DEVELOPMENT OF A PROTOTYPE OF FOURIER TRANSFORM
SPECTROGRAPH FOR THE THAI NATIONAL TELESCOPE

PORNAPA ARTSANG

A Thesis Submitted in Partial Fulfillment of the Requirements for the
Degree of Doctor of Philosophy in Applied Physics
Suranaree University of Technology
Academic Year 2021

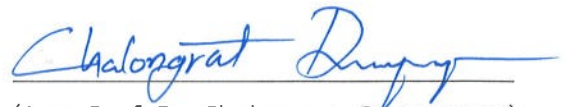# การพัฒนาระบบต้นแบบฟูเรียร์ทรานสฟอร์มสเปกโตรกราฟเพื่อประยุกต์ใช้กับกล้องโทรทรรศน์แห่งชาติ

นางสาวพรนภา อาจสังข์

วิทยานิพนธ์นี้เป็นส่วนหนึ่งของการศึกษาตามหลักสูตรปริญญาวิทยาศาสตรดุษฎีบัณฑิต
สาขาวิชาฟิสิกส์ประยุกต์
มหาวิทยาลัยเทคโนโลยีสุรนารี
ปีการศึกษา 2564

DEVELOPMENT OF A PROTOTYPE OF FOURIER TRANSFORM
SPECTROGRAPH FOR THE THAI NATIONAL TELESCOPE

Suranaree University of Technology has approved this thesis submitted in partial fulfillment of the requirements for a Degree of Doctor of Philosophy

Thesis Examining Committee

_____

(Asst. Prof. Dr. Chalongrat Daengngam)

Chairperson

_____

(Assoc. Prof. Dr. Panomsak Meemon)

Member (Thesis Advisor)

_____

(Prof. Dr. Joewono Widjaja)

Member

_____

(Assoc. Prof. Dr. Prayoon Songsiriritthigul)

Member

_____

(Dr. Athirot Mano)

Member

_____

(Assoc. Prof. Dr. Chatchai Jothityangkoon)

Vice Rector for Academic Affairs

and Quality Assurance

_____

(Prof. Dr. Santi Maensiri)

Dean of Institute of Science

พรนภา อาจสังข์ : การพัฒนาระบบต้นแบบฟูเรียร์ทรานสฟอร์มสเปกโตรกราฟ เพื่อ
ประยุกต์ใช้กับกล้องโทรทรรศน์แห่งชาติ (DEVELOPMENT OF A PROTOTYPE OF
FOURIER TRANSFORM SPECTROGRAPH FOR THE THAI NATIONAL TELESCOPE)
อาจารย์ที่ปรึกษา : รองศาสตราจารย์ ดร.พนมศักดิ์ มีมนต์, 118 หน้า.

คำสำคัญ: ฟูเรียร์ทรานสฟอร์มสเปกโตรกราฟ, เมโทรโลยี, คอนทราสต์, การแทรกสอด

ฟูเรียร์ทรานสฟอร์มสเปกโตรกราฟ เป็นหนึ่งในเครื่องมือที่มีความท้าทายหลายด้านในการ
พัฒนาทางด้านดาราศาสตร์ ความท้าทายประการหนึ่งคือการตรวจจับสัญญาณขนาดเล็กจากดาวฤกษ์
ที่อยู่ห่างไกล ซึ่งวิธีการแก้ปัญหาเพื่อให้ได้สัญญาณรบกวนต่ำในระบบนั้นมักจะมาพร้อมกับต้นทุนที่สูง
ดังนั้นในวิทยานิพนธ์นี้ จึงได้ทำการการออกแบบและพัฒนาต้นแบบระดับห้องปฏิบัติการของระบบฟู
เรียร์ทรานสฟอร์มสเปกโตรกราฟ ให้มีประสิทธิภาพสูง ในต้นทุนที่ต่ำ และมีขนาดกะทัดรัดสำหรับการ
ใช้งาน นอกจากนี้ ยังได้พัฒนาวิธีการแก้ไขปัญหาความผิดเพี้ยนของเฟสจากการเคลื่อนที่แบบไม่เชิง
เส้นของกระจกในระบบอีกด้วย

เพื่อให้ได้ผลลัพธ์ที่มีอัตราส่วนสัญญาณต่อสัญญาณรบกวนที่สูง ต้นแบบระบบที่พัฒนาขึ้นมี
การใช้เครื่องตรวจวัดแบบสมดุล ทำให้ได้อัตราส่วนของสัญญาณต่อสัญญาณรบกวนอยู่ที่ประมาณ 20
สำหรับความเข้มแสง 1.2 ไมโครวัตต์ นอกจากนี้ ยังได้ศึกษาผลกระทบของปัจจัยด้านขนาดของ
พื้นที่หน้าตัดของใยแก้วนำแสง และปัจจัยการเอียงของกระจกที่มีการเปลี่ยนแปลงตามการเคลื่อนที่
ซึ่งส่งผลต่อค่าคอนทราสต์ของสัญญาณการแทรกสอด ผลการวิจัยพบว่าการลดทอนค่าคอนทราสต์มี
ผลจากการเอียงของกระจกที่เกิดขึ้นระหว่างการเคลื่อนที่มากที่สุด โดยระยะการเคลื่อนที่สูงสุดของ
กระจกของระบบต้นแบบวัดได้เท่ากับ 15 มิลลิเมตร ซึ่งถูกกำหนดโดยค่าคอนทราสต์ของการแทรก
สอดที่สูงกว่า 0.5 ทั้งนี้ช่วงการสแกนส่งผลต่อความละเอียดในการวัดของระบบ เนื่องจากผลการแปลง
ฟูเรียร์ของสัญญาณที่มีขนาดจำกัด ส่งผลให้ได้ค่ากำลังการแยกสเปกตรัมของระบบที่พัฒนาขึ้น มีค่า
เป็น 19,609 ซึ่งสอดคล้องกับความละเอียดสเปกตรัมเท่ากับ 0.0323 นาโนเมตร ที่ความยาวคลื่น
633.178 นาโนเมตร

นอกจากนี้ ระบบที่พัฒนาขึ้นยังได้รับการตรวจสอบโดยการวิเคราะห์การดูดกลืนแสงบน
สเปกตรัมของดวงอาทิตย์ โดยวิเคราะห์เปรียบเทียบเส้นที่วัดได้ กับแบบจำลองทางคณิตศาสตร์ อีกทั้ง
ยังสามารถใช้เส้นดูดกลืนแสงที่วัดได้เพื่อวิเคราะห์ความแม่นยำและความเสถียรของระบบที่พัฒนาขึ้น
ผลการทดลองพบว่าระบบที่พัฒนาขึ้นนั้นสามารถตรวจจับเส้นดูดกลืนแสงแบบละเอียดของ เส้น
สเปกตรัมของ Fe-I ที่ความยาวคลื่น 846.8 นาโนเมตร โดยมีความกว้างเท่ากับ 0.0562 นาโนเมตร
และมีอัตราส่วนสัญญาณต่อสัญญาณรบกวนสูงกว่า 15

สาขาวิชาฟิสิกส์	ลายมือชื่อนักศึกษา_____
ปีการศึกษา 2564	ลายมือชื่ออาจารย์ที่ปรึกษา_____

PORNAPA ARTSANG : DEVELOPMENT OF A PROTOTYPE OF FOURIER TRANSFORM SPECTROGRAPH FOR THE THAI NATIONAL TELESCOPE THESIS ADVISOR : ASSOC. PROF. PANOMSAK MEEMON, Ph.D. 118 PP.

Keyword: Fourier transform spectrograph, Metrology, Contrast, Interference

The Fourier Transform Spectrograph (FTS) is one of the most challenging instruments that has been applied in astronomy. One of the challenges is to detect the small signal from a distant star. However, most of the solution to achieve high signal-to-noise ratio (SNR) in FTS comes with a high cost. In this thesis, the design and implementation of the laboratory prototype of a high performance, cost-effective, and compact fiber-fed FTS system for astronomical applications has been investigated. Moreover, a method for correction of the non-uniform data sampling due to a non-linear movement of the scanning mirror using a metrology interferogram and a cubic spline interpolation has been designed and implemented.

To achieve high SNR for the developed FTS prototype, a balance detection scheme was designed and implemented. The achieved SNR approximately was 20 for an input flux of 1.2 μW. Furthermore, the effects of the source's spatial extension and the mirror tilt along the translation direction to the loss in fringe contrast were studied. The results show that the loss in contrast is mainly governed by the tip-tilt of the dynamic mirror. The achieved maximum scanning distance of the developed system, as determined by the interference contrast drops of higher than 0.5, was measured to be 15 mm. The scanning range affect the achievable resolution of the system because of the truncate property of the Fourier transformation. The spectral resolving power of the developed system as defined by the full width at half maximum that was retrieved from the instrument line shape of metrology source was measured to be 19,609. This corresponds with a spectral resolution of 0.0323 nm at 633.178 nm wavelength.

Furthermore, the instrument line shape of the developed system was verified by analyzing absorption peaks on the spectrum of the Sun. The analysis of the telluric and Sun absorption lines obtained from the measurement was compared with that of the absorption spectrum obtained from a synthetic model. Moreover, the measured telluric absorption lines were used to determine the precision and stability of the developed system.

The result shows that the developed FTS system was able to detect a fine absorption line of Fe-I at wavelength 846.8 nm with a width equal to 0.0562 nm and with a signal-to-noise ratio higher than 15.

School of Physics

Academic Year 2021

Student's Signature _____

Advisor's Signature _____

ACKNOWLEDGEMENTS

I would like to express my sincere gratitude to my advisor, Assoc. Prof. Dr. Panomsak Meemon, for his patience, advice, and many helpful suggestions, and to Dr. Christophe Buisset who had the vision to develop the instrument. The success of the development was greatly support by them.

Special thanks to Dr. Sorawis Sangtawesin from SUT, Dr. Pakakaew Rittipruk, Dr. Sirinrat Sithajan, Dr. Anthony Berdeu, and Dr. Supachai Awiphan from NARIT for the constructive discussions.

I warmly thank to my colleagues of the Center for Optics and Photonics, NARIT and SUT friends for all supporting.

Last but not least, I wish to thanks my family for supporting me throughout the years, financially, practically and with moral support.

Pornapa Artsang

CONTENTS

CONTENTS (Continued)

CONTENTS (Continued)

LIST OF TABLES

LIST OF FIGURES

LIST OF FIGURES (Continued)

LIST OF FIGURES (Continued)

LIST OF FIGURES (Continued)

LIST OF FIGURES (Continued)

LIST OF FIGURES (Continued)

LIST OF FIGURES (Continued)

LIST OF ABBREVIATIONS

AC   Alternating Current
BS   Beam Splitter
DC   Direct Current
EM   Electromagnetic
FFT   Fast Fourier Transform
FTS   Fourier Transform Spectrograph
FWHM   Full Width at Half Maximum
HiRes   High Resolution
ILS   Instrument Line Shape
LowRes   Low Resolution
MedRes   Medium Resolution
OPD   Optical Path Difference
R   Spectral resolution
SNR   Signal to Noise Ratio
TAPAS   Transmissions of the AtmosPhere for AStronomical data
ZPD   Zero optical Path Difference

CHAPTER I

INTRODUCTION

1.1 Background of Fourier Transform Spectrograph

1.1.1 Basic of spectroscopy

The spectroscopy technique is commonly used to analyze an interaction between the electromagnetic (EM) wave of the source and the sample. EM radiation is composed of an electric field and a magnetic field that are perpendicular propagated. These two vectors oscillate at right angles to each other in planes perpendicular to the direction of propagation, as illustrated in Figure 1.1. In general, the vibrational modes of atom inside the molecule of a sample are introduced by the nature of each atom known as its "finger print" , which is unique and relates to the their physical properties inside molecular structure (Hu et al., 2016). These vibrational modes of an atom cause absorption in the source spectrum at specific frequencies and energies. Therefore, the spectral features of each sample can be distinguished.

The photon is an elementary particle used to explain EM phenomena in the term of quantum mechanics (Hofmann, 2010). When light interacts with a sample, it will transfer its energy interpreted as

$$E = \frac{hc}{\lambda} \; , \tag{1.1}$$

where h is the Planck constant ($h = 6.63 \times 10^{-34}$ Js), c is the speed of light ($c = 2.998 \times 10^{-8}$ m/s in vacuum) and λ is the wavelength which is defined as one cycle in the sinusoidal waveform or the spatial distance between the two consecutive peaks. This is illustrated in Figure 1.1. The vibrations of an atom inside the molecule provide the change of energy (ΔE) between the starting and the final states.

The spectrograph is an instrument that has been designed as a tool to detect the relative amount of energy from the radiation at each wavelength or frequency and thus provide results in the form of spectrum. The types of spectrograph can be classified into two categories, dispersive and non-dispersive spectrographs. The dispersive spectrograph generates the spectrum result by using dispersing elements, such as prisms and gratings, to split the light into the different wavelength. The non-

dispersive spectrograph operates without those restriction parts and thus provides the higher throughput than in the dispersive technique.
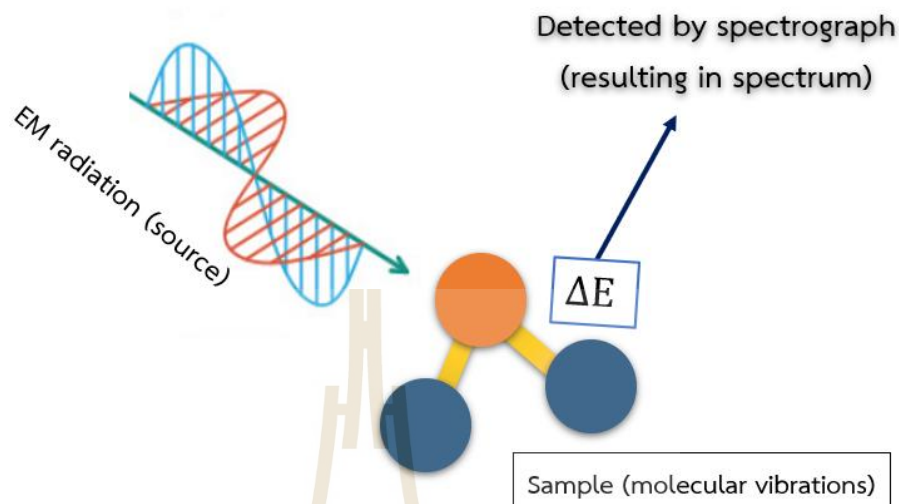
Figure 1.1   Schematic of the light radiation in the form electromagnetic wave that interacts with the sample and causes the vibrations inside the molecule.

The spectrograph is an instrument that has been designed as a tool to detect the relative amount of energy from the radiation at each wavelength or frequency and thus provide results in the form of spectrum. The types of spectrograph can be classified into two categories, dispersive and non-dispersive spectrographs. The dispersive spectrograph generates the spectrum result by using dispersing elements, such as prisms and gratings, to split the light into the different wavelength. The non-dispersive spectrograph operates without those restriction parts and thus provides the higher throughput than in the dispersive technique.

The optical resolving power is the key to evaluate the spectrograph, this is also known as "spectral resolution", which is determined by the minimum resolved wavelength ($\Delta\lambda$) between two spectral lines of the instrument. The resolution of spectrograph is defined as $R = \lambda/\Delta\lambda$ (Massey and Hanson, 2013). When $R < 3000$, the spectrograph is considered a "Low resolution (LowRES) spectrograph", while the situations of $3000 < R < 10,000$ and $R > 10,000$ are defined as "Medium resolution (MRES) spectrographs" and "High resolution (HiRES) spectrographs", respectively. The applications of spectrographs depend on their used. For example in astronomical application, the LowRES is commonly used to investigate the faint sources while the

MRES and HiRES, with higher resolutions, act as tools for observation bright source (Simcoe et al., 2013).

1.1.2 Fourier Transform Spectrograph

The Fourier Transform Spectrograph (FTS) is a non-dispersive spectrograph. It has been applied to the study of the vibrational responses that are caused by light interactions (Griffiths et al., 2007) in the form of absorption lines along the spectrum result. Figure 1.2 illustrates the block diagram of the FTS working process. The FTS necessarily uses the interferometer as a tool to receive the spectrum. The light source is passed through the sample and then reaches the interferometer. The output of the interferometer is called an "interferogram", which is detected by a detector. The spectrum result is thus determined from the implementation of a Fourier transform to the interferogram as a post-signal processing. The strengths of a FTS are declared as high accuracy and precision, speed, increasing of sensitivity, ease of operation, and non-destructive testing of the sample (Undavalli et al., 2021).
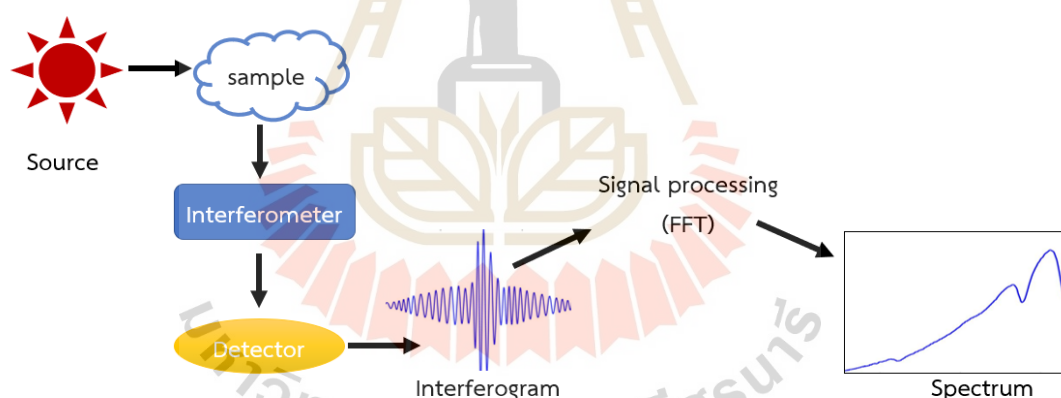
Figure 1.2   Schematic concept of the FTS technique.

Furthermore, the FTS includes two major advantages over the dispersive spectrometers especially in the infrared region (Thorne et al., 1999), including the "multiplex or Fellgett advantage" and the "throughput or Jacquinot advantage".

The Fellgett advantage (Fellgett, 1949) describes the capability of FTS technique to measure spectral information from all wavelengths simultaneously, while in a dispersive spectrograph each spectrum element is consecutively measured. It can be inferred that in order to obtain spectra with the same signal-to-noise ratio, the dispersive spectrum requires a longer time of measurement than the FTS. Meanwhile,

for the spectra that were measured at the same time and the same resolution, the FTS gains a higher signal-to-noise-ratio than the dispersive spectrograph (Griffiths et al., 2007).

The Jacquinot advantage (Jacquinot, 1960) states that the FTS measurements provide a very high throughput compared to dispersive spectrographs. In addition, the capability to easily adjust the resolution by varying the scan range of the interferometer (Réhault et al., 2017) is included as the benefit of the FTS technique. For these reasons, the FTS has been implemented in various applications.

1.2 FTS in astronomy

Spectroscopy is a famous technique that has been applied to studying the universe (Massey and Hanson, 2013) based on the concept that all the information of planets are affected by their environment, which is composed of standard elements such as hydrogen, carbon, etc. that can be characterized by the principle of the spectroscopy.

The FTS technique has been successfully used in planetary investigation and in the analysis of the Earth's atmosphere (Drissen et al., 2011) and also applied in astronomical observations in order to analyze the properties, compositions, and radial velocities of stellar sources. The first investigation of the earth's atmosphere was done during 1940's with the grating spectrograph. The absorption features of methane (Migeotte, 1948) and carbon monoxide (Migeotte, 1949), were detected in the spectrum of the solar observations.

During the late 1970s and early 1980s, the ground-based FTS has started in the applications of astronomical observation (Paton-Walsh, 2011) with the first prototype systems for solar-tracking at Kitt Peak National observatory on 4-m telescope, as illustrated in the left panel of Figure 1.3 with Initial interest in the detection of stratospheric trace gasses (Rinsland et al., 1986). Through the mid-1980s, Kitt Peak National observatory provided spectra in the spectral range 1 μm to 5 μm at a spectral resolution close to 20,000 in the K band.

The Canada-France-Hawaii Telescope (CFHT), as illustrated in the right panel of Figure 1.3, is famous for high-resolution FTS which started operating in the 80's in a large variety of planetary and stellar applications (Chalabaev and Maillard, 1985). It was widely used to provide spectrum in the near-infrared of both single-point and extended objects (L. Drissen et al., 2016).
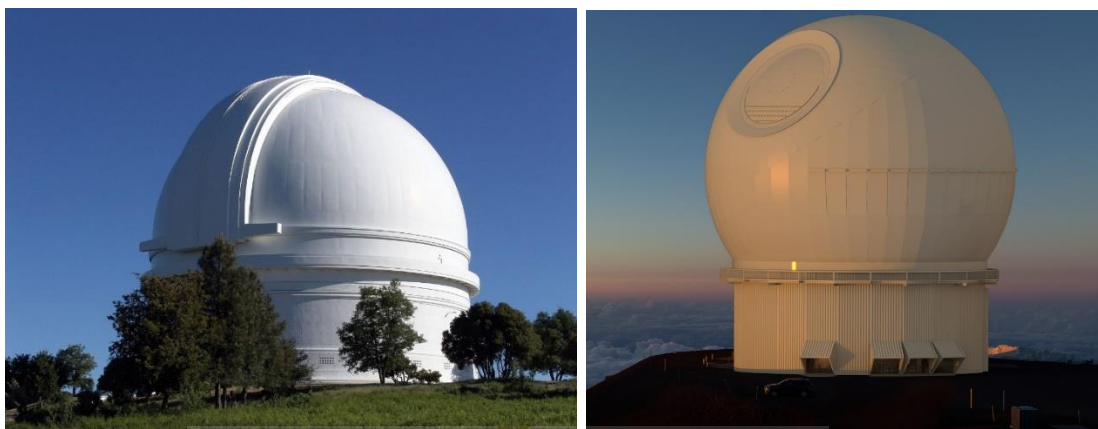
Figure 1.3   (Left) The Kitt Peak National observatory or Mayall 4-m telescope installed at Kitt Peak in Southern Arizona, USA (Britannica, 2020). (Right) The CFHT that committed to the Maunakea Spectroscopic Explorer as the future of the facility in Hawaii, USA (Laychak, 2020).

More recently, some very nice imaging FTS operating in the optical domain were developed and installed on large telescopes. The Spectromètre Imageur de l'Observatoire du Mont-Mégantic (SpIOMM) installed on the focal plane of the 1.6-m telescope of the Mont Mégantic Observatory in Québec, Canada. This instrument has been able to provide hyperspectral images over the full visible spectral domain and spectral resolution between 1,000 and 2,000 (Drissen et al., 2012). The most advanced version of the FTS hyperspectral imagers operating in the optical domain is certainly the instrument Spectromètre Imageur à Transformée de Fourier pour l'Etude en Long et en Large de raies d'Emission (SITELLE) that was installed on the 3.6-meter CFHT and started to provide spectrum of stellar sources in 2015 (Grandmont et al., 2016). This instrument provides hyperspectral images over the spectral domain 350 nm to 900 nm with a spectral resolution adjustable between 1 and 10,000.

Those FTS systems were designed to receive an incoming flux direct from the telescope. It is important to mention that all these systems are massive and complex instruments installed directly at the focal plane of the telescopes. The design thus involves only large and custom-made optics together with complex mechanical structures and active mechanisms. In order to guaranty the performance, the instrument is operated under the controlled conditions, including the telescope vibrations, the influence of the gravity and the thermoelastic effects on the optical surface's positions and orientations. These design constraints generally lead to massive instruments, difficult to manufacture and very expensive.

To overcome this limitation, the implementation of a fiber to feed the incoming light from the telescope to the spectrograph has been investigated. This efficient method is simple and can improve the performance of the system, such as the high accuracy of radial velocity measurements(Queloz et al., 1999). Most of the current fiber-fed high resolution spectrographs mounted on large telescopes are Echelle Spectrographs (Chakraborty et al., 2014; Pilachowski et al., 1995). One of the most famous examples is the High Accuracy Radial velocity Planet Searcher (HARPS) spectrograph mounted on the 3.6-m telescope at the European Southern Observatory (ESO) La Silla observatory that has provided high quality spectrum and makes the discovery of several new exoplanets and other astronomical phenomena possible (Pepe et al., 2000; Rodler and Curto, 2019).

The diameter of the fiber of an Echelle spectrograph is adjusted to match the size of the star image provided by the telescope and defined by the seeing conditions. The collimator focal length is then adjusted to reach specified spectral resolution and the fiber core diameter. This focal length defines the grating size and thus the instrument volume. For example, in HARPS, the fiber core diameter is equal to 70 microns, that corresponds to an on-sky size of 1 arcsecond. The collimator focal length is equal to 1.6 m and the grating dimensions are equal to 840 × 214 × 125 mm to reach a specified spectral resolution equal to 115,000. That yields a very large instrument volume that requires a Vacuum vessel of volume close to 2 m^3 to stabilize the instrument environment. These instruments require high precision and large optical surfaces, a fully controlled environment to reach the specified performance. The cost is thus usually very high and only large observatories with massive facilities and large budget resources can afford the development of such instruments.

In addition, there is a trade-off between fiber core diameter and system efficiency. The large fiber core can cover a broader sky aperture, but with less system efficiency. In contradiction, the small size of fiber core provides high system efficiency, but a limited sky coverage area. For example, the HARPS spectrograph has two operating modes. The first mode, called as HAM mode, is operated with the fiber core diameter equal to 70 microns with a covered sky aperture of 1 arcsecond, which provides the accuracy of radial velocity at 1 m/s. The second mode is operated with the fiber core diameter 100 microns, known as the high efficiency (EGGs) mode. It gains throughput a factor of 1.75 as compared to the HAM mode with the covered sky aperture of 1.4 arcseconds but the accuracy of radial velocity is reduced to 3 m/s.

The instrument transmission is mostly limited by the limited size of the input fiber core diameter that is designed to be matched and fit to the seeing conditions,

the optics transmission, and the and the grating efficiency (Lhospice et al., 2019). Therefore, the dispersive elements limit its throughput. For example, the maximum transmission of HARPS including the limited core diameter and the spectrometer transmission is close to 6% at the wavelength equal to 550 nm, as illustrated in Figure 1.4 (Rodler and Curto, 2019).
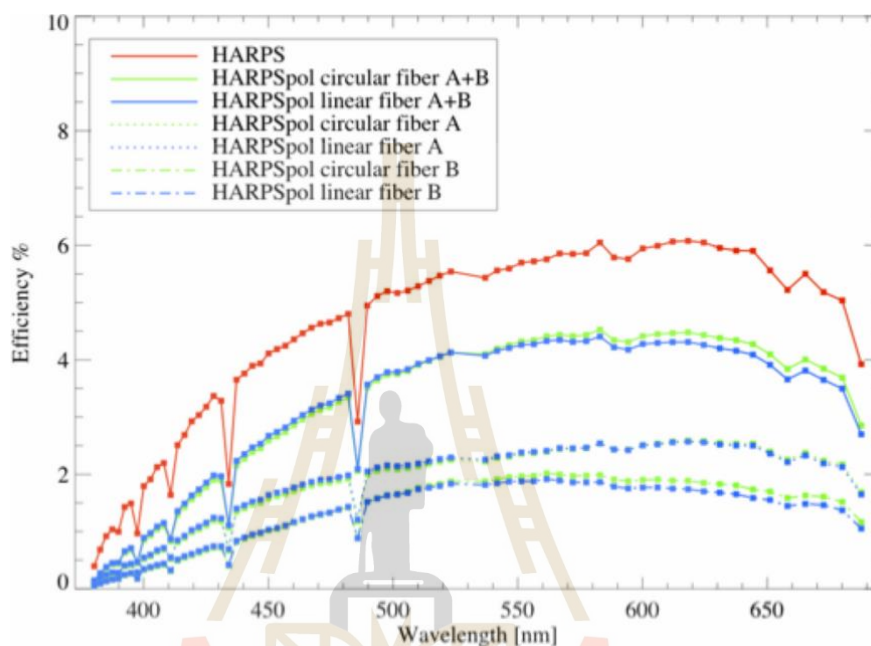
Figure 1.4   The throughput transmission of HARPS spectrograph (Rodler and Curto, 2019).

1.3 Significance of study

Many FTS instruments have been applied in astronomical observation. Most of them were installed at the telescope focal plane and directly obtained star flux from the telescope (Drissen et al., 2011). This installation required to be placed in a vacuum for the telescope body. Furthermore, it can be induced the guiding error due to the velocity shift of the star objects (Bernier et al., 2006).

At the Thai National Telescope (TNT), another spectrograph already existed at its focal. In order to connect the developed FTS to the TNT, one solution is to connect by using an optical fiber to receive the incoming flux and direct to the FTS system. Through that, the FTS system can be installed inside the controlled room with stable environment. The proposed individual system provides more convenience in order to align the setup without any interruption.

The developed FTS system can resolve the low throughput that has occurred in the fiber-fed HARPS spectrograph. However, the FTS includes more challenges in the interferometer optical alignment and requires a high precision of mirror scan.

There is one consideration that the flux will be lost due to the fiber transmission. The capability of low flux intensity detection is one challenge of the developed fiber-fed FTS system.

In this thesis, the balanced detection of instrument design is one solution for this problem. It can remove the offset of the interferometer output (Soldevila et al., 2016) and thus increase the signal to noise ratio (P. Zhang et al., 2021).

Furthermore, the spectral resolution of the FTS is governed by the range of the mirror scan inside the interferometer. To reach a system of high-resolution, a large scan range is required. However, the scan range is limited by the contrast loss of the recorded interferogram, which can be affected by the optical alignment of the interferometer such as the scanning mirror misalignment or an off-axis source. In this thesis, these two possible effects of the contrast loss have investigated. The sources spatial extension due to the use of large fiber cores and the tilt of the mirror along the scan have been studied.

Moreover, the implementation of Fourier transform to obtain the spectrum result requires the accurate phase information of the interferogram. In practical, the translation of the dynamic mirror is normally subjected to non-linear movement and thus induces the phase distortion in the interferogram. Therefore, the developed FTS system has been designed to include a metrology interferometer in common path in order to calibrate the non-linear scan of the dynamic mirror. The signal processing for these phase corrections by using the metrology interferogram to resampling the scientific interferogram was developed. The cubic spline interpolation has been investigated for the spectrum aliasing correction.

1.4 Research objectives

1.4.1   To design and develop a fiber fed FTS system in laboratory conditions using balanced detection +scheme in order to increase the signal-to-noise-ratio from the low flux intensity detection.

1.4.2   To verify the limited scan range by the contrast variation and investigate the sources of contrast loss in the developed FTS system.

1.4.3   To develop the signal processing for the implemented FTS system for the phase correction of scientific signal using metrology interferogram and cubic spline interpolation.

1.5 Scope

       1.5.1   Design and develop the compact FTS instrument setup that was made of only off-the-shelf components, which is operated following the specifications in the Table 1.

       1.5.2   Develop the signal processing by using MATLAB2021a program to transform the interferogram signal that was obtained from interferometer to receive the spectrum result.

       1.5.3   Verify the performance of the FTS by investigation of fringe contrast varying and the instrument line shape of the system.

       1.5.4   Use halogen-tungsten source and two spectral bandpass filters to evaluate spectrum results obtained from the fiber and the bandpass filter transmissions.

       1.5.5   Test the implemented FTS system by measuring spectrum of the Sun light through the multi-mode fiber, in order to investigate the atmospheric and Sun absorption lines.

       1.5.6   Analyze the spectral qualities of the Sun spectrum by measuring the signal-to-noise-ratio and the spectral resolving power of the interested absorption lines.

Table 1.1   The target specifications of FTS instrument.

Parameter	Specification
Science spectral band	[400 nm, 1000 nm]
Setup Architecture	1 scientific channel + 1 metrology channel
Metrology source	He-Ne Laser source
Maximum Optical Path Difference	> 1 cm

CHAPTER II

THEORETICAL BACKGROUND

2.1 Concept of Fourier Transform Spectrograph

A classical configuration for FTS uses the Michelson interferometer as the heart of the system (Lacan et al., 2010) (Heverly et al., 2004). The schematic of classical Michelson interferometer is illustrated in Figure 2.1.
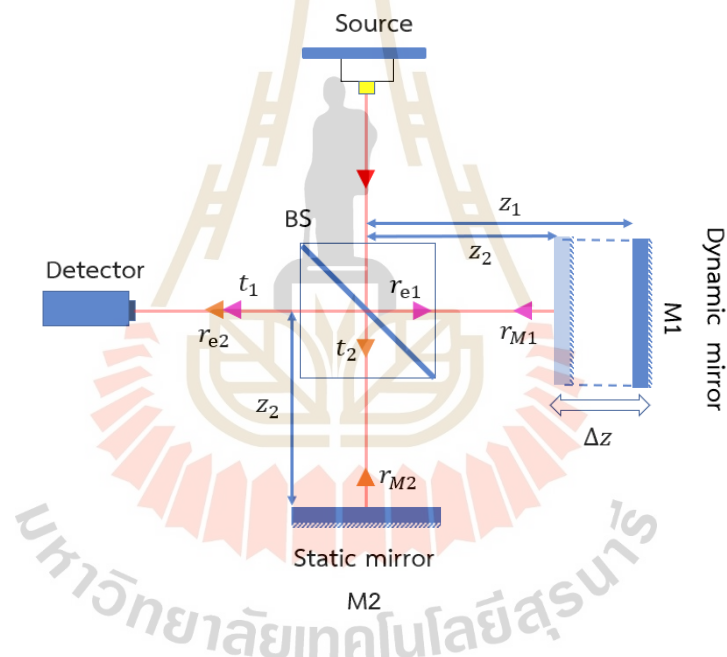
Figure 2.1   A schematic diagram of classical Michelson interferometer.

The light source injects the beam to the beam splitter (BS). The BS splits the beam into two channels. The light beam in the first channel travels to the dynamic mirror (M1) while the second channel is directed to the static mirror (M2). Then, the two beams are reflected by each mirror back to the BS. Finally, the BS recombines the two beams and directs it toward the detector.

The output of interferometer consists of the direct current (DC) part and the alternating current (AC) part. The modulated signal are all included in the AC part, which is determined by the autocorrelation function (Toenger et al., 2019).

The DC part can be eliminated by balanced detection (Soldevila et al., 2016). Therefore, the signal to noise ratio in balanced detection is improved compared that of a classical interferometer with single output (P. Zhang et al., 2021). This chapter will be focused on the Michelson interferometer with balanced detection of two outputs in order to improve on the small oscillated signals for Astronomical observations.

The mathematical expression of this phenomena will be described hereafter.

2.2 Mathematical description

The electromagnetic radiation of the light source is a traveling wave that includes the orthogonal electric and magnetic field varying amplitude with respect to time. Since the amplitude and phase of the magnetic field are related linearly to the electric field, the expression of the light wave that travel through the interferometer as only the electric field of electromagnetic wave will be considered.

2.2.1 Michelson interferometer

The wave equation form for a light emitted from a monochromatic source at wavelength λ_0 and travelling in a distance z can be expressed in an exponential form of electric field (E) as (Born and Wolf, 1999)

$$E(\sigma_0, t, z) = E_0 e^{i(\omega_0 t \pm k_0 z)} = E_0 e^{i(\omega_0 t \pm 2\pi\sigma_0 z)} , \tag{2.1}$$

where E_0 is a scalar amplitude of electric field. k_0 is the wave number defined as $k_0 = \frac{2\pi}{\lambda_0}$. ω_0 is the angular frequency, which can be expressed in a function of frequency as $\omega_0 = 2\pi c\sigma_0$, where c is the speed of light. σ_0 is the spatial frequency, which is defined as the inverse of wavelength $\sigma_0 = \frac{1}{\lambda_0}$ that will be called as frequency along this thesis report. The plus ($+$) and minus ($-$) signs respectively represent the in the negative and positive direction of wave propagations.

As illustrated in Figure 2.1, the detector detects the signal that is formed from the two waves that were reflected from the mirror M1 and M2, as shown in the pink and orange arrow lines, respectively. The detected intensity can be written as

$$I_D(\sigma_0) = |E_1(\sigma_0, t, z_1) + E_2(\sigma_0, t, z_2)|^2 , \tag{2.2}$$

where $E_1(\sigma_0, t, z_1)$ and $E_2(\sigma_0, t, z_2)$ are electric fields of the beams in channel 1 and 2 that represent the propagated waves reflected from the dynamic mirror M1 and the static mirror M2, respectively.

Following the beam path of channel 1 as illustrated in the pink line of Figure 2.1, the beam is first reflected by the BS, which includes the external reflection coefficients defined as r_{e1}. Then, the beam is reflected by mirror M1 back to the BS corresponding to the amplitude reflection coefficients of the mirror defined as r_{M1}. Finally, the beam is thus transmitted through the BS to reach the detector with the amplitude transmission coefficients defined as t_1. The expression of detected electric field of the beam in channel 1 at the detector can be simplified and written as

$$E_1(\sigma_0, t, z_1) = r_{e1} r_{M1} t_1 E_{10} e^{i\omega_0 t} e^{i2\pi\sigma_0 \cdot 2z_1}, \tag{2.3}$$

where E_{10} is the scalar amplitude of electric field of the beam in channel 1, and z_1 is the propagation distance of light in the channel 1. Notice that which is equal to twice of the mirror distance due to the travel back and forth of the beam path.

On the other hand, the beam path of channel 2 is first transmitted through the BS to reach mirror M2, as illustrated in the orange line of Figure 2.1, which contains the transmission coefficients t_2. Then, the mirror M2 reflects the beam back to the BS with reflection coefficients of mirror M2 defined as r_{M2}. Finally, the beam is thus reflected by the BS to the detector with the external reflection coefficients at the BS defined as r_{e2}. The electric field of the beam in channel 2 is expressed as

$$E_2(\sigma_0, t, z_2) = t_2 r_{M2} r_{e2} E_{20} e^{i\omega_0 t} e^{i2\pi\sigma_0 \cdot 2z_2}, \tag{2.4}$$

where E_{20} is the scalar amplitude of electric field of the channel 2, and z_2 is the propagation distance of light in the channel 2.

Following Equation (2.2), the intensity detected at the detector can be written as

$$I_D(\sigma_0) = \big(E_1(\sigma_0, t, z_1) + E_2(\sigma_0, t, z_2)\big)\big(E_1(\sigma_0, t, z_1) + E_2(\sigma_0, t, z_2)\big)^*. \tag{2.5}$$

This expression can be written in the complex conjugate form as

$$\begin{aligned} I_D(\sigma_0) = E_1(\sigma_0, t, z_1)E_1^*(\sigma_0, t, z_1) &+ E_2(\sigma_0, t, z_2)E_2^*(\sigma_0, t, z_2) \\ &+ E_1(\sigma_0, t, z_1)E_2^*(\sigma_0, t, z_2) \\ &+ E_2(\sigma_0, t, z_2)E_1^*(\sigma_0, t, z_1). \end{aligned} \tag{2.6}$$

Then, let substitute Equation (2.3) and Equation (2.4) into Equation (2.6) and express each term as follow. The first term is expressed as

$$
E_1(\sigma_0, t, z_1)E_1^*(\sigma_0, t, z_1)
$$
$$
= \left[r_{e1}r_{M1}t_1E_{10}e^{i\omega_0 t}e^{i2\pi\sigma_0\cdot 2z_1}\right]\left[r_{e1}r_{M1}t_1E_{10}e^{-i\omega_0 t}e^{-i2\pi\sigma_0\cdot 2z_1}\right]
$$
$$
= |r_{e1}r_{M1}t_1E_{10}|^2. \qquad (2.7)
$$

The expression of the second term is

$$
E_2(\sigma_0, t, z_2)E_2^*(\sigma_0, t, z_2)
$$
$$
= \left[t_2r_{M2}r_{e2}E_{20}e^{i\omega_0 t}e^{i2\pi\sigma_0\cdot 2z_2}\right]\left[t_2r_{M2}r_{e2}E_{20}e^{-i\omega_0 t}e^{-i2\pi\sigma_0\cdot 2z_2}\right]
$$
$$
= |t_2r_{M2}r_{e2}E_{20}|^2. \qquad (2.8)
$$

The expression of the third term is

$$
E_1(\sigma_0, t, z_1)E_2^*(\sigma_0, t, z_2)
$$
$$
= \left[r_{e1}r_{M1}t_1E_{10}e^{i\omega_0 t}e^{i2\pi\sigma_0\cdot 2z_1}\right]\left[t_2r_{M2}r_{e2}E_{20}e^{-i\omega_0 t}e^{-i2\pi\sigma_0\cdot 2z_2}\right]
$$
$$
= r_{e1}r_{M1}t_1t_2r_{M2}r_{e2}E_{10}E_{20}e^{i2\pi\sigma_0\cdot 2(z_1-z_2)}. \qquad (2.9)
$$

And the fourth term is thus expressed as

$$
E_2(\sigma_0, t, z_2)E_1^*(\sigma_0, t, z_1)
$$
$$
= \left[t_2r_{M2}r_{e2}E_{20}e^{i\omega_0 t}e^{i2\pi\sigma_0\cdot 2z_2}\right]\left[r_{e1}r_{M1}t_1E_{10}e^{-i\omega_0 t}e^{-i2\pi\sigma_0\cdot 2z_1}\right]
$$
$$
= t_2r_{M2}r_{e2}r_{e1}r_{M1}t_1E_{20}E_{10}e^{-i2\pi\sigma_0\cdot 2(z_1-z_2)}. \qquad (2.10)
$$

Therefore, the detected intensity is obtained by substituting Eq. (2.7), (2.8), (2.9), and (2.10) into Equation (2.6) as

$$
I_D(\sigma_0, z) = |r_{e1}r_{M1}t_1E_{10}|^2 + |t_2r_{M2}r_{e2}E_{20}|^2
$$

$$
+r_{e1}r_{M1}t_1t_2r_{M2}r_{e2}E_{10}E_{20}e^{i2\pi\sigma_0\cdot 2|z_2-z_1|} + t_2r_{M2}r_{e2}r_{e1}r_{M1}t_1E_{20}E_{10}e^{-i2\pi\sigma_0\cdot 2|z_2-z_1|}.
$$
$$
(2.11)
$$

The system can be considered with the following assumptions:

1) The BS is ideally 50:50 transmission and reflection. Following the separation on the beam splitter (Hughes et al., 2021), the relation is thus obtain as $E_{10} = E_{20} = \frac{E_0}{\sqrt{2}}$.

2) The external reflection coefficients of splitter beam and the recombiner beam are identical ($r_{e1} = r_{e2}$), which is defined as r_{bs}.

3) The transmission coefficient of splitter beam and the recombiner beam are identical ($t_1 = t_2$), which is defined as t_{bs}.

4) The amplitude reflection coefficients of the two mirrors M1 and M2 are identical ($r_{M1} = r_{M2}$), which is defined as r_M.

The mirror moves in a displacement defined as $\Delta z = |z_2 - z_1|$, while the Optical Path Difference (OPD) is twice the displacement as $OPD = 2\Delta z$. When two mirrors are positioned at the same distance from BS, there are no time delay between two propagated wave fields in both channels ($OPD = 0$) which is called as "Zero optical Path Difference (ZPD)".

Therefore, the intensity form in Equation (2.11) can be expressed as

$$I_D(\sigma_0, OPD) = |r_{bs} r_M t_{bs} E_0|^2 + r_{bs}^2 r_M^2 t_{bs}^2 \frac{E_0^2}{2} e^{i2\pi\sigma_0 \cdot OPD} + r_{bs}^2 r_M^2 t_{bs}^2 \frac{E_0^2}{2} e^{-i2\pi\sigma_0 \cdot OPD}.$$

(2.12)

By applying the Euler's formula, the intensity result can be written in the simplified form as,

$$I_D(\sigma_0, OPD) = 2R_{bs} R_M T_{bs} \cdot E_0^2 (1 + cos(2\pi\sigma_0 OPD)),$$ (2.13)

where $R_{bs} = r_{bs}^2$ and $R_M = r_M^2$ define the intensity reflection coefficients of the BS and the mirrors, respectively. $T_{bs} = t_{bs}^2$ defines the intensity transmission coefficients of the BS.

Figure 2.2 is visually present showing the plot with labels:
- Constructive interference (top dashed line at 2)
- $DC = 2R_{bs}R_M T_{bs} \cdot E_0^2$ (middle dashed line at 1)
- Destructive interference (bottom dashed line at 0)
- Y-axis: Intensity (A.U.)
- X-axis: Data points (100 to 600)
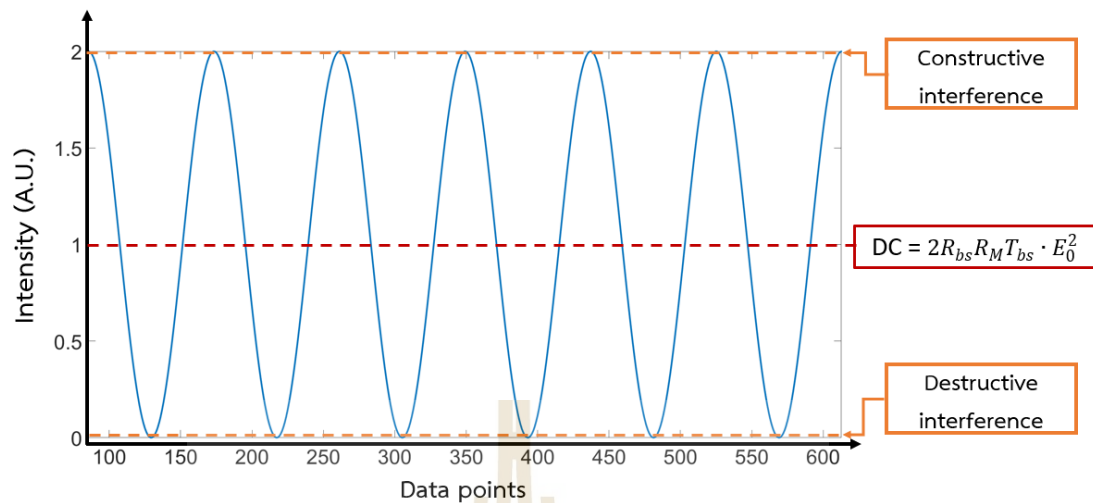
Figure 2.2   A simulation of interferogram of a monochromatic source in a cosine waveform.

The expression of intensity result in Equation (2.13) is called as "interferogram", as illustrated in Figure 2.2. The first term is a DC part which is a constant term. The second term, containing of the modulation of cosine signal, is an AC part. The maximum amplitudes, called constructive interference, appear when the two waves are in phase. The minimum amplitudes, called destructive interference, appear when the two waves are out of phase. The DC part can be removed by the balanced detection that will be described hereafter.

2.2.2 Balanced and unbalanced outputs in Michelson interferometer

In this sub-Section, the Michelson interferometer will be described as the two outputs including of balanced and unbalanced outputs through the design of two retro-reflectors, as illustrated in Figure 2.3. In situation, the BS simultaneously acts as the beam splitter and beam compensator, while the retro-reflector acts as the mirror.
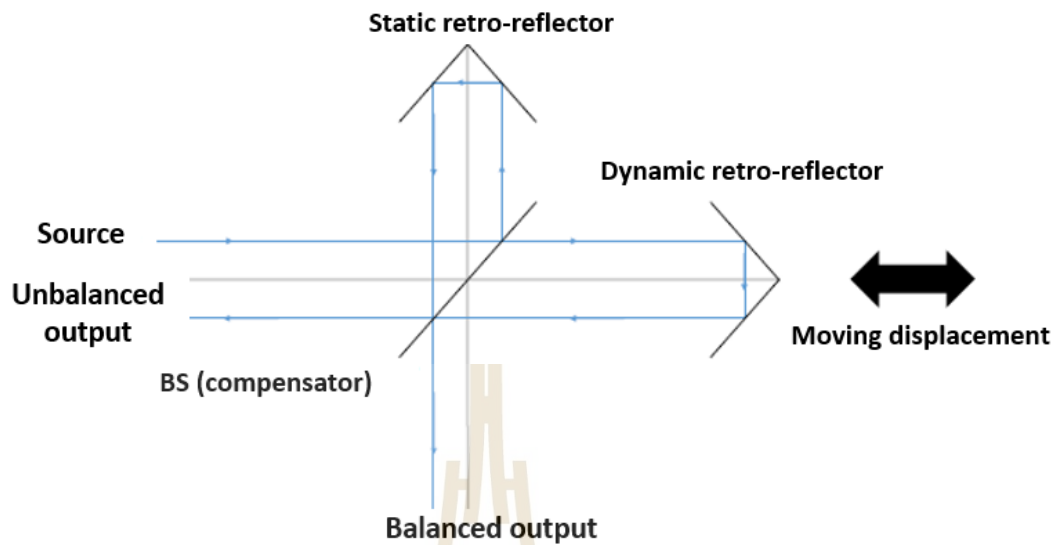
Figure 2.3 The expression of two outputs interferometer from the two retro-reflectors (Libert, 2016).

The beam that is reflected by the BS provides the reflection coefficient (R_{bs}) while the beam that is transmitted through it has related to the transmission coefficient (T_{bs}). The balanced output is directly obtained as the ordinary paths from the interferometer, while the unbalanced output is taken the different paths. The unbalanced output in channel 1 contains twice transmissions while it includes twice reflections in channel 2, as illustrated in Figure 2.4(a) and (b), respectively.
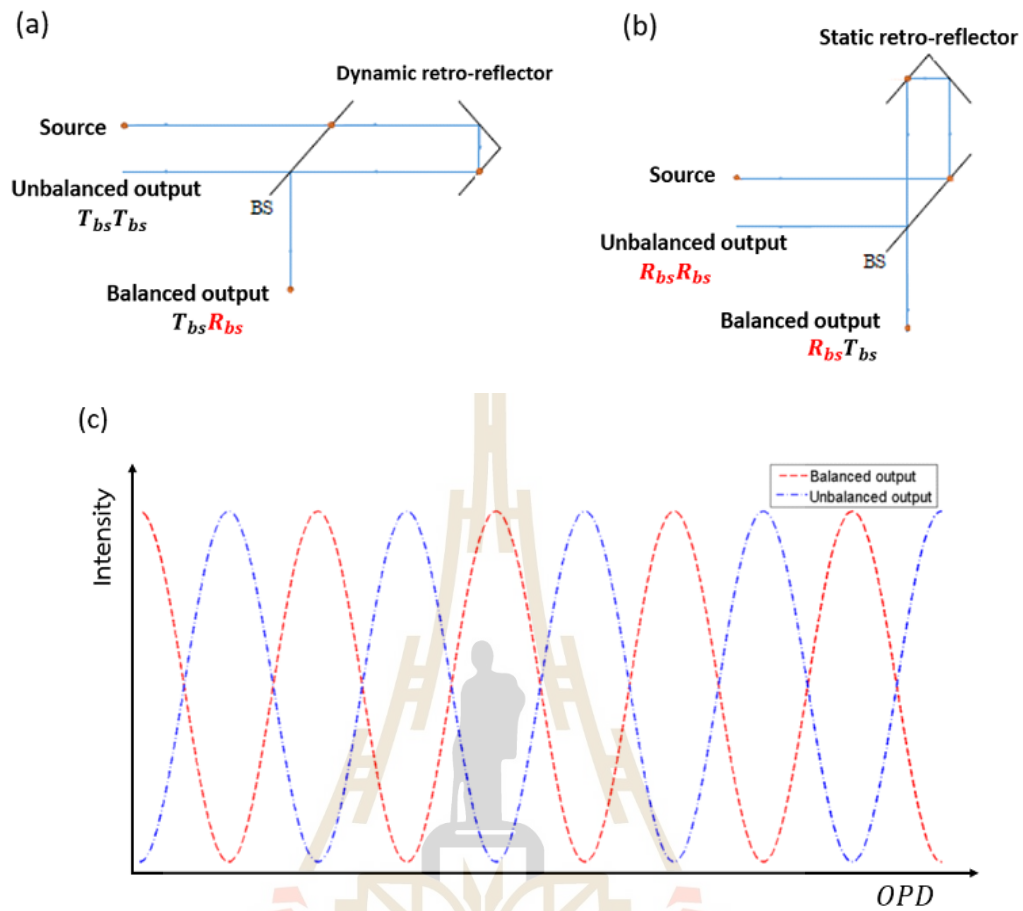
Figure 2.4 (a) The schematic illustrated the beam path of channel 1 in the dynamic arm. (b) The schematic illustrated the beam path of channel 2 in static arm (Libert, 2016). (c) An illustration of intensity detected for monochromatic source in balanced (red) and unbalanced (blue) outputs with the phase shift of pi.

The beam paths of the balanced output are similar to the path that was explained in the classical Michelson interferometer in the previous Section. The expression of the intensity that is detected at the balanced output is thus following an Equation (2.13) as

$$I_{1P}(\sigma_0, OPD) = 2R_{bs}R_M T_{bs}I_0(1 + cos(2\pi\sigma_0 OPD)). \qquad (2.14)$$

The phase is changed by π on the reflection path (Born and Wolf, 1999). In the balanced output, the beam paths of channel 1 and channel 2 face the BS with one reflection and one transmission, with a total phase shift equal to π. In the unbalanced output, there are two reflections in the beam path of channel 1 corresponding to the total phase shift of 2π while there is no phase shift in the channel 2. Therefore, there are phase shift equal to π between each channel in both balanced and unbalanced outputs, as illustrated in Figure 2.4(c).

The detected intensity at the unbalanced output is out of phase equal to π with respect to the balanced output but both outputs contain the same information (Libert, 2016), which can be written as

$$I_{2P}(\sigma_0, OPD) = 2R_{bs}R_M T_{bs}I_0(1 - cos(2\pi\sigma_0 OPD)). \qquad (2.15)$$

The output at the balanced detector is derived by the subtraction the unbalanced output from the balanced output. By substituting Equation (2.14) and (2.15) into Equation (2.16), the detected intensity result is obtained as

$$I_B(\sigma_0, OPD) = I_{2P}(\sigma_0, OPD) - I_{1P}(\sigma_0, OPD) = 4I_0 R_{bs}R_M T_{bs} \cos(2\pi\sigma_0 OPD). \qquad (2.16)$$

The comparison between the interferogram outputs that are retrieved from classical interferometer and from the balanced detection is illustrated in Figure 2.5(a) and (b), respectively. The DC offset of the interferogram output in the classical interferometer can be eliminated by the balanced detection (Soldevila et al., 2016). Furthermore, the amplitude of modulated signal in the balanced output is twice larger than the output in classical interferometer. Therefore, the balanced detection of the instrument design is one of the solutions for improving of signal-to-noise ratio of the system (P. Zhang et al., 2021).
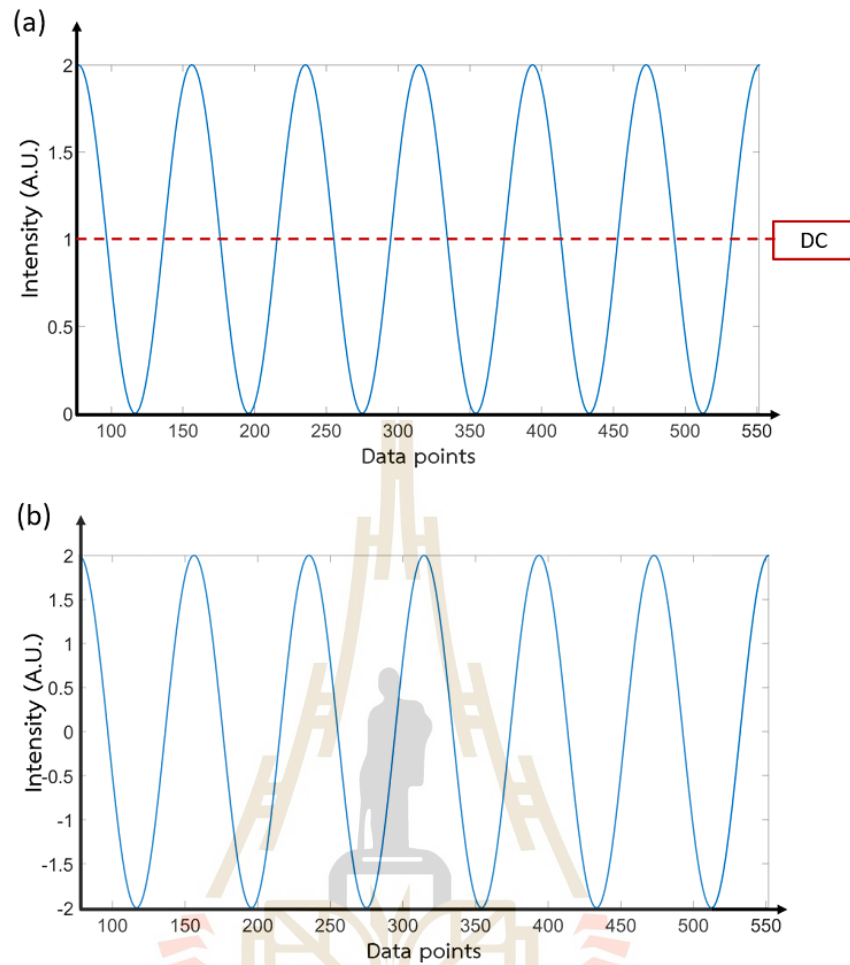
Figure 2.5 The comparison of detected interferogram results between (a) classical output and (b) balanced output of Michelson interferometer.

The Equation (2.16) can be simplified by grouping the all coefficients in front of the bracket as a factor $S(\sigma_0)$, which is quantified in a single frequency-dependent factor and thus obtain the result as

$$I_B(\sigma_0, OPD) = S(\sigma_0) \cos(2\pi\sigma_0 OPD). \qquad (2.17)$$

The result in Equation (2.17) shows the advantages of the implementation of balanced detector in the FTS system including of eliminating most of the DC part and improving the signal to noise ratio of the signal.

2.2.3 Michelson interferometer with broadband source

Generally, the FTS system has been implemented with a broadband source, which provides a continuous spectrum of a large range of frequencies. The interferogram obtained from the broadband source is the integration of each interferogram in a specified frequency with a weight factor of spectral irradiance, which quantifies the amount of radiated power through a unit area at frequency σ. The FTS measures the spectral irradiance of the source along the frequency interval as defined as spectrum.

The measured spectral irradiance is defined by $S(\sigma)$. The intensity can be obtained by integrating an Equation (2.17) over all the frequencies σ and is written as

$$I(OPD) = \int_0^\infty S(\sigma) \cos(2\pi\sigma OPD) \, d\sigma. \qquad (2.18)$$

The two above equations consider only on the positive OPD range and also positive frequency, which corresponds to the single side interferogram. Ideally, the interferogram is an even function of the OPD as $I(-OPD) = I(OPD)$, meaning that the double side interferogram is obtained by measurement of symmetrical OPD range around ZPD and can be expresses in the form as

$$I(OPD) = \frac{1}{2}\int_{-\infty}^\infty S(\sigma) \cos(2\pi\sigma OPD) \, d\sigma. \qquad (2.19)$$

2.2.4 Coherence and Fourier transform theorem

The spectral shape of an ideal monochromatic source is represented by a delta function with single frequency and provides the infinite sinusoidal variation, as respectively illustrated in Figure 2.6(a) and 2.6(b).

Typically, the monochromatic source has the spectral line represented as a band of frequencies, which is never infinitely sharp known as natural linewidth (E. Hecht, 2002), as represented in Figure 2.6(c). The interference obtained from this effect is detected with pulses duration of fringe dropped. The range between the ZPD (OPD =0) to the half maximum of amplitude of the fringe variation is defined as coherence length (Δl_c), as illustrated Figure 2.6(d). As a consequence, the spectrum of broadband source provides more limited coherence length, as shown in Figure 2.6(e) and 2.6(f), respectively.
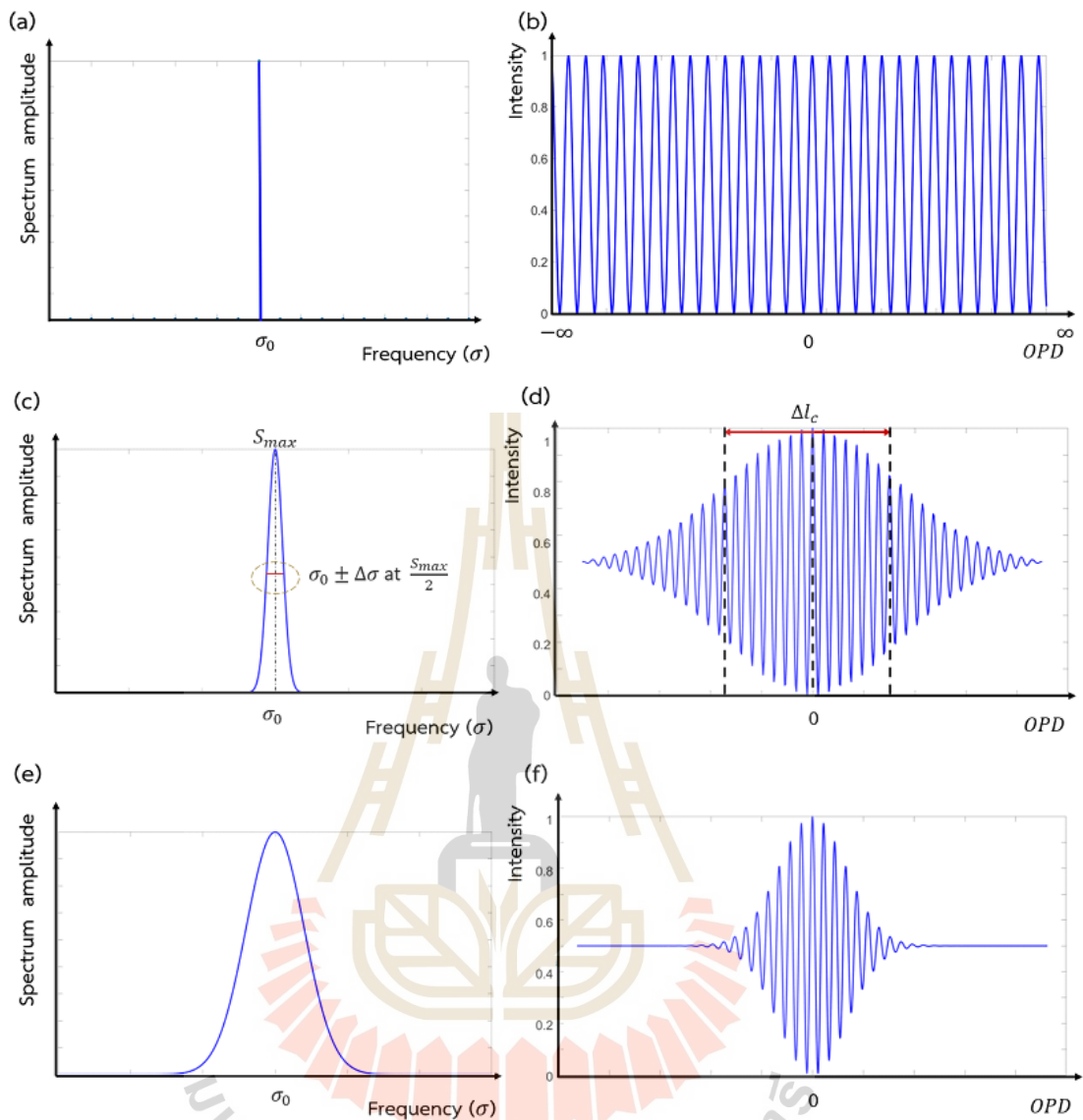
Figure 2.6 (a) An ideal spectral line as a delta function of monochromatic source and (b) its interference in the form of infinite sinusoidal wave. (c) A spectral line of conventional monochromatic source with the spectral linewidth, and (d) its interference variation, including the defined of coherence length. (e) The spectrum line shape of the broadband source, which corresponding to its interference plotted in (f).

The coherence length is related to the spectrum bandwidth as defined as $\Delta z_c = \frac{\lambda^2}{\Delta \lambda}$ (Born and Wolf, 1999), where $\Delta \lambda$ defines wavelength stability of the source. The laser or monochromatic source with narrow bandwidth has a larger coherence length than the source with broader bandwidth, such as the Sun or the other

broadband sources, implying that the broader spectral bandwidth provides the shorter coherent length.

Practically, Equation (2.19) is an even function, which can be expressed in the Fourier transform relation as

$$I(OPD) = \frac{1}{2}\int_{-\infty}^{\infty} S(\sigma)e^{-i2\pi\sigma OPD}\, d\sigma = \mathcal{F}(S(\sigma)). \qquad (2.20)$$

The spectrum function is thus obtained by taking the inverse Fourier Transform to the interferogram in Equation (2.20) (Bracewell, 2000) as

$$S(\sigma) = \frac{1}{2}\int_{-\infty}^{\infty} I(OPD)e^{i2\pi\sigma OPD}\, dOPD = \mathcal{F}^{-1}(I(OPD)). \qquad (2.21)$$

The spectrum function $S(\sigma)$ can be retrieved by taking the Fourier transform to the interferogram function $I(OPD)$ and vice versa. In the FTS application, the interferogram output of the interferometer, as illustrated in Figure 2.7(a), is transformed to obtain the spectrum result, as illustrated in Figure 2.7(b).
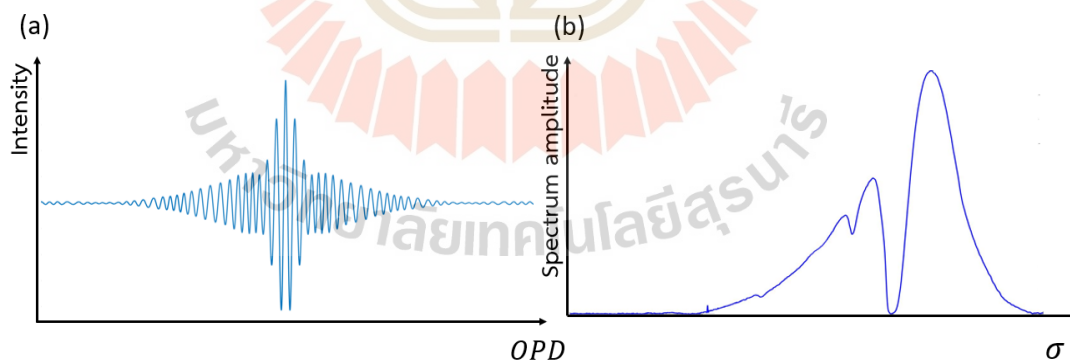
Figure 2.7   An example of interferogram of a Halogen-tungsten source (a) and its spectrum result after taking the Fourier transform (b).

2.3 Sampling theorem

In order to convert the interferogram to obtain the spectrum result, the modern digital computer has been used as an essential tool for the FTS by algorithm, known as Fast Fourier Transform (FFT) (Brault, 1985). The data-acquisition in the FTS system

acquires the signal in a discrete time. The recorded signal in each discrete time step is called "sampling" (Brault, 1985) that will be explained in this Section hereafter.

To illustrate this effect, the interferogram will be multiplied function by the Dirac delta comb function, which is represented by a unit-area of delta function (δ), centered at the origin and spaced one unit apart. The expression of comb function is illustrated in Figure 2.8(a) and can be written in the form of

$$comb(x) = \sum_{n=-\infty}^{\infty} \delta(x - n), \tag{2.22}$$

where n is an integer.

The scaled property of comb function can be expressed as

$$comb(\tfrac{x}{b}) = \sum_{n=-\infty}^{\infty} \delta(x - nb). \tag{2.23}$$

The expression of scale property in Equation (2.23) describes an array of unit area of delta function, centered at the origin and spaced b apart, as illustrated in Figure 2.8(b).
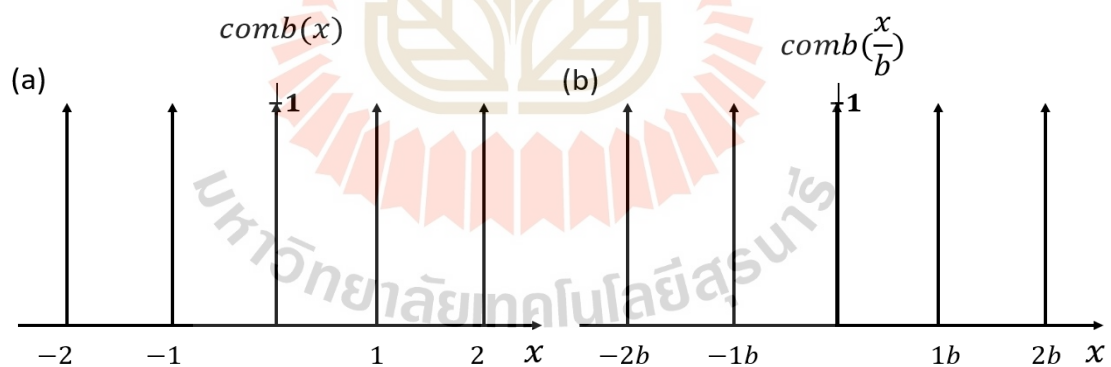
Figure 2.8   An illustration of *comb* function in the form of *comb(x)* in (a) and the expression of *comb(x/b)* function in (b).

Consider the FTS system, the interferogram has been recorded in a constant interval of retardation. As illustrated in Figure 2.9(a), the interferogram is recorded with the total length equal to OPD and sampled in a uniform interval equal to

$$\Delta OPD = \frac{OPD}{N_{pixel}} \ , \tag{2.24}$$

where N_{pixel} denotes the number of sampling in the acquiring data-acquisition.
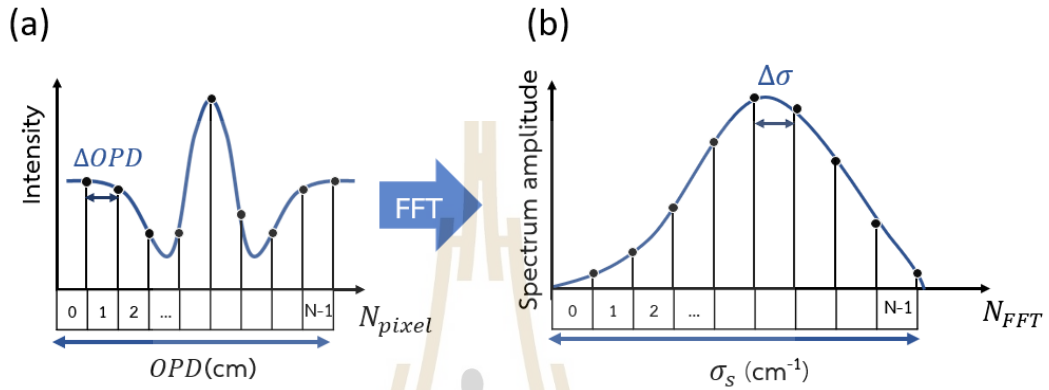
Figure 2.9   An illustration of (a) The discrete samples recorded interference signal in space domain and its obtained spectrum (b) after taking FFT in spectrum domain.

The interpretation of discrete sampling interferogram (I_d) that sampled in the interval equal to ΔOPD is described by the product of continuous interferogram and the sampling in *comb* function, which can be written as

$$I_d(OPD) = I(OPD) \cdot comb(\frac{OPD}{\Delta OPD}). \tag{2.25}$$

It can be expressed in another form following an Equation (2.23), as

$$I_d(OPD) = \sum_{n=-1}^{Npixel} I(OPD - n\Delta OPD). \tag{2.26}$$

The spectrum function was obtained from the FFT of the discrete sampling interferogram $I_d(OPD)$. The Fourier transform of the comb function spaced interval

equal to $\frac{1}{x}$, as illustrated in Figure 2.10(a), is another comb function at an opposed period equal to x, as illustrated in Figure 2.10(b).
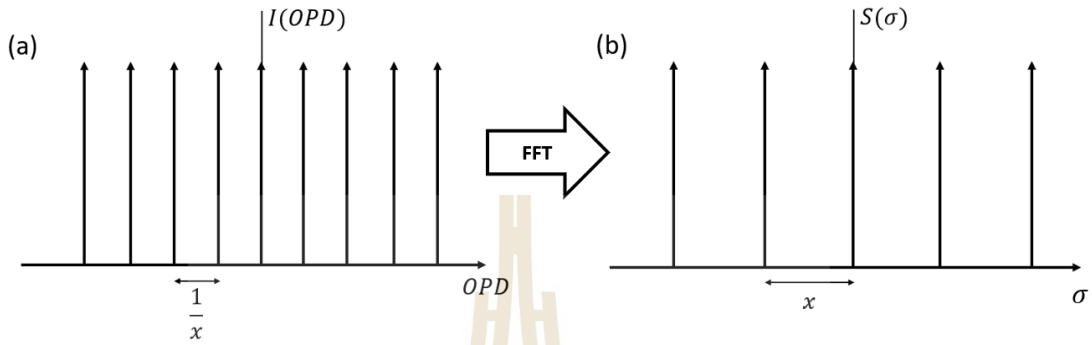
Figure 2.10   (a) the *comb* function with a period of *1/x* and (b) its Fourier transform of another *comb* function with a period of *x*.

Therefore, after taking the FFT to Equation (2.26), the spectrum function is thus obtained as illustrated in Figure 2.9(b) and expressed as

$$S_d(\sigma) = \sum_{n=1}^{Npixel} S(\sigma - \frac{n}{\Delta OPD}) = \sum_{n=1}^{Npixel} S(\sigma - n\sigma_s). \qquad (2.27)$$

Notice that the relation $\sigma_s = \frac{1}{\Delta OPD}$ implies the sampling frequency of the spectrum meaning that a smaller ΔOPD is required in order to observe the larger σ_s.

The spectrum will be repeatable sampled σ_s. To avoid overlap across the frequency range between 0 and σ_{max}, the spectrum needs a frequency coverage of at least $2\sigma_{max}$ as known as "Nyquist frequency" (Dondurur, 2018). A poorly sampled interferogram leads the spectrum folding of negative frequencies, which prevents the identification of the real shape of original spectrum. The expression of sampling interferogram under this criterion can be expressed as

$$\Delta OPD \leq \frac{1}{2\sigma_{max}} = \frac{\lambda_{min}}{2}, \qquad (2.28)$$

where σ_{max} defines the maximum frequency of the source that is related to the minimum wavelength $\lambda_{min} = \frac{1}{\sigma_{max}}$.

The spectrum interval or the frequency spacing can be calculated as

$$\Delta\sigma \ = \frac{\sigma_s}{N_{FFT}} = \frac{1}{N_{FFT} \cdot \Delta OPD}, \qquad (2.29)$$

where N_{FFT} is the number of samples in the spectrum domain.

2.4 Effect of finite OPD

In this Section, some phenomena that have been approached in the realistic FTS measurements are described. Following Equation (2.26), the spectrum function that is obtained by the integral boundary of the scan range of interferogram between $-\infty$ and ∞ becomes unrealistic in the real measurement. In realistic, the FTS system has been operated in the finite OPD between $-OPD_{max}$ and OPD_{max}, where OPD_{max} defines the maximum OPD that is allowed in the system.

Let's consider the truncated interferogram obtained from the monochromatic, as illustrated in Figure 2.11(a). The expressed interferogram function can be derived by multiplying Equation (2.26) by the rectangular or boxcar function (Π), as

$$I_{rect}(OPD) = I_d(OPD) \cdot \Pi(OPD), \qquad (2.30)$$

where

$$\Pi(OPD) = \begin{cases} 1 \,; OPD \le |OPD_{max}| \\ \ 0 \,; otherwise \end{cases}. \qquad (2.31)$$

The spectrum function of this finite range is obtained by taking Fourier transform on the Equation (2.30), which can be expressed as

$$S_{rect}(\sigma_0) = \mathcal{F}(I_{rect}(OPD)) = \mathcal{F}(I_d(OPD) \otimes \mathcal{F}(\Pi(OPD)). \qquad (2.32)$$

The spectrum result obtained is the sinc function, which can be written as

$$S_{rect}(\sigma_0) = S(\sigma_0) \otimes sinc(2\pi\sigma_0 OPD_{max}). \qquad (2.33)$$
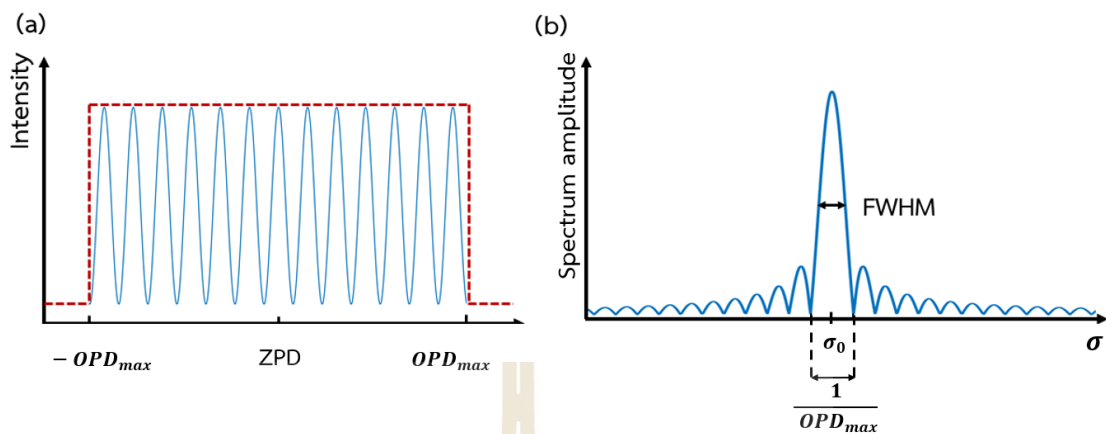
Figure 2.11 (a) An illustration of the truncated interferogram in the truncated range and (b) A result of its Fourier transform of sinc function.

Figure 2.11(a) shows the limitation in finite path difference which is represented as a truncation of the cosine interferogram. The Fourier transform of this effect in the sinc function is shown in Figure 2.11(b). The first main lobe of the sinc function centered about σ_0 provides the frequency width equal to $\frac{1}{OPD_{max}}$. The sinc function can be considered as the instrument line shape (ILS) function which can be used to verify the system performance through the measured of the Full Width at Half Maximum (FWHM) of the spectrum function. The theoretical FWHM of the ILS that measured in centimeter unit can be calculated by

$$\text{FWHM}_{ILS} = \frac{1.207}{2OPD_{max}}.$$ (2.34)

2.5 Sampling error

Ideally, the FFT has been implemented on signals that are sampled in a uniform interval, meaning that the translation of the dynamic mirror is required to be perfectly linear. The interferogram signals are acquired from FTS system in the function of time varying signal. The timestamps are recorded in a uniform time interval. The increment sampling in path difference of two mirrors relates to the translation velocity of the dynamic mirror. In reality, the dynamic mirror is driven by the translation stage which contains the acceleration to force from the steady position until reach the specified velocity and the retardation for the stopping motion. For this reason, the OPD between two mirrors in the interferometer system is considered to be non-

uniform interval and caused the sampling position error due to the velocity fluctuation in dynamic mirror.

Let consider a monochromatic source, the finite OPD range that is obtained from the measurement is expressed as

$$OPD(\Delta V, \tau) = 2(V_0 + \Delta V(t))\tau,$$ (2.35)

where V_0 defines the constant velocity of the dynamic mirror along the displacement. ΔV is the velocity error induced by the acceleration and retardation in the translation stage. τ is time delay along the measurement.

Therefore, the interferogram due to the velocity error can be expressed as

$$I'(\Delta V, \tau)) = I(OPD_0 + \Delta V \cdot \tau),$$ (2.36)

where $OPD_0 = 2V_0\tau$.

The expression of the interferogram, corresponding to sampling position error (ε), can be written as (McCurnin, 1981)

$$I'_\varepsilon(\tau)) = I(OPD_0 + \varepsilon(\Delta V, \tau)),$$ (2.37)

where ε defines the sampling position error in a function of OPD.

For a small error, the first order approximation of truncated Taylor series expansion can be applied as

$$I'_\varepsilon(OPD) \approx I(OPD_0) + \varepsilon(\Delta V, \tau)\frac{d(IOPD_0))}{dOPD}.$$ (2.38)

The spectrum result that is obtained after taking FFT can be expressed as

$$S'_\varepsilon(\sigma) = S(\sigma) + \varepsilon(\sigma)\otimes 2\pi i\sigma S(\sigma),$$ (2.39)

where $\otimes$ defines the convolution operator. The term $2\pi i\sigma$ implies the phase distortion that are introduced from sampling position errors ε.

In reality, the interferogram signals are sampled with the sampling position errors due to the translation of the dynamic mirror, which contain acceleration from a stop motion to reach the specified velocity and retardation to stop the motion. The translating stage controls the dynamic mirror with undecided values of both acceleration and retardation. When the scanning velocity varies randomly about the central value V, it will affect the manifested spectrum as a noise, with the highest noise amplitude occurring at σ_0 (Griffiths et al., 2007).

To illustrate this situation, the sampling position errors by simulation of the two origins have been analyzed, including of the velocity fluctuation and the sampling jitter that will be presented hereafter.

2.5.1 The sampling position error due to the velocity fluctuation

To clarify this effect, I have simulated this error under the consideration of a monochromatic source at wavelength equal to λ = 633.178 nm with a finite path range of $OPD = ZPD \pm 1$ mm. The simulation of the sampling position errors (ε) is illustrated in the left-panel of Figure 2.12. ε was assumed to be related to the velocity fluctuation. It is rapidly increased in the beginning due to an acceleration in the translating stage from the static position. Then, it becomes smaller until it reaches the specified velocity and gives the smallest errors ($\varepsilon \cong 0$) at the ZPD, and it thus turns to increase again due to the effect of deacceleration until the mirror is stopped. The incrementations of ε is interpreted in a time dependent of uniform symmetrical parabolic function as

$$\varepsilon(\tau) = \varepsilon_i \tau^2 ,$$
(2.39)

where ε_i defines the order of magnitude of an error.

The simulation of four order of magnitudes of ε have varied, including of $\varepsilon_1 \propto 10^{-4}, \varepsilon_2 \propto 10^{-5}, \varepsilon_3 \propto 10^{-6}$, and $\varepsilon_4 \propto 10^{-7}$, as respectively presented in (a), (b), (c) and (d) on the left-panel of Figure 2.12.
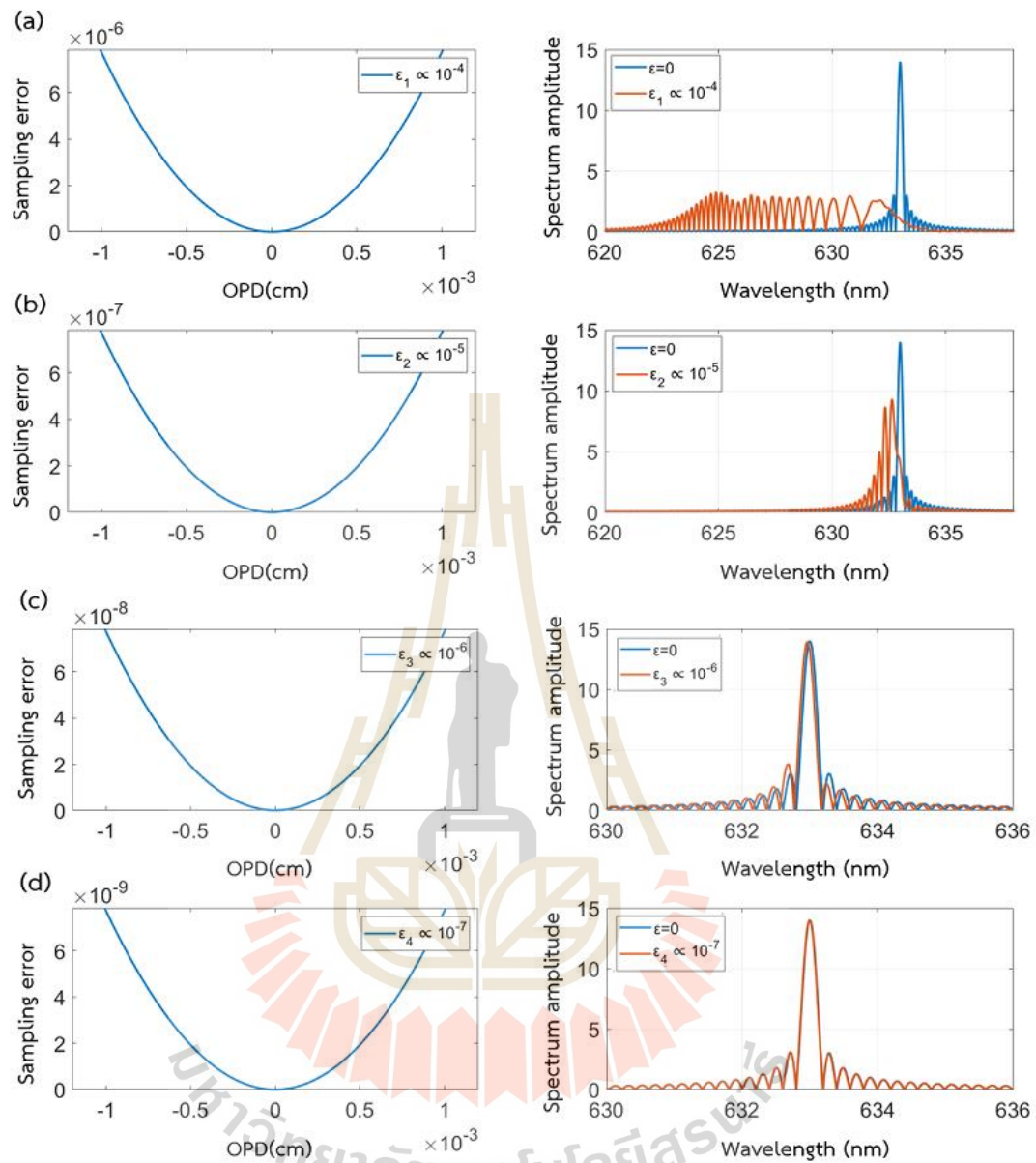
Figure 2.12 Simulations of position sampling errors due to velocity fluctuation with four order of magnitudes in the left-panel corresponding to their spectral results in the right-panel.

The right-panel of Figure 2.12, shows the spectral results corresponding with each ε in the left-panel. The theoretical spectrum in the blue lines shows the line shape of a monochromatic source at the simulated central wavelength (CTW) equal to 633.178 nm. First, the largest error $\varepsilon_1 \propto 10^{-4}$, as illustrated in Figure 2.12(a), shows many spurious frequencies that formed to be the large bandwidth. Second, the smaller

error $\varepsilon_2 \propto 10^{-5}$, as illustrated in Figure 2.12(b), provides the smaller number of spurious frequencies than ε_1. In the third order, $\varepsilon_3 \propto 10^{-5}$, as illustrated in Figure 2.12(c), provides the spectral line shape closed to the theoretical line shape with a very small shift of 0.04 nm from the theoretical CTW. Finally, the fourth order, which is the smallest value at $\varepsilon_4 \propto 10^{-5}$, as illustrated in Figure 2.12(d), gives the spectral line shape and CTW to be the same as the theoretical spectrum.

2.5.2 The sampling position error due to sampling jitter

The sampling position error can be induced by the jitter motion of the mirror. The sampling jitter occur during the translation of the mirror due to the non-uniform carrying of the translating stage. The term ε is interpreted in a random variation in a function as

$$\varepsilon(\tau) = \beta\tau, \tag{2.40}$$

where β is independent random variable.

The simulation of the sampling position errors due to this effect is illustrated in Figure 2.13. The jitter is assumed to be randomly occurred along the translation. The left-panel illustrates the two random jitters that have been created and plotted in a function of position jitter varying with OPD, while the spectral result with spurious frequencies of each jitter is presented in the red line of right-panel compared to the theoretical spectrum in the blue line.
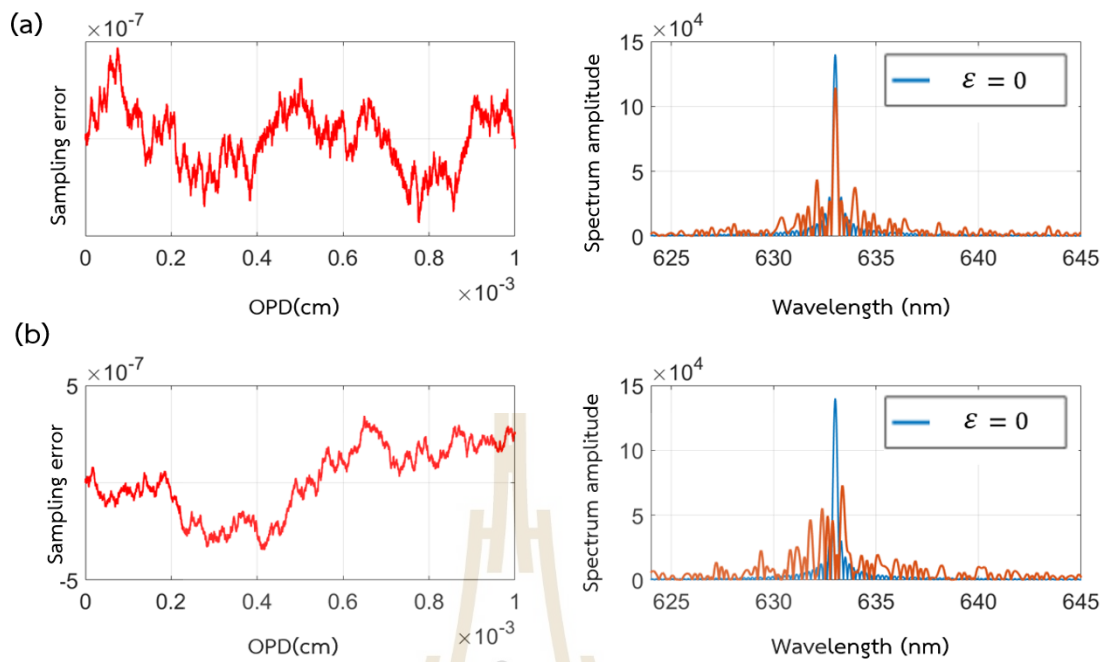
Figure 2.13　Simulations of sampling errors of non-uniform *OPD* in a function of random jitter position in the left-panel, which are corresponded to their spectral results in the right-panel.

The sampling jitter results in Figure 2.13(b) have been created with higher random amplitude than in Figure 2.13(a) or $\beta_b > \beta_a$. These result show that the spurious frequencies in the spectrum are increased proportional to the amplitude of random jitter.

2.6 Fringe contrast

The characterization of interference fringe modulation of interferogram that is retrieved from the interferometer is quantified by the fringe visibility or fringe contrast. It is determined by the average cross-section of the intensity distribution along the interference pattern (Deng and Chu, 2017). The spatial coherence value is calculated through the fringe contrast (C) as (Erickson and Brown, 1967)

$$C = \frac{(I_{max} - I_{min})}{(I_{max} + I_{min})}, \tag{2.41}$$

where I_{max} and I_{min} are the maximum and minimum intensity of the fringe modulation, respectively. The system with higher C will generally provide a larger signal to noise ratio and thus gain the measurement accuracy (Y. Zhang et al., 2010).
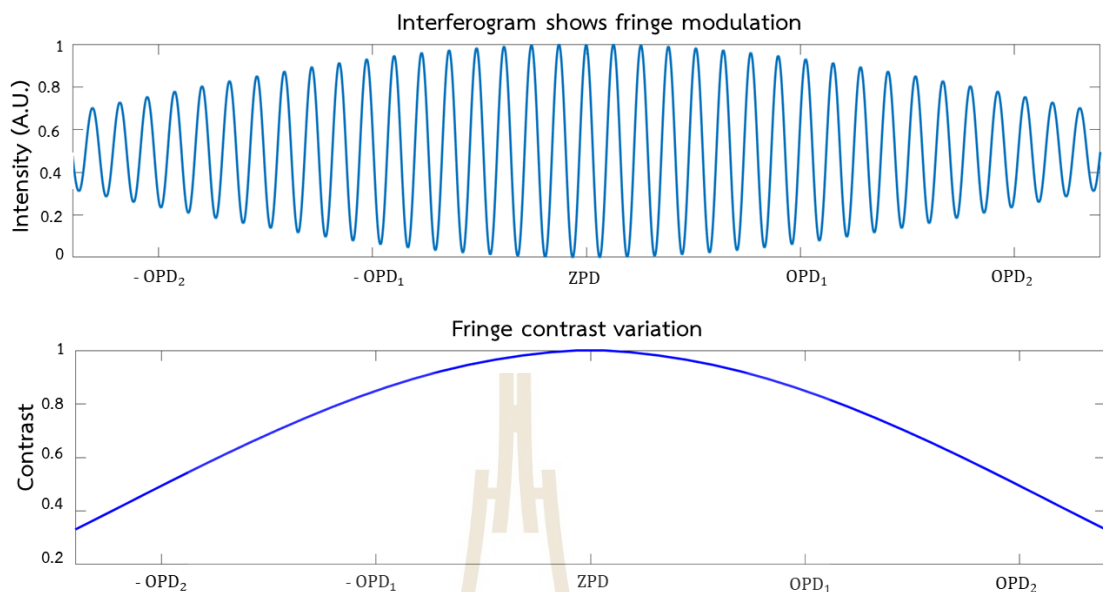
Figure 2.14   Simulations illustrated fringe modulations interferogram (a) and corresponded to the measured of contrast variation shown in (b).

When I_{min} is much smaller than I_{max}, the high contrast is observed as $C \approx 1$ which is generally observed close to ZPD. The fringe modulations are clearly observed in the case of $C > 0.5$, while $C < 0.2$ implied that the bright and dark patterns in fringe modulation are difficult to observe (Beaudry; D. and Milster.).

Figure 2.14(a) illustrates the interferogram simulation that obviously shows large fringe modulations while the fringe contrast variation corresponding to this modulation is obtained by Equation (2.56) and presented in the Figure 2.14(b).

In this Section, I have identified the two effects that limit the to the contrast of the system, including of the effect spatial extension of the fiber core, and the effect of the tilt in the dynamic mirror during the displacement (Artsang et al., 2022).

Notice that one more possible origin that limit the contrast is the effect of coherence length due of the bandwidth of monochromatic source, as described in the Section 2.2.4. The coherence length is related to the spectrum bandwidth as defined as $l_c = \frac{c}{\Delta f}$ (Born and Wolf, 1999), where Δf is the frequency bandwidth of the source spectrum. Conventionally a laser source has a long range of coherence length. For example, the stabilized laser at central wavelength 633.178 nm that was applied in

the experimental setup has coherence length longer than 1 meter. Therefore, this effect is negligible for the investigation of contrast loss in the range of few centimeters.

2.6.1 Effect of the spatial extension of the fiber core

In the fiber-fed FTS system, the beam reaches the interferometer through a multi-mode fiber. The beam is diverged at the fiber output and then collimated by the collimator. The size of collimated beam is increased with the large core diameter. The spatial extension of the fiber core introduces a variation of the OPD that impacts the contrast performance (Griffiths et al., 2007).
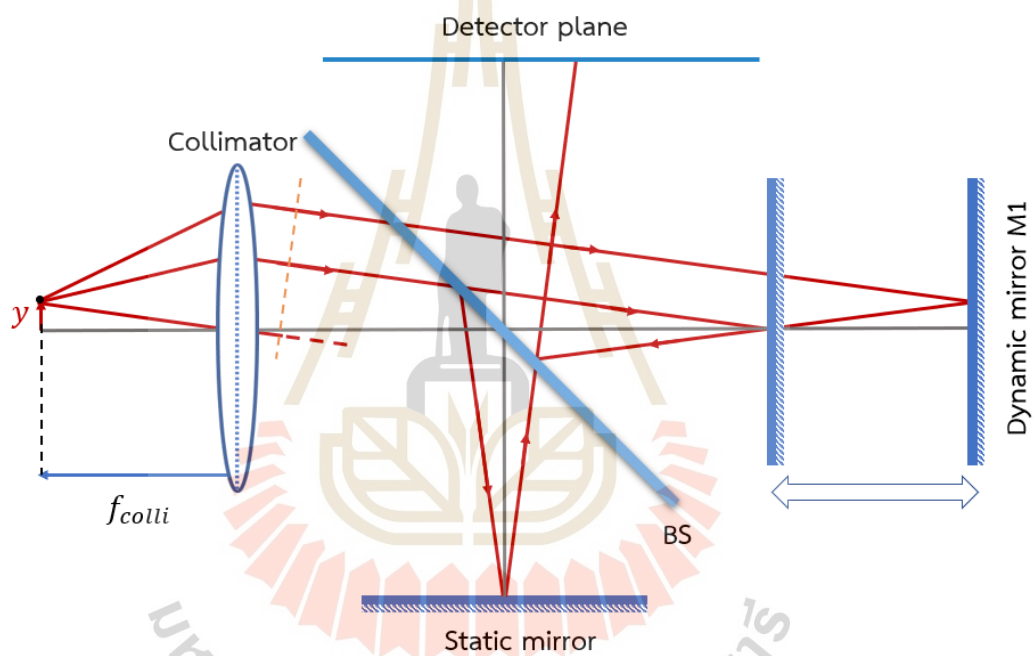
Figure 2.15   A schematic of source that is injected by the large core fiber from the source plane and propagated to the interferometer with the angle of incident due to the effect extended source.

As illustrated in Figure 2.15, the light source is injected through the fiber with the core size y to the FTS system with the angle of incident (θ). This angle induced the off-axis rays propagated and reached the detector, as plotted in the red lines, and thus caused the OPD variation along the fringe modulations.

The channel 1 defines the beam that is reflected by BS toward the dynamic mirror M1 while the channel 2 defines the beam that is transmitted through BS toward the static mirror M2. The OPD at any incident angle is quantified by the difference

between the OPD of beam that propagated through channel 1 and the OPD of beam that propagated through channel 2.

As illustrated in Figure 2.16, the OPD of the beam in channel 1 is quantified as ac', while the OPD of the beam in channel 2 is expresses as $2bc$ or $2ab$. The expression of total OPD due to the effect of off-axis ray is thus written in the form as

$$OPD' = 2bc - ac' . \tag{2.42}$$
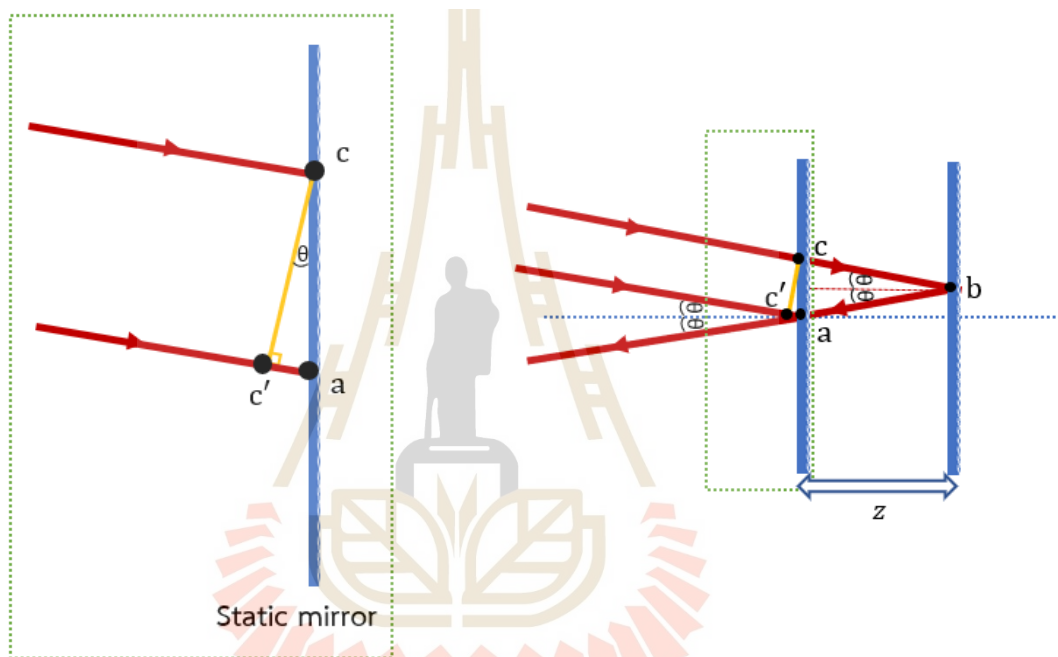
Figure 2.16 A schematic of the geometrical path of the off-axis beam that propagated to the dynamic mirror.

Let z represents to the on-axis distance path between channel 1 and channel 2, implying that the on-axis OPD is equal to $2z$. By applying the trigonometric identities, the first term in Equation (2.42) can be expressed as

$$2bc = \frac{2z}{cos\theta} . \tag{2.43}$$

To derive the second term, the expression can be deduced that $ac = 2bc \cdot sin\theta$ and $ac' = ac \cdot sin\theta$. Therefore, the second term of Equation (2.42) is expressed as

$$ac' = 2bc \cdot sin^2\,\theta. \tag{2.44}$$

By substituting Equation (2.43) and (2.44) into the Equation (2.42), the OPD of the off-axis beam can be expressed as

$$OPD' = \frac{2z}{cos\theta}(1 - sin^2\,\theta) = 2zcos\theta = OPD \cdot cos\theta. \tag{2.45}$$

The OPD result in the off-axis rays affects to the interferogram variation and thus influences the contrast loss.

2.6.2 Effect of the tilt in the dynamic mirror during the displacement

The quality of the measured interferogram on a Michelson interferometer depends on the maintained alignment between the plane of static mirror relative to the plane of dynamic mirror during the displacement. When the dynamic mirror is held at a different angle than the static mirror relative to the plane of the BS, both beams will hit the plane of the detector at a different position, as illustrated in Figure 2.17. If the images from the static and dynamic mirrors are not centered at the same point on the detector, fringe contrast can be drastically reduced (Griffiths et al., 2007).

This effect involves the fact that the drive mechanism of the stage that controls the movement of the dynamic mirror can not maintain the angle relative to BS along the translation.

Consider the effect of a mirror tilt equal to α radians on a collimated beam with diameter d_{colli}, as illustrated in Figure 2.17. The increased in OPD between the two the extreme rays A and B is expressed as twice of retardation as (Griffiths et al., 2007)

$$l = 2 \cdot \frac{d_{colli}}{2}tan(\alpha) = d_{colli}\,tan(\alpha). \tag{2.46}$$

In general, the value of pitch and roll in the translating stage is in the order of ten microradians. (For example, our translation stage is NEWPORT ESP 301 translating stage has a value of maximum pitch and roll equal to of 37 microradians). I thus apply the small angle approximation to Equation (2.46) and expressed the OPD variation due to the effect of mirror tilt as
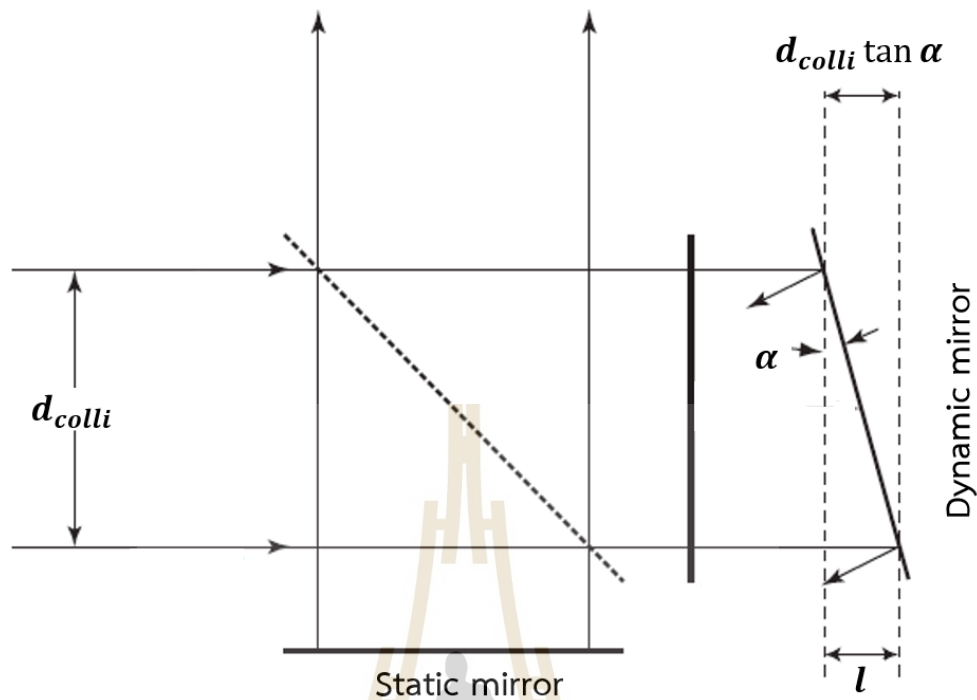
Figure 2.17 A schematic of Michelson interferometer with an effect of changing the plane of the dynamic mirror of an interferometer during a scan modified from (Griffiths et al., 2007).

$$OPD'' = OPD + l = OPD + d_{colli} \cdot \alpha. \qquad (2.47)$$

The increasing of OPD result in Equation (2.47) due to the effect of dynamic mirror tilt along the translation affects to the loss in fringe modulation (Griffiths et al., 2007) thus influences the contrast loss.

2.7 Spectral quality

2.7.1 The spectral resolution

The fundamental key property to determine the instrument performance is the spectral resolution (R), which is analogous to the spectral resolution of the instrument. The calculation of R at the defined wavelength λ can be calculated by (Massey and Hanson, 2013)

$$R = \frac{\lambda}{\Delta \lambda}, \qquad (2.48)$$

where $\Delta\lambda$ is the smallest wavelength resolved or the minimum separation of two spectral lines. In this thesis, I have analyzed the R of the FTS system by using the two methods

Method I

The smallest wavelength resolved $\Delta\lambda$ has determined by the FWHM of the measured ILS that is obtained at the finite OPD, as described in the Section 2.3 and illustrated in Figure 2.18. When the monochromatic source at CTW $= \lambda_{ref}$ has been implemented, the expression of R is retrieved by following the relation in Equation (2.48) as

$$R = \frac{\lambda_{ref}}{\text{FWHM}_{ILS}} . \tag{2.49}$$
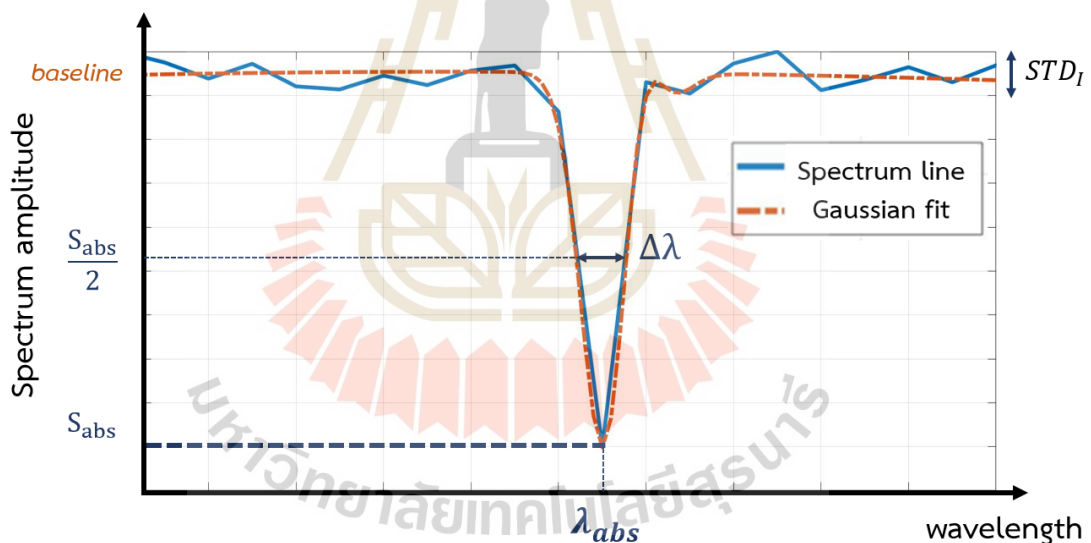
Figure 2.18   An illustration of a region of absorption line in the spectrum for the calculation of the spectral solution in method II and the signal-to-noise-ratio in method I.

Method II

This method has determined R at the small intrinsic absorption line in the spectrum, as illustrated in Figure 2.18. An absorption line with a depth of absorption

defined as S_{abs} has a wavelength resolved $\Delta\lambda$ measure at the depth $\frac{S_{abs}}{2}$. The calculation of R is expressed in the form of

$$R = \frac{\lambda_{abs}}{\Delta\lambda}. \tag{2.50}$$

2.7.2 The noise contributions and Signal-to-noise ratio

Another key property to determine the instrument performance is the ratio between the signal (S) and noise (STD) of the result of the system, knowing as the Signal-to-Noise-Ratio (SNR).

The noise usually contributes from two important effects, including instrumental effects and environmental effects. The fundamental types of noises have been classified by their nature into two categories. First is the random noise or time-uncorrelated noise, which is generally associated to the photon noise. The examples of random noise sources in the FTS with astronomical observations include detector readout noise, detector dark current noise, background noise, and atmospheric flash noise. The effect of photon noise can be reduced by increasing the photon counts of the signal (Hinse et al., 2015). The second type is related to the systematic nature, such as the alignment of the instrument. There are many sources of this noise that are included along the observation which are difficult to quantify and depend on the alignment of the system.

There are the three methods for the SNR calculation that will be used in this thesis

Method I

This method describes the SNR along the region of an absorption line, as illustrated in Figure 2.18. The depth of the absorption line $|S_{abs}|$ from the reference baseline is considered as the signal while the noise is determined by the standard deviation of the noise nearby this absorption line (STD_I). The SNR is thus expressed as

$$SNR = \frac{|S_{abs}|}{STD_I}. \tag{2.51}$$

Method II

This method is known as the spectral SNR (Lacan et al., 2010), which is determined spectrum of bandpass filter as illustrated in Figure 2.19(a). The noise is

obtained by the standard deviation of the feet of the spectrum, while the signal is considered as the maximum of the spectrum intensity (S_{max}). The SNR that obtained from this method can be in expressed as

$$SNR = \frac{S_{max}}{STD_{II}}.$$

(2.52)

Method III

      This method has determined the selected portion of spectrum and skipped absorption lines. The average of signal variation ($\bar{x}$) represents the signal of the system. The noise is retrieved by the standard deviation of the signal and ignores the feet part of the spectrum, as illustrated in Figure 2.19(b). The SNR that is obtained from this method can be in expressed as (Holmes, 2007)

$$SNR = \frac{\bar{x}}{STD_{III}}.$$

(2.53)
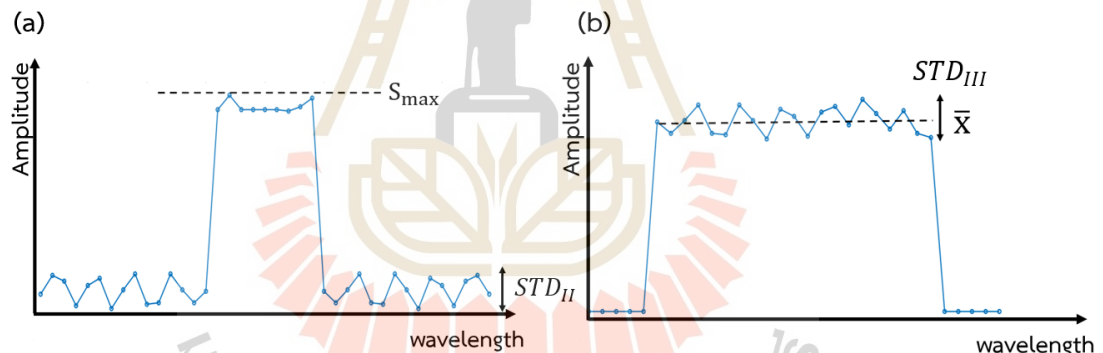
Figure 2.19   An illustration of the signal-to-noise-ratio calculation from the spectrum in method II in (a) and method III in (b).

CHAPTER III

RESEARCH METHODOLOGY

3.1 Instrumental concept

The fiber-fed in developed FTS system has been designed for a ground-based telescope. As illustrated in Figure 3.1, the amount of incoming flux transmitted through the FTS system is related to the Numerical Aperture (NA) of the fiber, as expressed in the geometrical relation as

$$NA = sin\,\emptyset, \tag{3.1}$$

where $\emptyset$ defines the half cone angle of the diverged beam that is injected from the fiber output.
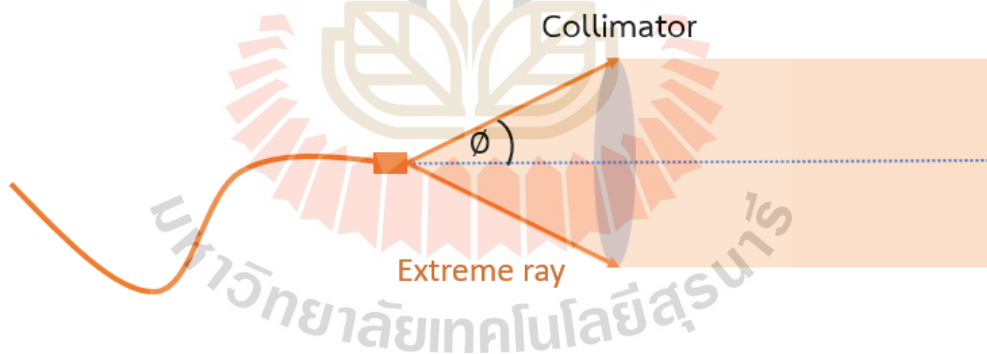
Figure 3.1   Schematic of the injected beam from the fiber output through a collimator.

As illustrated in Figure 3.1, the extreme ray of the divergence beam is limited by the size of the collimator. In our FTS system, the optical fiber that has been selected to connect to the interferometer has an NA equal to 0.22 (FG050LGA, Thorlabs Inc., USA) corresponding to an aperture number ($F_{\#}$) equal to

$$F_{\#Fiber} = (2 \cdot NA)^{-1} \approx 2.27. \tag{3.2}$$

The TNT has clear aperture diameter equal to 2.3 m (Buisset et al., 2015) and the aperture number equal to $F_{\#TNT} = 10$. The TNT collects the star light beam with an autoguiding and directs this beam toward a Guiding and Injection Unit (GIU). The scientific optical fiber is thus connected to the GIU to receive the star flux and direct toward the FTS system that was placed inside the spectrograph laboratory, as illustrated in the schematic of the Figure 3.2.
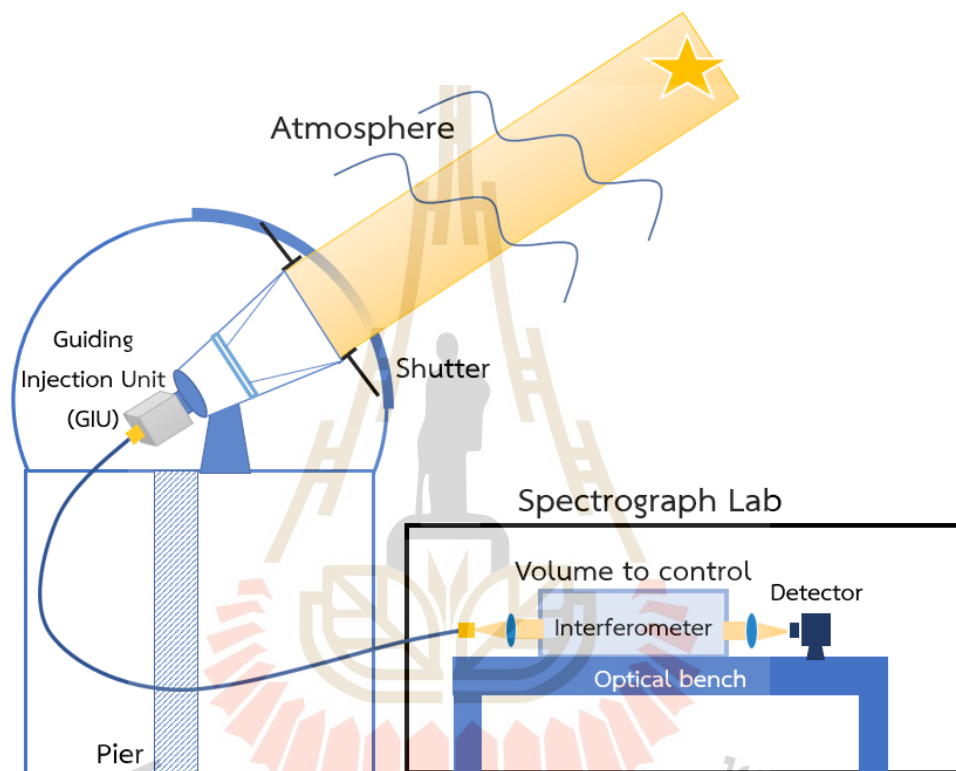
Figure 3.2 A Schematic concept of the proposed fiber-fed FTS system receiving star flux that passed through an atmospheric path. The telescope points and directs the beam flux toward the GIU before reaching the FTS system via multi-mode fiber connection.

In the fiber fed spectrograph system, the size of fiber core is adjusted to fit the size of star image at the telescope focus. The GIU is included in the setup to customize the output beam from the telescope to the scientific fiber connection by following the matching condition of the relation between an aperture number and focal length as

$$\frac{f_{TNT}}{F_{\#\,TNT}} = \frac{f_{Fiber}}{F_{\#\,Fiber}}, \tag{3.3}$$

where f_{TNT} and f_{Fiber} define the focal length of TNT collimator and the focal length of the GIU collimator that will be connected to the fiber, respectively. Therefore, the effective focal length of the TNT is calculated as

$$f_{eff} = F_{\#TNT} \cdot \frac{f_{Fiber}}{F_{\#,Fiber}} = 5.2 \text{ m}. \tag{3.4}$$
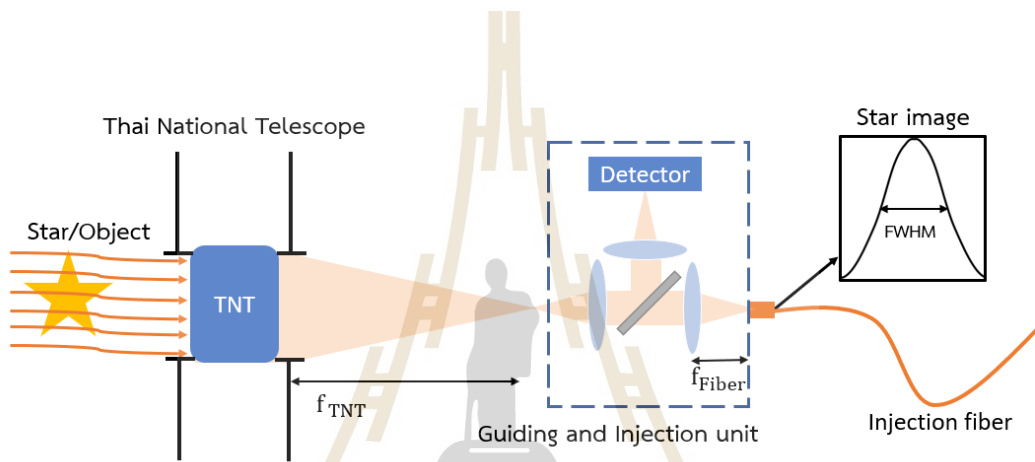
Figure 3.3   An illustration of gathering and receiving flux from the star through the optical fiber to reach the FTS system.

Typically, TNT has the seeing ($\delta\theta_{\text{Seeing}}$) in median conditions approximately equal to 0.9" (Dhillon et al., 2014). In order to include all sky conditions during an observation, the seeing can be determined as $\delta\theta_{\text{Seeing}} \approx 2"$. The star image can be thus estimated from the seeing condition and the telescope focal length (Lhospice et al., 2019) as

$$FWHM_{star} \approx f_{eff} \cdot \delta\theta_{seeing} = 50.4 \times 10^{-6} \text{ rad}. \tag{3.5}$$

Consequently, an optical fiber with a core diameter equal to 50 microns was designed and selected to receive the star flux from the telescope and connect to our FTS setup inside the laboratory.

3.2 Instrument design

3.2.1 Metrology installation

The design of the FTS system includes one scientific channel and one metrology channel, as illustrated in Figure 3.4. The telescope collects the light from the star through GIU directly to the fiber of the scientific channel. The metrology channel is implemented in order to correct the non-linearity scanning of the dynamic mirror.
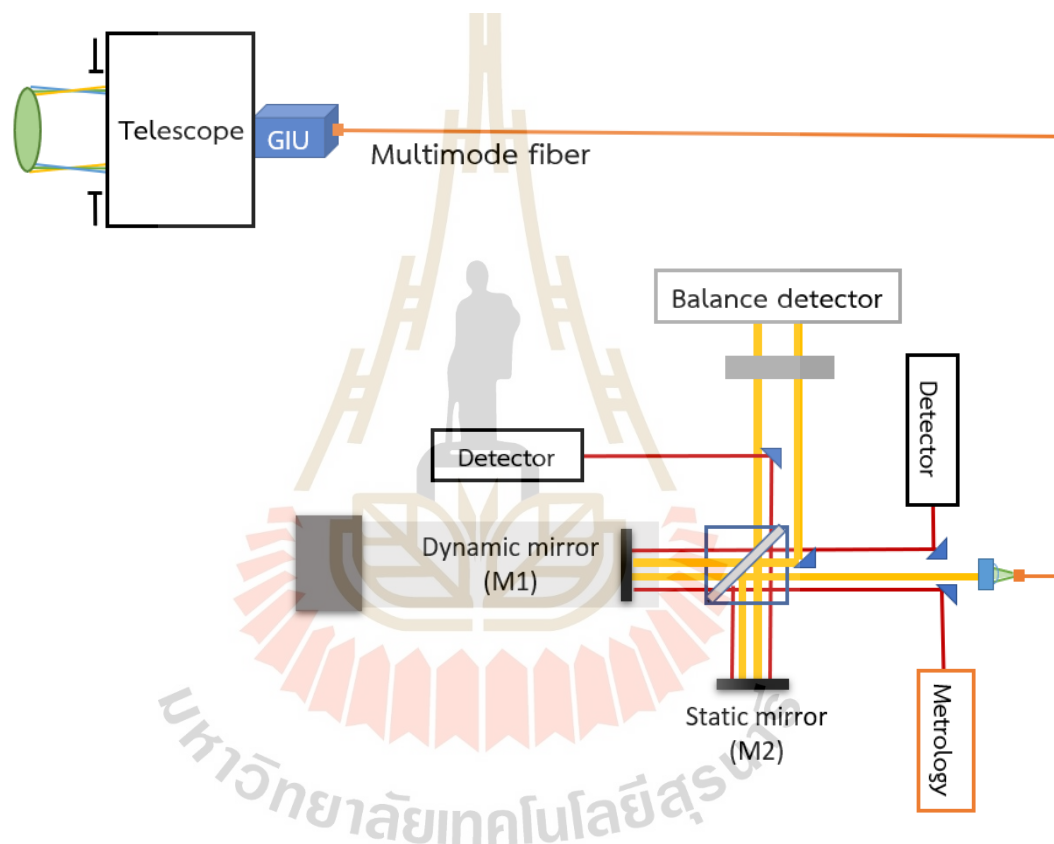
Figure 3.4   A proposed schematic of FTS system receiving flux from telescope through the fiber and with the two outputs.

The path of the light inside the FTS has been described in the Section 2.1 and 2.2. In order to detect the small flux from the star, the FTS was designed to use the commercial balance detector (Model 2307, Newport Inc., USA), which has two ports with 3.4 cm separation (Newport). The system was designed to get the two outputs for this detection. I used the single mode fiber to inject the metrology source through the

system with the similar path as the scientific channel. The two metrology outputs will be detected by the single port of silicon detector.

3.2.2 Two outputs for balanced detection

The design of two outputs interferometer using the two plane mirrors has been applied to the FTS system. By applying a small tilting into the BS as corresponding to in the static mirror, the two outputs are obtained. The beam propagation in channel 1 and channel 2 are separately illustrated in the Figure 3.5(a) and (b), respectively.
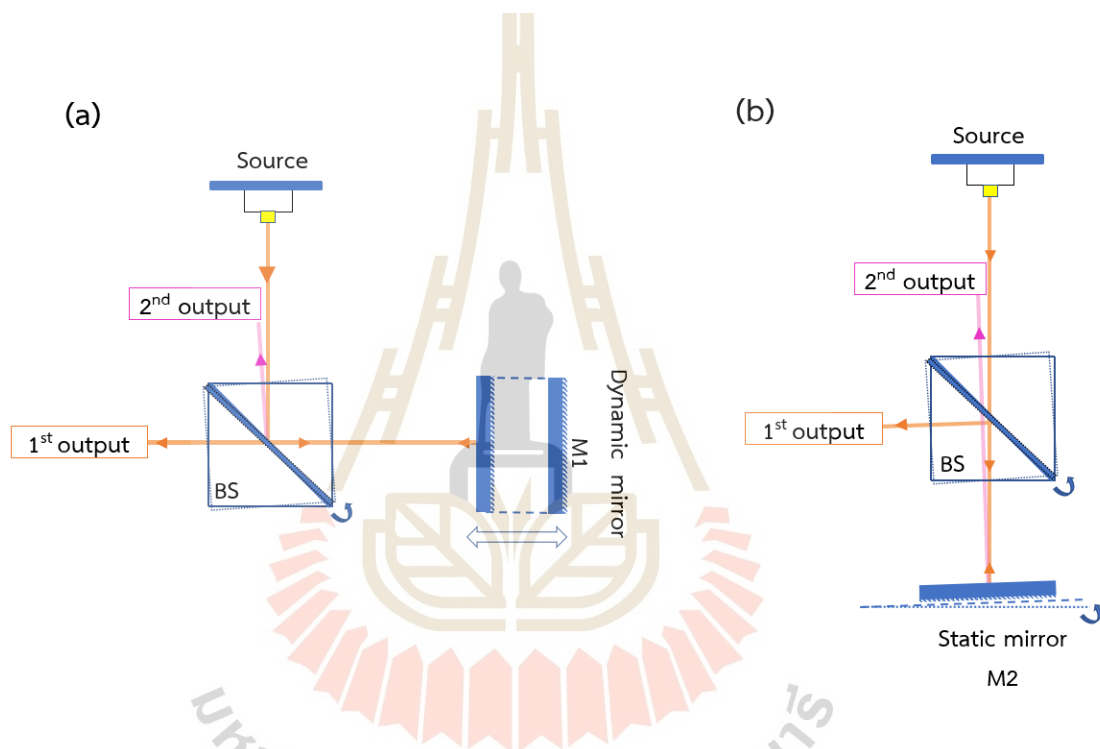
Figure 3.5   (a) Channel 1 beam path: the arm including of only dynamic mirror M1 with the small tilting in BS to obtain the two outputs. (b) Channel 2 beam path: the arm including of only static mirror M2 with additional small tilting M2 to obtain the two outputs closed to the beam path in channel 1.

The beam paths that reach each surface of BS and mirror contained the corresponding coefficients, including reflection and transmission, as presented in Table 3.1. These concepts are related to the description in Section 2.2.2. In this system, the balanced output and unbalanced output were represented by the first output and the

second output, respectively. The developed FTS system by using two plane mirrors to obtain two outputs is illustrated in schematic of Figure 3.6.

Table 3.1   The representative coefficients of the reflected beam path and the transmitted beam paths obtained from the two outputs.

	Channel 1 path (static mirror M1)			Channel 2 path (dynamic mirror M2)		
	1st	2nd	3rd	1st	2nd	3rd
1st output	R_{bs}	R_M	T_{bs}	T_{bs}	R_M	R_{bs}
2nd output	R_{bs}	R_M	R_{bs}	T_{bs}	R_M	T_{bs}
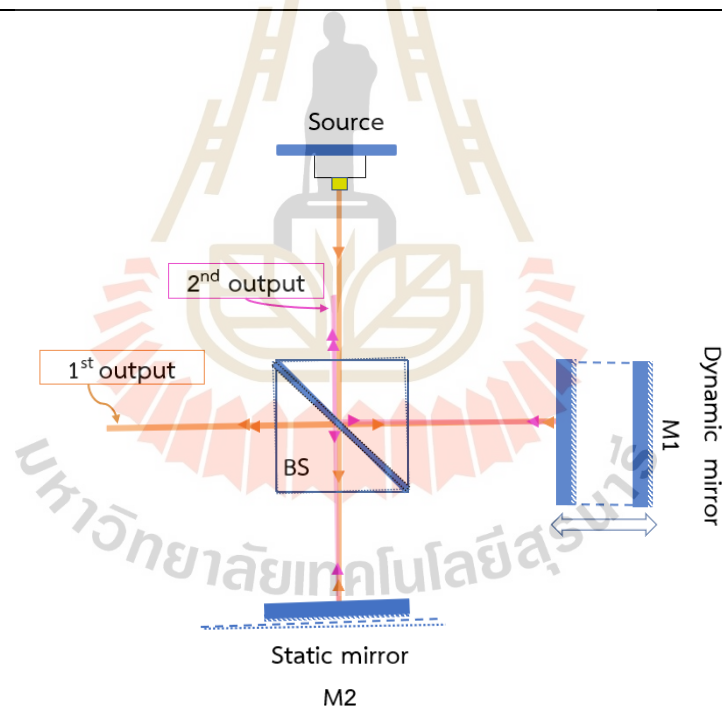
Figure 3.6   The concept design of two outputs interferometer by using the two plane mirrors.

The step of FTS system operation is shown in the flow chart in Figure 3.7. The metrology signal and scientific signal are simultaneously acquired. The interference of metrology signal, which is a monochromatic source, is in the form of cosine variation. Notice that distance between the two consecutive peak and valley is relative to the

distance of half of wavelength of the metrology light source. This relation can be used to correct the non-linear scan and obtain the uniform resampling interferogram (The description of resampling step will be more explicit in the Section 3.5). The spectrum will be obtained after taking the Fourier transform to the resampling interferogram.
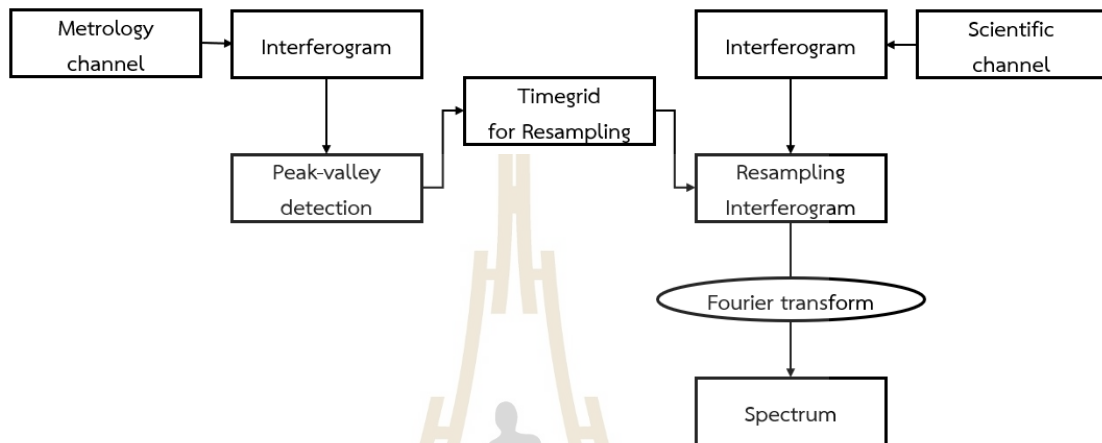
Figure 3.7　　The flow chart describes the process to obtain the spectrum from the acquired interferogram signals in the FTS system.

3.3 Data acquisition

In the FTS system, the measured intensity output of interference signal from interferometer has been digitized by the analog-to-digital converter (ADC). the signals from scientific and metrology channels were simultaneously acquired by using the a 16-bits oscilloscope Analog Discovery 2 (Digilent Inc., USA).

The two simultaneously recorded signals were acquired sampling rate of 50 kHz at a translating stage speed equal to 1.8 mm/s. This parameter provides the metrology interference comprising of approximatively 10 points per fringe. The two synchronous results, including of scientific interferogram and metrology interferogram, are illustrated in Figure 3.8(a) and (b), respectively. The sampling frequency of interferogram signals are sufficient to overcome an aliasing problem that was explained in the Section 2.3. The sampling time interval in both the scientific and the metrology is equal to 20 microseconds that corresponds to an OPD equal to 36 nanometers of metrology.
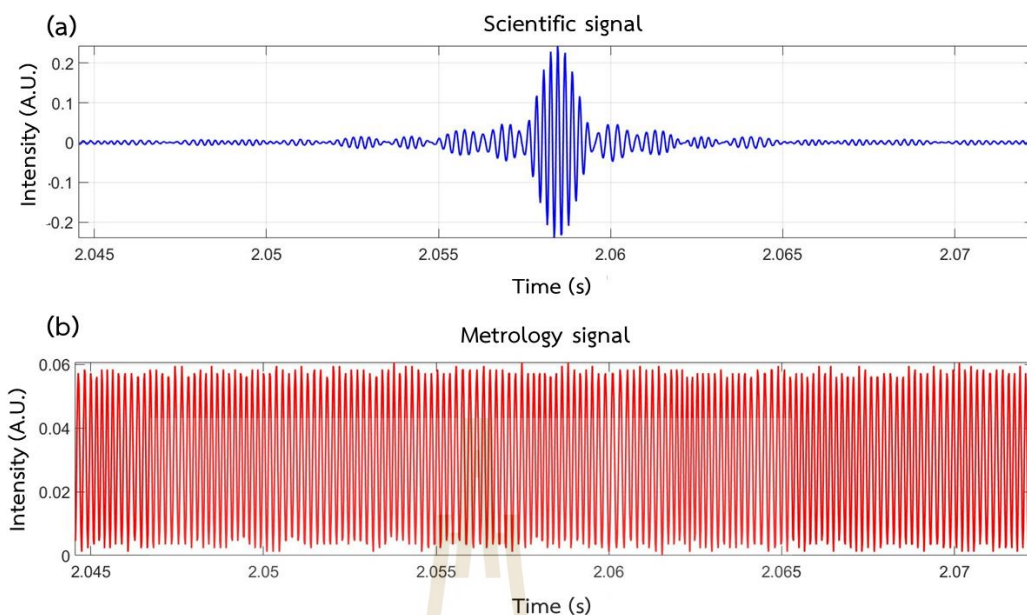
Figure 3.8   An illustration of the simultaneous acquisition of two interference signals from scientific channel (a) and metrology channel (b).

3.4 Investigation of contrast loss

This Section describes the investigation of contrast loss by calculation of fringe contrast with the two possible origins of contrast loss have been introduced in the Section 2.6. The effects under the realistic considerations in our FTS system will be investigated.

3.4.1 Effect of spatial extension of the fiber core

To investigate the effect of core extension to the fringe contrast, the source is assumed to be made up of a large number of point sources, which are mutually incoherent (Born and Wolf, 1999). The fiber output face is represented as spatially incoherent made of a disk uniformly illuminated of diameter defined as $\emptyset_c$.

Let consider one point M located off-axis at the distance y from the optical axis in the object focal plane of the collimator of focal equal to f_{colli}, as shown in Figure 3.9. Each point M reaches the interferometer with an angle of incident defined as θ.
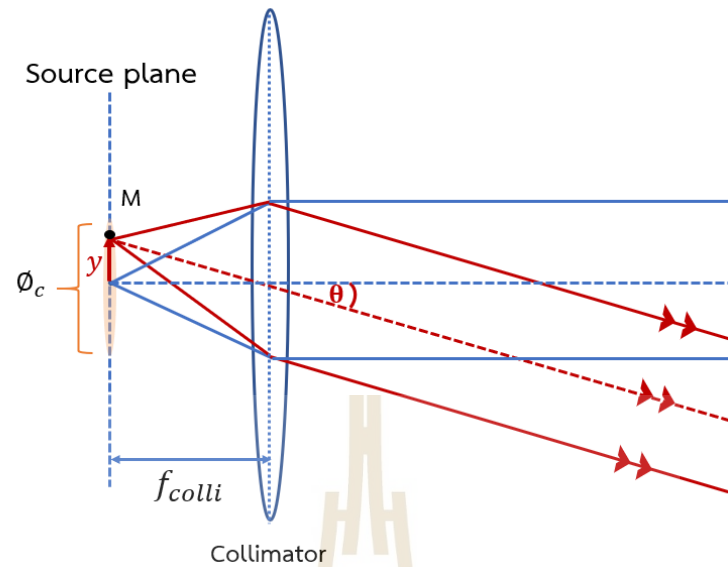
Figure 3.9 A schematic of ray propagating from the point *M* located inside the multi-mode fiber which making an angle of incident to the optical axis.

The angle θ between the beam emitted by M and transmitted by the collimator can be expressed as

$$\theta_M = \tan^{-1}\left(\frac{y_M}{f_{colli}}\right). \tag{3.6}$$

The size of y is limited by the radius of fiber core as $y \leq \frac{\emptyset_c}{2}$. The size is very small compared to the focal length ($f_{colli} \gg y$), implying that the angle θ is typically smaller than 10 degree. Therefore, the small angle approximation (J. Hecht, 2019) can be applied to Equation (3.6) as

$$\theta_M \approx \frac{y_M}{f_{colli}}. \tag{3.7}$$

Let's assume that the source is set a direct orthonormal referential (O, X, Y) with the origin O located at the object focus of the collimator colinear with the optical axis and oriented in the direction of light propagation.
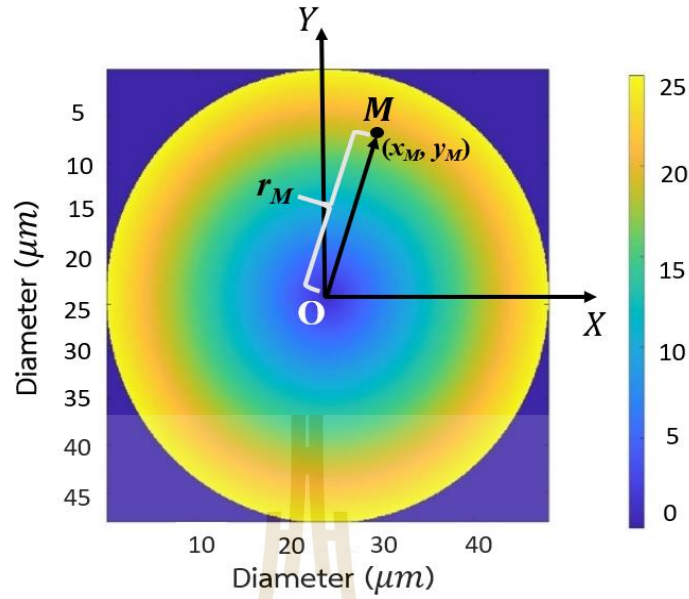
Figure 3.10 An illustration of disk profile of the fiber that varied by the distance from the center.

The expression of the intensity of the beam emitted by M that incidents on the detector is

$$I_M(\sigma_0, OPD'_M) = S(\sigma_0)\cos(2\pi\sigma_0 OPD'_M), \qquad (3.10)$$

where $OPD'_M = OPD_M \cdot \cos\theta_M$ that was calculated from the Equation (2.20).

As illustrated in Figure 3.10, the disk profile of the fiber is expressed as the variation of its radius distanced from the center to the its maximum radius size of fiber core equal to 25 microns. Let's define the radius of point M by setting the radius from the center defined as

$$r_M = \sqrt{x_M{}^2 + y_M{}^2}. \qquad (3.8)$$

As in the small angle approximation in Equation (3.7), the term $\cos\theta$ can be interpreted as $\cos\left(\dfrac{r_M}{f_{col}}\right)$. the expression of OPD'_M is written as

$$OPD'_M(OPD_M, r_M) = OPD_M \cdot \cos\left(\frac{r_M}{f_{col}}\right). \qquad (3.11)$$

The measured intensity at any point in the wave-field s then the sum of the intensities from the individual point sources (Born and Wolf, 1999), which are provided

by each point M inside the fiber. The expression of the theoretical detected intensity at the constant OPD is considered when the beam disk profile composed of N individual points the theoretical detected intensity can be expressed in the summation form as

$$I_{detector}(OPD_M) = \sum_{M=1}^{N} I_M(OPD'_M(OPD_M, r_M)).$$
(3.12)
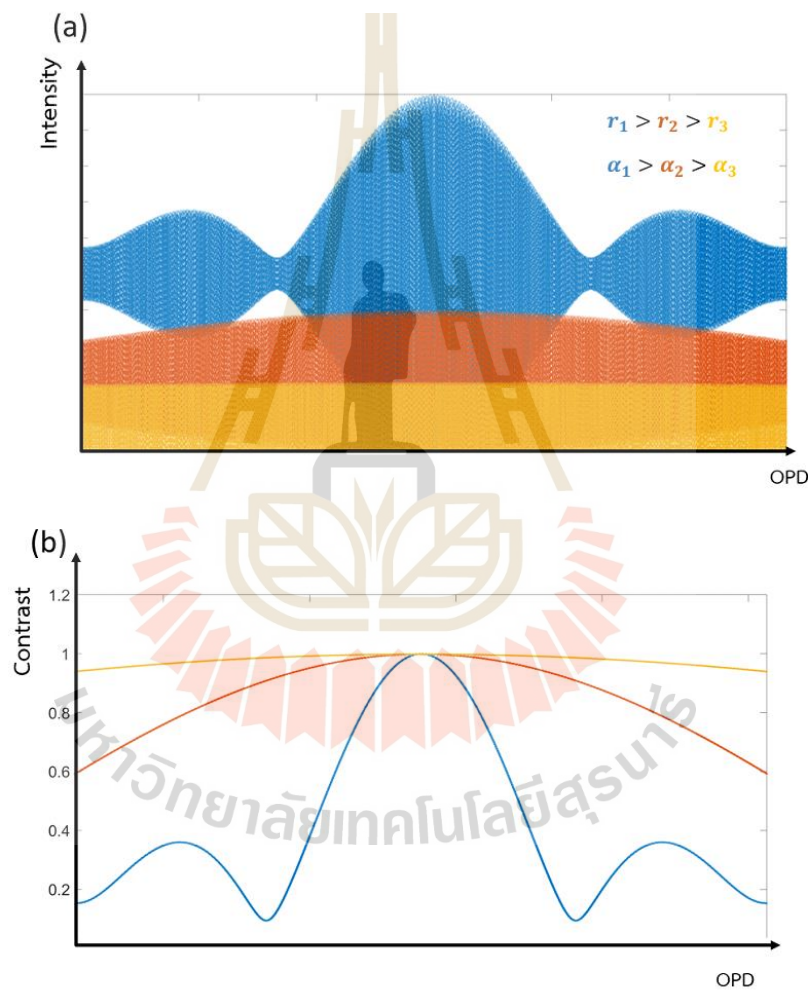
Figure 3.11   (a) The simulation of interferograms that were obtained from the monochromatic source due to the effects of source spatial extension in the fiber core with varying three radii and the effect of the tilt in the dynamic mirror during the displacement with varying three tilt angles and. (b) The fringe contrast variations of (a).

Figure 3.11(a) illustrates the modulated interferograms that were retrieved from the three varying radii of fiber core sizes (r) with same collimator focal length, which corresponds to the contrast varying in Figure 3.11(b). The maximum radius (r_1) is plotted in the blue color. While the smaller radius (r_2) and the minimum radius (r_3) are respectively plotted in the red and yellow color. I thus conclude that the larger size of fiber core leads to the faster contrast loss which agrees with the assumption of spatial extension in the fiber core effect.

3.4.2 Effect of the tilt in the dynamic mirror during the displacement

This effect has been introduced in the Section 2.6.2. As illustrated in Figure 3.12, when the dynamic mirror is moved and thus held at a different angle varied in time than the static mirror relative to the plane of the BS. The two output beams that reflected from both mirrors thus hit the detector plane in the different positions.
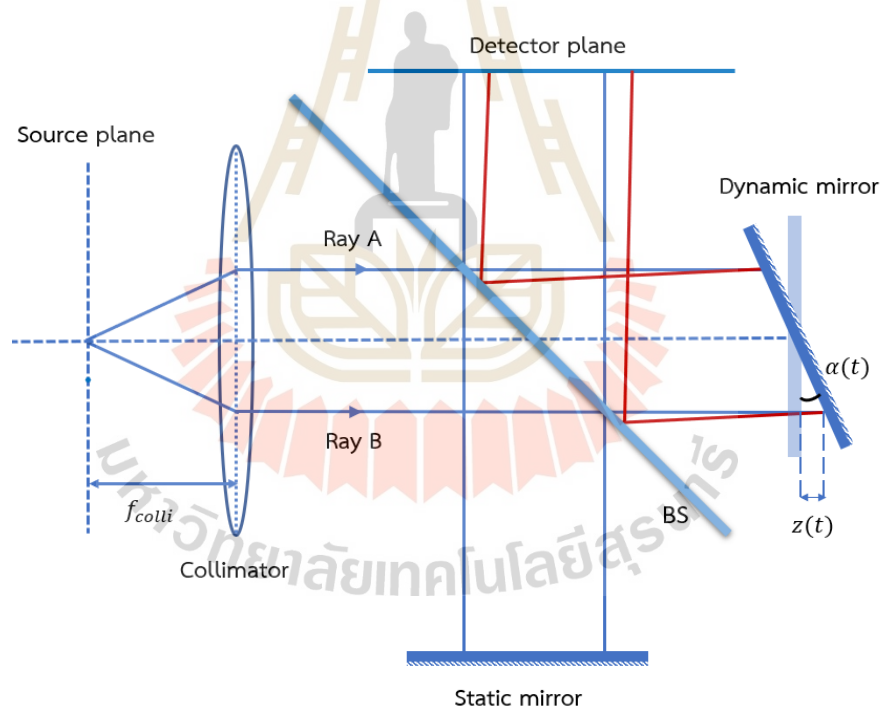
Figure 3.12 A schematic of Michelson interferometer with the effect of tilt in the dynamic mirror along the translation with angle increased with respect to time.

To investigate this effect, the size of the beam that entered to the system is demonstrated. As illustrated in Figure 3.13(a), the beam is injected from the fiber with

Numerical Aperture (NA) defined as $NA = sin\,\emptyset$, where $\emptyset$ determines the maximal half cone angle of light that can enter or exit the lens (Born and Wolf, 1999) through the collimator. The collimator is positioned at f_{colli}, which provides the collimated beam diameter d_{colli} before propagating through the interferometer.

The expression for the diameter size of the collimated beam is written as

$$d_{colli} = 2f_{colli} \cdot tan\,\emptyset \tag{3.13}$$
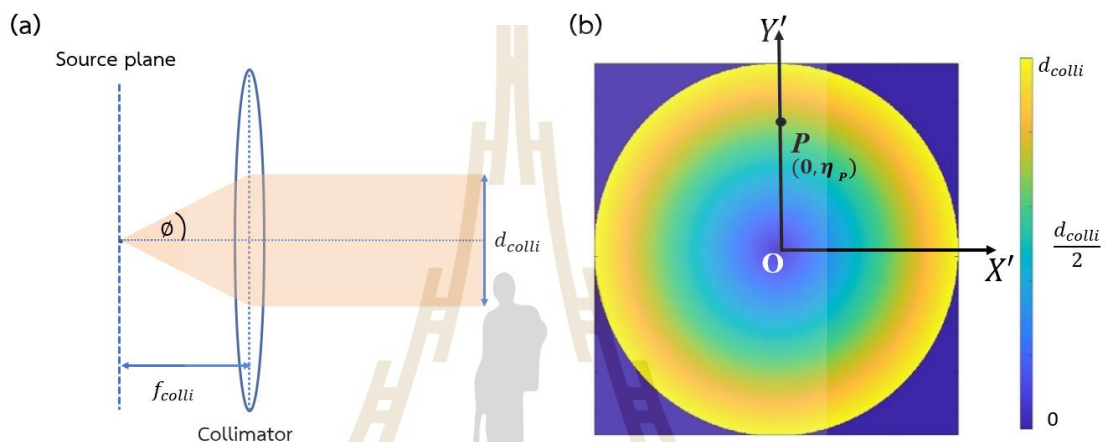
Figure 3.13 (a) A schematic of the collimated beam that propagated through the FTS system. (b) An illustration of disk profile of the collimated beam at the pupil plane, which has the varied color by the distance from the center.

In the Michelson interferometer, the relative alignment between dynamic mirror M1 and the static mirror M2 is directly related to the spectra quality of the system. The unmaintained acuracy path during the translation in dynamic mirror through the interferometer system will be discussed in this Section.

In the FTS system, the dynamic mirror M1 is mounted on a commercial translating stage with a pitch and roll that induce a tilt during M1 translation. The coordinate orthonormal referential (O, X', Y') was set with the origin O located at the centered beam that faced to mirror M1. The disk profile of collimated beam is interpreted as the color variation measured from its centered to its radius size, as illustrated in the Figure 3.13(b).

The tilt α of M1 was assumed to be around the horizontal axis X'. The tilt α is linearly increased with respect to the time delay t, as illustrated in Figure 3.14(a).

Notice that if there is no misalignment in mirror M1, it will always position at perfectly perpendicular to the mirror M2 along the translation.
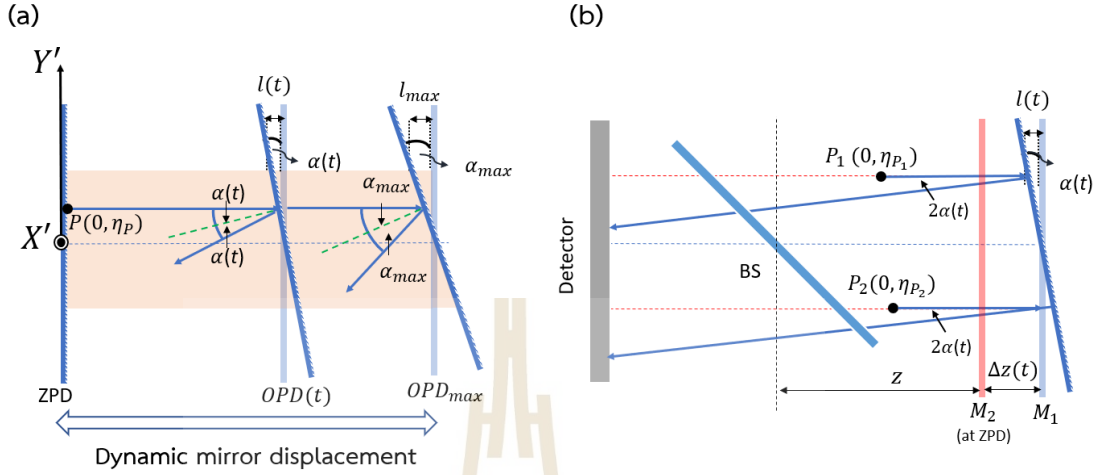
Figure 3.14 A schematic representation of M1 the tilt induced by the translating stage during M1 displacement.

Let's consider the point P located inside the collimated beam at the coordinate $(0, Y')$, the beam incident on the detector by this point can be expressed as

$$I_P (\sigma_0, OPD''_P) = S(\sigma_0) \cos(2\pi\sigma_0 OPD''_P). \tag{3.14}$$

As illustrated in Figure 3.14(b), the static mirror M2 is positioned at distance z from the BS. The beam is reflected with the angle 2α from the dynamic mirror tilt α. The tilt in the mirror induces the shift distance $l(t)$, which is represented as $l_P(\alpha, t)$ at point P. This distance implies the shift in OPD equal to $2l_P(\alpha, t)$.

Consider the at the point $P_1(0, \eta_{P_1})$ located on the positive Y' coordinate in a relative distance η_{P_1}, the expression of OPD at this point is expressed as

$$OPD''_{P_1} = 2\left[\frac{z+\Delta z(t)}{\cos(2\alpha(t))} - z\right] - 2l_{P_1}(t), \tag{3.15}$$

where z is the relative distance from the mirror at ZPD to the detector and $2\Delta z(t) = OPD(t)$.

On the otherhand, at the point $P_2(0, \eta_{P_2})$ located on the negative Y' coordinate in a relative distance η_{P_2}, the expression of OPD at this point is expressed as

$$OPD''_{P_2} = 2\left[\frac{z+\Delta z(t)}{cos(2\alpha(t))} - z\right] + 2l_{P_2}(t). \tag{3.16}$$

Notice that the maximum relative distance ($\eta_{P,max}$) is equal to the half size of collimated beam ($d_{colli}/2$).

The tilt angle is related to the value of pitch and roll in the translating stage, which is in the order of ten microradians. (For example, our translation stage: NEWPORT ESP 301 translating stage has a value of maximum pitch and roll equal to of 37 microradians). The small angle estimation that $cos\alpha \approx 1 - \frac{\alpha^2}{2} \approx 1$ will be applied to the first term of Equation (3.15) and (3.16) as

$$2\left[\frac{z+\Delta z(t)}{cos(2\alpha(t))} - z\right] = 2(z + \Delta z(t) - z) = 2\Delta z(t) = OPD(t). \tag{3.17}$$

Therefore, the expression of the OPD at each point can be written as

$$OPD''_P = OPD(t) \mp 2l_P(t,\alpha), \tag{3.18}$$

where the signs $\mp$ implies the opposite sign of the Y' coordinate as the defined point P.

To verify the shift distance of the point P at the time t, the geometrical relation (Griffiths et al., 2007) can be expressed as

$$l_P(\alpha,t) = \eta_P \cdot tan(\alpha_P(t)). \tag{3.19}$$

The tilt angle is related to value of pitch and roll in the translating stage, which is in the order of ten microradians. (For example, our translation stage: NEWPORT ESP 301 translating stage has a value of maximum pitch and roll equal to of 37 microradians). The small angle approximation will be used to simplified Equation (3.19) as

$$l_P(\alpha,t) \cong \eta_P \cdot 2\alpha_P(t). \tag{3.20}$$

Following the assumption that the tilt α is linearly increased with respect to the time delay t from $\alpha = 0$ at the ZPD to $\alpha = \alpha_{max}$ at OPD_{max}. Therefore, this OPD shift is also varied with respect to this variation from $l(\alpha) = 0$ at ZPD to the maximum $l_{P,max}$ at OPD_{max}. The relative expression between the OPD shift and the OPD is thus written in the ratio as

$$\frac{l(\alpha,t)}{l_{,max}} = \frac{OPD(t)}{OPD_{max}}. \tag{3.21}$$

Therefore, the OPD shift at the specified time t which corresponds to the defined point P is expressed as

$$l_P(\alpha, t) = \frac{OPD(t)}{OPD_{max}} \cdot l_{P,max}. \tag{3.22}$$

By using the geometrical relation, the maximum OPD shift is obtained maximum tilt (α_{max}) can be written in the form as

$$l_{P,max} = \eta_P \cdot \alpha_{max}. \tag{3.23}$$

The expression of the OPD shift is obtained by substituting Equation (3.23) into Equation (3.22) as

$$l_P(\alpha, t) = \frac{OPD(t)}{OPD_{max}} \cdot \eta_P \cdot \alpha_{max}. \tag{3.24}$$

Therefore, the total OPD at each point following Equation (3.18) is expressed as

$$OPD''_P = OPD(t)[1 \mp \eta_P \cdot \alpha_{max}]. \tag{3.25}$$

The detected intensity at the point as following Equation (3.14) is derived as

$$I_P(\sigma_0, OPD, \alpha) = S(\sigma_0) \cos(2\pi\sigma_0 OPD(t)[1 \mp \eta_P \cdot \alpha_{max}]). \tag{3.26}$$

The expression of the theoretical detected intensity that composes of K individual points at the constant OPD is the summation of all individual points inside a pupil plane, which can be written as

$$I_{detector}(OPD,t) = \sum_{P=1}^{K} I_P (\sigma_0, OPD, \alpha).$$ (3.27)

Figure 3.11(a) illustrates the modulated interferograms that were retrieved from the three values of tilts, including pitch and roll, in the translating stage (α), which corresponding to the contrast varying in Figure 3.11(b). The maximum tilt angle (α_1) is plotted in the blue color. While the smaller tilt angle (α_2) and the minimum tilt angle (α_3) are respectively plotted in the red and yellow color. Therefore, a larger tilt leads to faster loss in contrast which agrees with the assumption of tilt in the dynamic mirror during the displacement effect.

3.5 Data processing

This Section presents the steps of signal processing that have been developed and implement through the FTS system

3.5.1 Uniform sampling

The spectrum result is obtained from the implementation of a Fourier transformation to the interferogram which is acquired from interferometer. In general, the interferogram of the source of wavelength λ is recorded in a function of OPD and then converted into the spectrum as the reciprocal of wavelength, called as spatial frequency defined as $\sigma = 1/\lambda$. The interferogram sampling requires the uniform OPD interval.

Figure 3.15 illustrates the spectrum result of recorded metrology signal which is a monochromatic source at wavelength 633.178 nm from the FTS system, while the inset plot shows the theoretical source spectrum that was observed from the optical spectrum analyzer. The result was obtained from the instant recorded interferogram at the desired scan speed in dynamic mirror without the correction of non-linear scan. The non-linearity of scan speed along the acquired signal directly affects to the spectrum result, containing of spurious frequencies in a large spectral bandwidth.
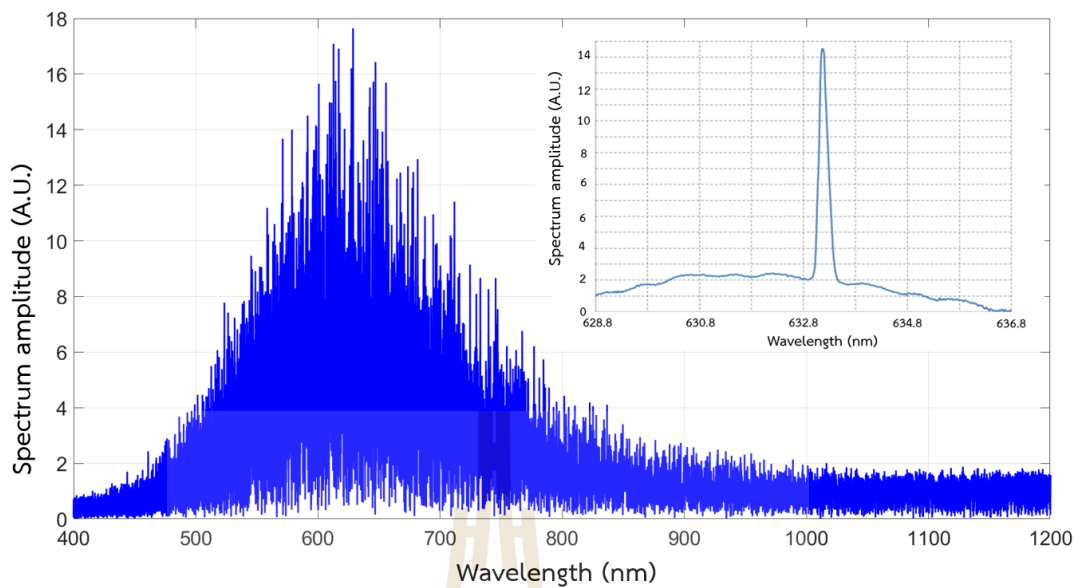
Figure 3.15   The spectrum result of metrology source at wavelength 633.178 nm without the non-linear scan correction and the theoretical spectrum measured by the optical spectrum analyzer (inset).

The data acquisition card records the interferogram in a form of constant time interval. Notice that the interferogram of monochromatic source is modulated in a cosine waveform. The uniform OPD interval can be retrieved from the spatial reference of metrology interferogram. The distance between two maxima as peak-to-peak and two minimum fringes as valley-to-valley from maximum to minimum is equal to the one cycle wavelength of the reference source (λ_{ref}), as illustrate in Figure 3.16. I thus use this relation to evaluate the uniform OPD grid to resampling on the scientific interferogram.
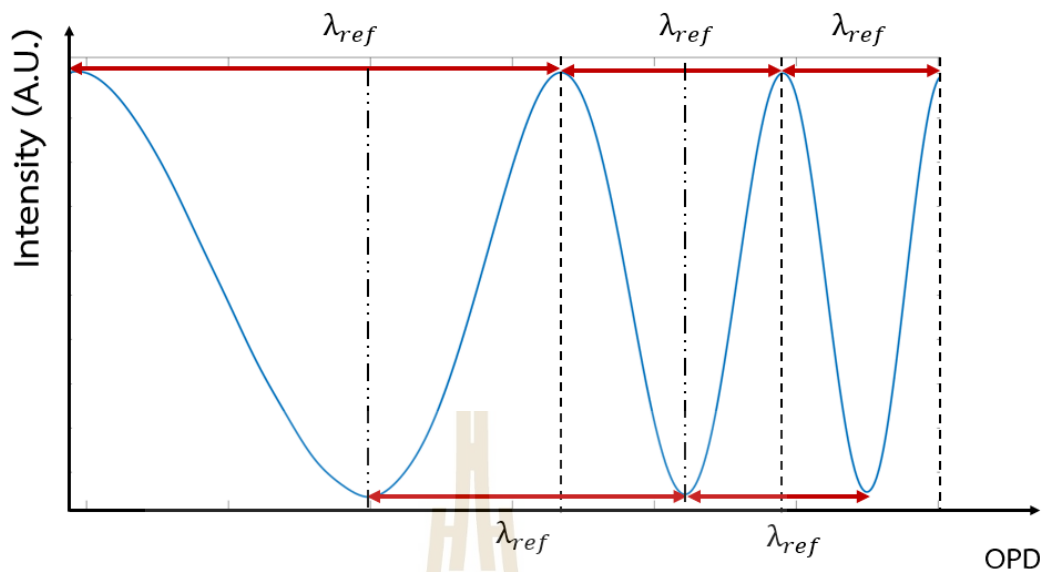
Figure 3.16   An illustration of cosine waveform that represented the interferogram of monochromatic source which is varying under the non-linear scan of the dynamic.

3.5.2 Resampling on interferogram

As described in the Section 3.4, the metrology and scientific interferograms are simultaneously recorded with the same sampling interval at the uniform timestamps. At the sampling rate 50 kHz, the time interval has been recorded at 20 microseconds. The velocity of the dynamic mirror was set at 1.8 mm/s corresponding to OPD interval approximately equal to 72 nm. The processing algorithm that used to extract the spectrum from the raw intensity measurements is implemented on MATLAB 2021a and based on the method, which comprises steps described in the flow chart of Figure 3.17.
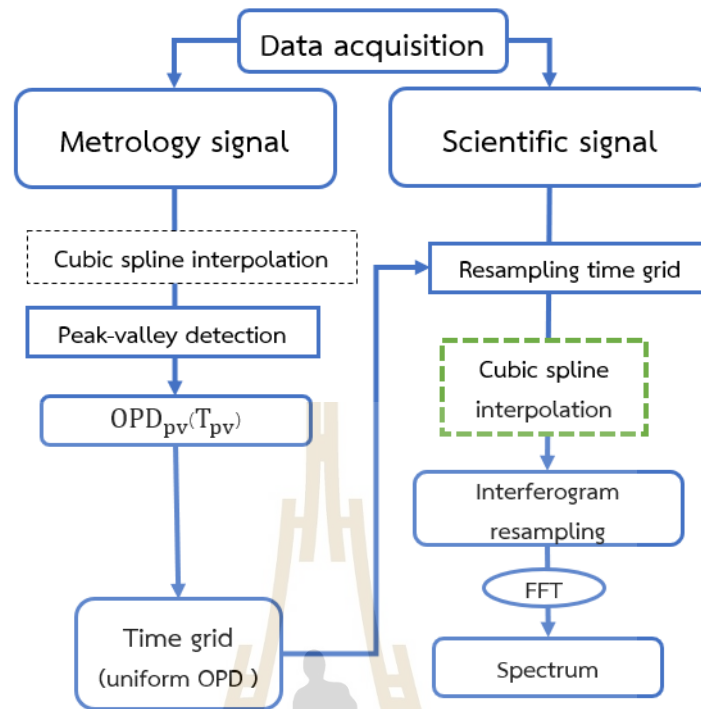
Figure 3.17   The flow chart described the data processing steps by using the Peak-Valley position of metrology signal to resampling the scientific signal before taking the FFT.

First, the scientific and metrology signals were simultaneously recorded as plotted in red rectangular dots in Figure 3.18(a). Second, the locations of the metrology signal peaks and valleys were detected, as illustrated in blue circular dots in Figure 3.18(a). Spline interpolation was applied to the raw signal to improve accuracy of peaks and valleys detection (Aliaga, 2017). The syntax *findpeaks* was used to obtain the position of the metrology signal peaks and valleys from the interpolated signal.

The OPD was defined at a given metrology signal peak measured at the instant time stamp $T_{pv,k}$ called as $OPD_{pv,k}$, where $k = 1, \ldots, N$. The OPD on the preceding signal valley measured at the instant $T_{pv,k-1}$ is called as $OPD_{pv,k-1}$. The variation between OPD of peak-valley's detection and their measured times are plotted in the Figure 3.18(b). Notice that the signal was sampled with a non-uniform OPD interval due to the non-linear scanning of dynamic mirror that was controlled by the translating stage.
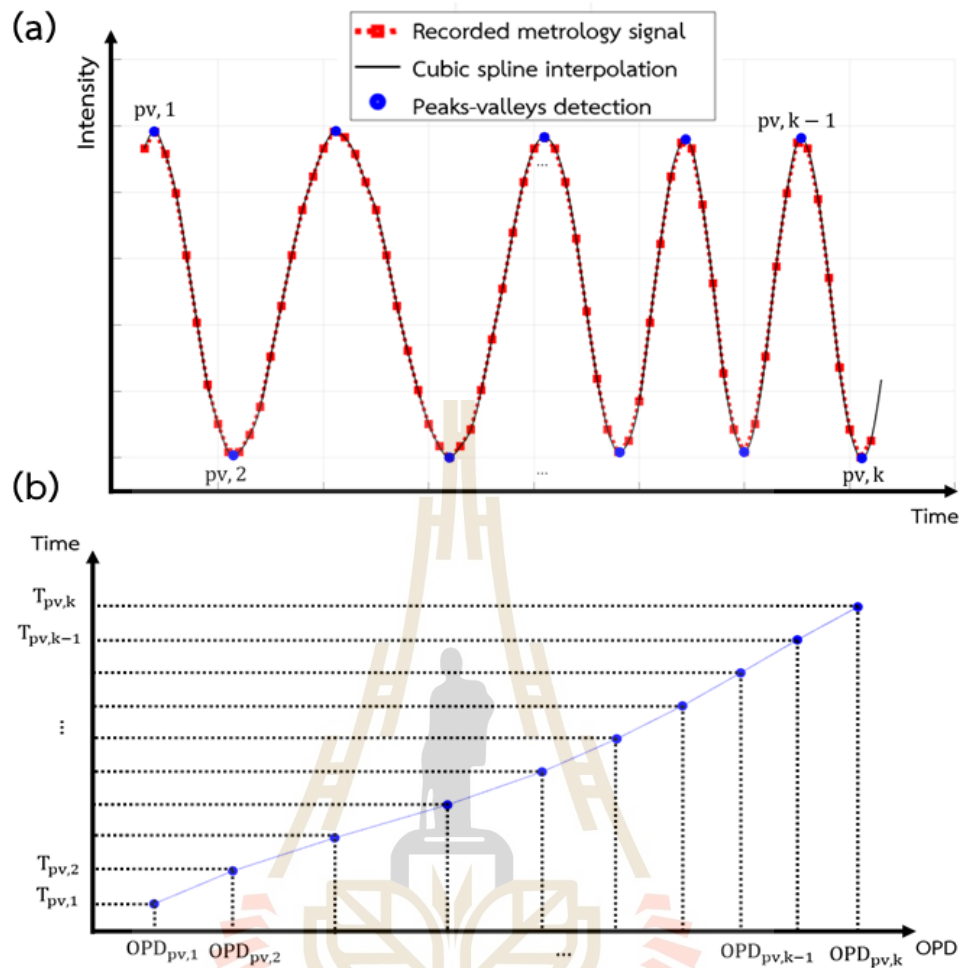
Figure 3.18 (a) An illustration of each peak-valley's detection from the recorded metrology signal. (b) The obtained time grid of at each tracked peak-valley positions with respect to their acquired timestamps of signal (a).

The fact that the time-position relation (Roy et al., 2007) that $OPD_{pv,k} - OPD_{pv,k-1} = 0.5\lambda_{ref}$ was used to calculate the value of the OPD at each time $T_{pv,k}$. The timegrid was obtained in a uniform OPD interval. Finally, the signals from scientific interferogram at each correlated time were extracted, called as "resampled interferogram".

One constraint for the resampling method is the interferogram spacing must follow Nyquist criterion. As described in the Section 2.3, the interval of interferogram is required to be smaller than or equal to $\frac{\lambda_{min}}{2}$. The obtained timegrid from peak-valley detection provides the interval equal to $0.5\lambda_{ref}$, where λ_{ref} is metrology wavelength at 633.178 nm. In order to observe the spectrum that has wavelength response below

λ_{ref}, this interval leads to the problem of aliasing spectrum (Kirchner, 2005) and this resampling method is thus not sufficient.

The result of timegrid in a uniform OPD interval for resampling the scientific signal is varied as the fraction of reference wavelength. The sampling spaced was defined as a fraction of the reference metrology wavelength (Simon A. Roy, 2007). The developed methods for the aliasing correction will be described hereafter.

3.5.3 Correction of aliasing problem: Method I
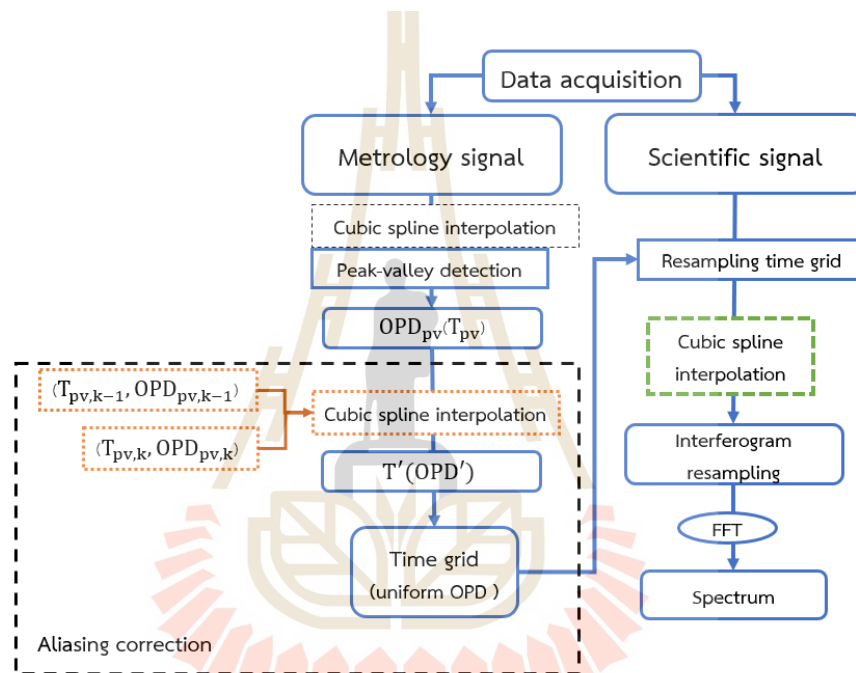
Figure 3.19   A flow chart of resampling steps in method I.

The first method has been developed by implementation the fit of cubic spline interpolation to the time-position variation (Naylor et al., 2004). The steps that described the resampling method I are illustrated in the flow chart in Figure 3.19.

Consider the variation between $(OPD_{pv,k-1}, T_{pv,k-1})$ and $(OPD_{pv,k}, T_{pv,k})$, the outputs of the cubic spline interpolation are two vectors, corresponding to the timestamps and OPD values, as illustrated in Figure 3.20. The timestamp T_i' is retrieved from OPD_i' separation between $OPD_{pv,k-1}$ and $OPD_{pv,k}$ to obtain the new resampling timegrid.
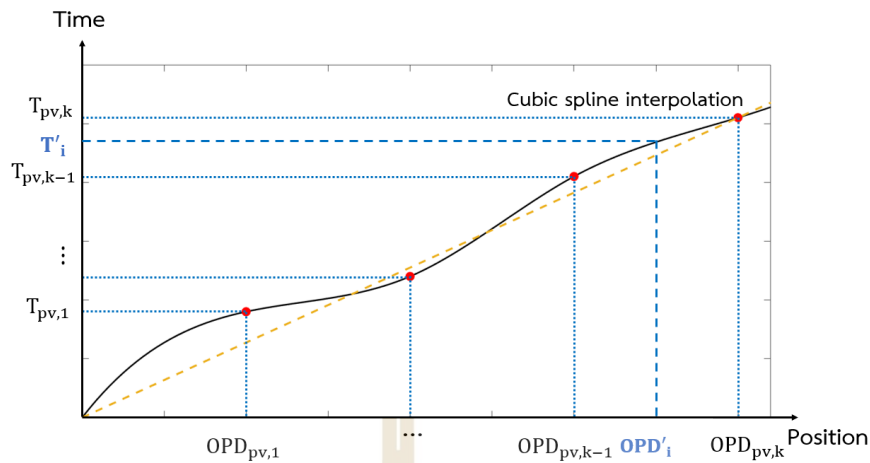
Figure 3.20 An illustration of time-intensity variation that used cubic spline interpolation to determine the resampling timegrid in method I.

3.5.4 Correction of aliasing problem: Method II

The second method the for correction of aliasing has been developed based on the fit of cubic spline interpolation, as shown in the flow chat of Figure 3.21. *CSAPI* syntax in MATLAB Curve fitting toolbox was implemented to each peak-valley pair of metrology signal.
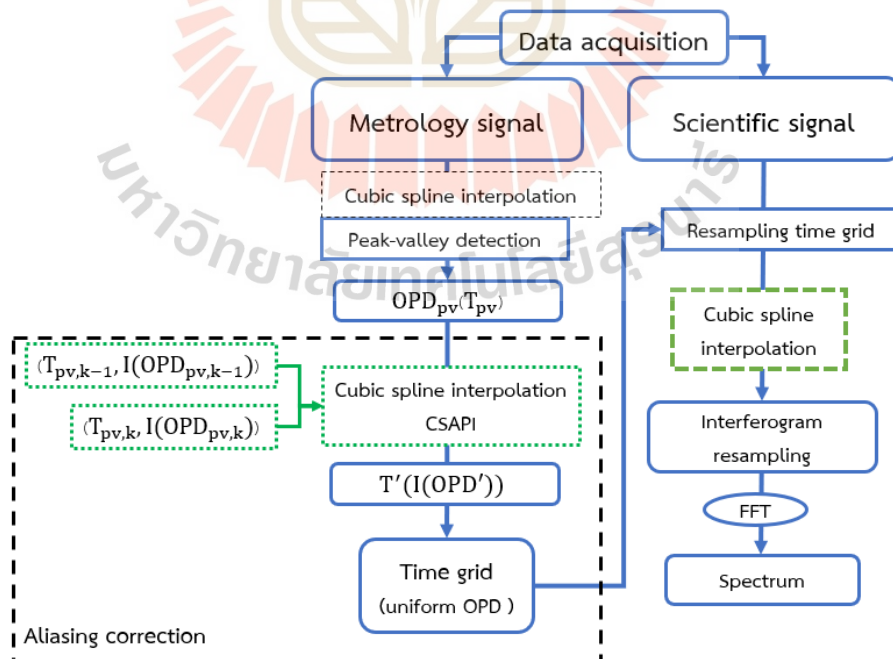
Figure 3.21 A flow chart of resampling steps in method II.

The intensity that was detected at a given metrology signal peak measured at the instant time stamp $T_{pv,k}$ is called as $I(OPD_{pv,k})$ where $k = 1,\dots,N$. The implementation of this method is considered the time-intensity variation between $(I(OPD_{pv,k-1}), T_{pv,k-1})$ and $(I(OPD_{pv,k}), T_{pv,k})$, as illustrated in Figure 3.22. The $I(OPD_{pv,k})$ defines the intensity amplitude that is compromised with the detected position $OPD_{pv,k}$. The term $I(OPD'_i)$ is retrieved from the separation of intensity amplitude between $I(OPD_{pv,k-1})$ and $I(OPD_{pv,k})$. Therefore, the timegrid $T'(I(OPD'_i))$ is obtained, corresponding with the uniform OPD interval equal to $0.25\lambda_{ref}$.
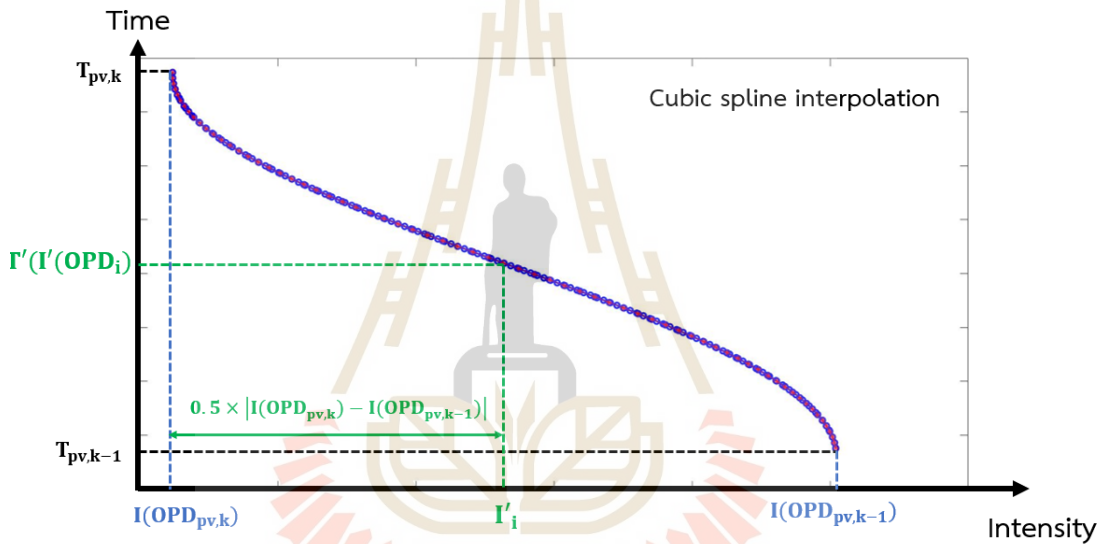
Figure 3.22 An illustration of time-intensity variation that used cubic spline interpolation to determine the resampling timegrid in method II.

3.6 Performance verification by measuring Sun spectrum

In general, a fiber-fed system in an astronomical observation measures the star flux by focusing the beam that is received from the telescope toward fiber entrance. For our measurement, I have applied the telescope defocus technique for collecting the Sun light during an observation. However, the proceeding noises that occur during an observation, for example instrumental or environmental effects, will be the same in both focusing mode and defocusing mode (Hinse et al., 2015).

3.6.1 The experimental setup

The Sun light was collected by using a lens, which represents the telescope. A lens with 1" diameter (AC254-050-B-ML, Thorlabs Inc., USA) was used to defocus the image of the Sun on the fiber entrance. The flux was received through the multimode fiber and connected to the FTS system inside the laboratory. The distance between lens and fiber entrance face was adjusted to reach a flux at the fiber output approximately equal to 1 micro-watt, which is equivalent to the flux of the planets, such as Venus or Jupiter at TNT image plane. The tracking errors with this size of field of view should not compromise obtaining integrated solar disk light in 20 minutes with 40 measurements, as illustrated in Figure 3.23(a).

The lens was held by the compact system called as "Star Adventurer Astronomy" for collecting the Sun light and set with the step as the following:

1) Point the head position to the North pole.
2) Adjust 3 standing posts to reach the tracking inclination equal to 18 degree (see Figure 3.23(b)).
3) Place the lens on the holder as shown in Figure 3.23(b).
4) Rotate the adjusting knob (including rough and fine adjustments) to arrange the position of defocused light through the center of fiber whole (see 3.23(c)).
5) Select the observation mode by rotating the function to "SUN" (see Figure 3.23(d)).
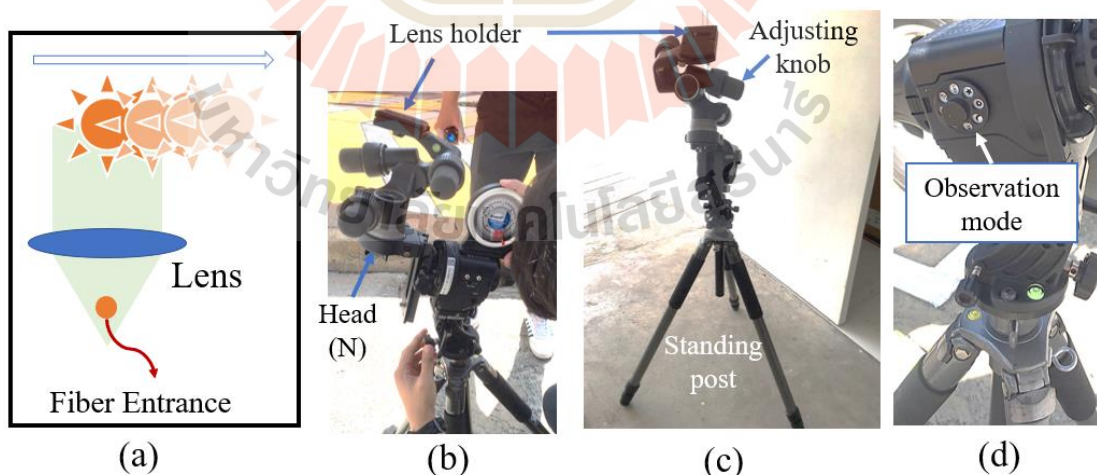
Figure 3.23   (a) Schematic of Sun rotational effect during an observation. The mounting steps of compact Star Adventurer Astronomy to track the Sun rotational path are illustrated in (b), (c), and (d).

3.6.2 The FTS measurement of the Sun

The four steps for making Sun observation by the FTS system will be described as follows

Step 1: Verify the system alignment

A well-aligned FTS system is required before making the measurements. To verify the system, the contrast variation of monochromatic source is required. The metrology source was injected through the scientific fiber and recorded the fringe modulation variation. The result of contrast variation at higher than 0.5 for the operated OPD range between -15 mm, 15mm is satisfied.

Step 2: Set the parameter of acquired data

The two commercial software were applied for the measurement of parameters presented in the table 3.2, including of i) ESP301 for controlling the motion of translating stage. and ii) Waveforms of diligent analog discovery 2 for acquiring the data. The velocity was set to 1.8 mm/s and the sampling rate of acquired data was set to 50 sample/second (as described in Section 3.3). The total scanning range was equal to 15 mm, an integration time was approximately 8.5 seconds for each single measurement.

Table 3.2   The properties of data acquisition in FTS system.

OPD range	-15 mm to +15 mm
Scanning range	-7.5 mm to +7.5 mm
Stage velocity	1.8 mm/s
Sampling rate	50 kHz

Step 3: Make a measurement

The setup was positioned outside the laboratory during an observation, as illustrated in Figure 3.24.
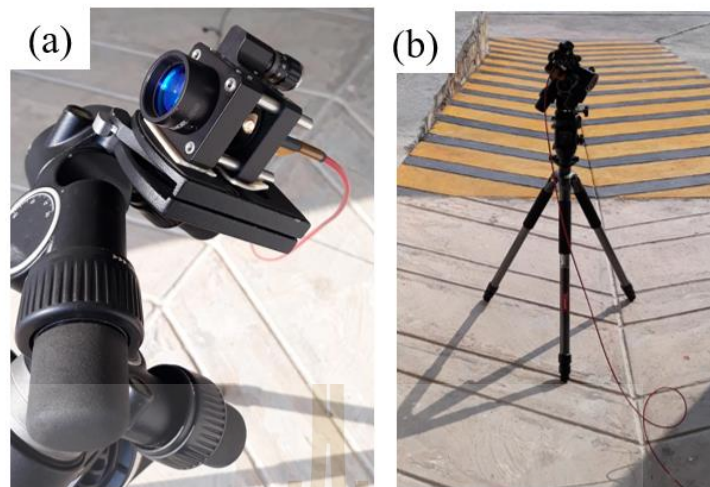
Figure 3.24   (a) An illustration of the setup image of Sun and connected to the fiber to reach the scientific port of FTS system inside the Laboratory in (b).

In each single measurement, the data was acquired and illustrated the preliminary result in the Waveforms software. The two channels were simultaneously recorded with the same timestamps and all parameters listed in Table 3.2. these results were thus exported and performed the post-signal processing by using MATLAB 2020a to obtain the spectrum of the Sun that will be presented and discussed in the next chapter.

CHAPTER IV
RESULTS

4.1 Setup implementation

Our FTS system relies on the dual-configuration Michelson interferometer, including scientific and metrology interferometers. A schematic diagram of the FTS setup is illustrated in Figure 4.1. In scientific system, the multimode fiber with core diameter 50 microns and N.A. equal to 0.22 (FG050LGA, Thorlabs Inc., USA) injects the light source to the collimator L1 (AC127-019-B, Thorlabs Inc., USA). The collimator collimates the beam toward the 50:50 non-polarized beam splitter cube (BS014, Thorlabs Inc., USA). The beam splitter splits the beam into two identical beams, calling as channel 1 and channel 2. In channel 1, the beam is reflected by the beam splitter to the dynamic mirror M1 (PF10-03-M01, Thorlabs Inc., USA). This mirror is mounted on a linear translating stage (M-ILS200CCL, Newport Inc., USA) and is controlled by a motion controller (ESP 301, Newport Inc., USA) during the data acquisition. At the same time, the beam in channel 2 is transmitted through the BS to reach the static mirror M2 (PF10-03-M01, Thorlabs Inc., USA).
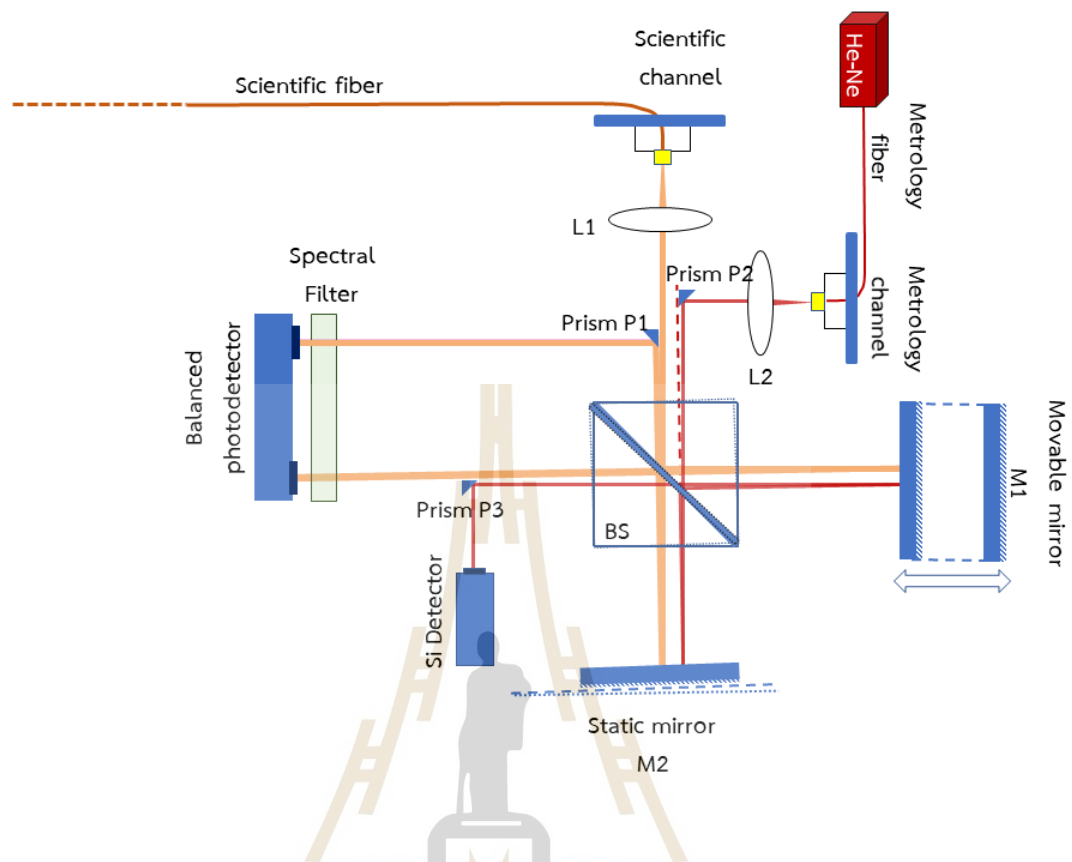
Figure 4.1   Schematic illustrated the optical components in the FTS system. The tracing in orange color illustrates scientific beam path that is entered to the system by a fiber with a core diameter of 50 microns. The metrology source is injected to the system via the single-mode fiber, as represented in the red color. The beam splitter and static mirror are slightly tilted in order to obtain and direct the two output beams toward the two ports of a balanced photodetector.

A small tilting in the beam splitter and in the static mirror M2 is applied. Hence, the beam splitter combines the two reflected beams of channel 1 and 2 and provides two output beams. The first output beam is incident on the spectral filter (I-band region, Astrodon Photometrics) and directed to the first port of balanced photodetector (2307, Newport Inc., USA). The second output beam is incident on the reflecting prism P1 (PS908H-B, Thorlabs Inc., USA) that directs the beam toward the second entrance of the balanced photodetector after passing through the spectral filter. The spectral filter is located in front of the balanced photodetector in order to reduce the photon noise by restricting the spectral extension of the beam incident on

the detector and suppressing the metrology leakage signal that is induced by the scattering, diffraction, and spurious reflections along the measurement.

The metrology port is included in the FTS system to correct the non-linearities of the dynamic mirror. It has been applied as the reference source to monitor the displacement of the dynamic mirror during the data acquisition. The metrology source is made of a stabilized laser (SLM_52371_2-258, Edmund Optics Inc., USA) at the reference wavelength equal to 633.178 nm. The single mode fiber (FT030-Y, Thorlabs Inc., USA) injects the metrology source to the collimator L2 (AC254-050-A-ML, Thorlabs Inc., USA). The beam is collimated and directed toward the prism P2 (PS908H-B, Thorlabs Inc., USA). The prism P2 reflects the collimated beam into a similar direction of the scientific beam that incident on the FTS. The optical path of the metrology beam through the interferometer is thus similar to the science beam's optical path. The prism P3 (PS908H-B, Thorlabs Inc., USA) is placed to reflect the one output toward the Si detector (2032, Newport Inc., USA).
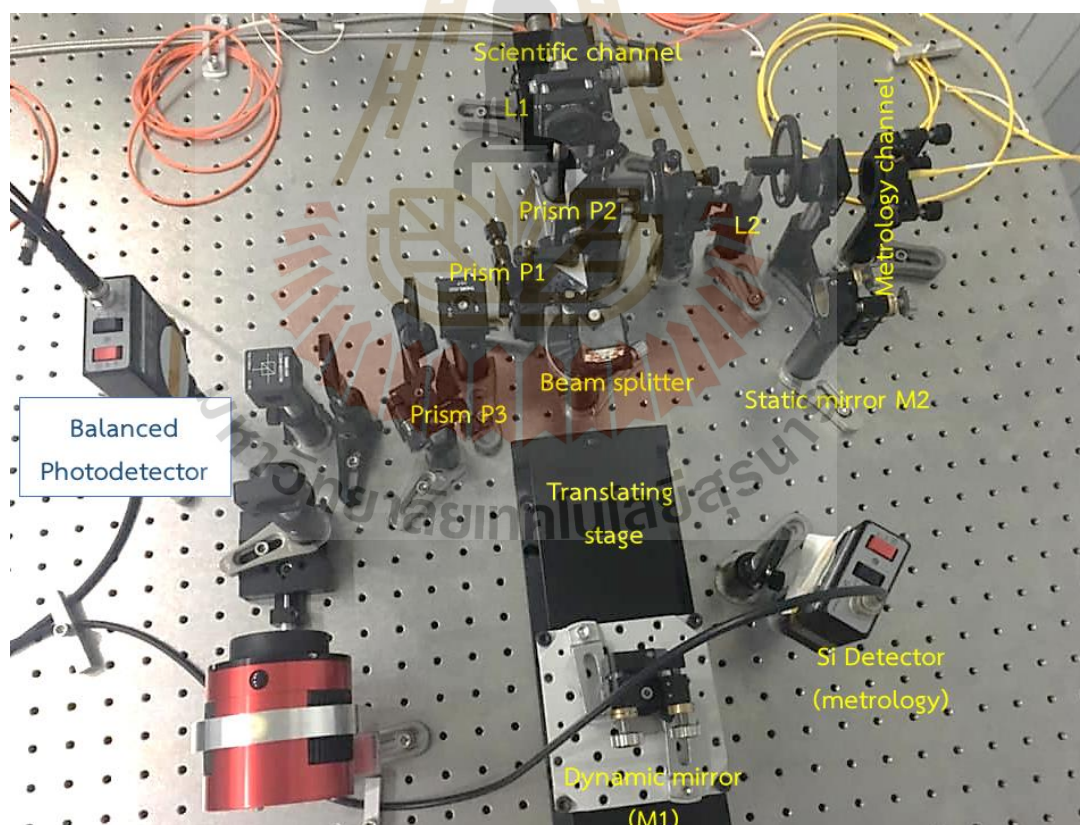
Figure 4.2   A photograph of the FTS setup on an optical bench that has been developed in Laboratory of Optics for Space and Astronomy at NARIT, Chiang Mai, Thailand.

The image of the FTS setup developed at National Astronomical Research Institute of Thailand (NARIT) is shown in Figure 4.2.

4.2 Performance of the system

4.2.1 Instrument throughput

The throughput of the FTS system is determined by the multiplication of each optical transmission along the beam path of the system. This throughput was considered starting after the beam was injected from the fiber. As described in the precious Section, the first element that the beam has passed was the collimated lens $L1$. Then, the beam reaches the BS and was spitted to the two mirrors and reflected back to the BS. Notice that the beam was passed through a spectral filter before reaching the balanced detector. The calculation of FTS throughput is expressed as

$$T_{FTS} = T_{L1} \times [T_{output1} + T_{output2}] \times T_{SF}, \tag{4.1}$$

where T_{L1} is the transmission of the lens $L1$. T_{SF} is the transmission of the spectral filter. $T_{output1}$ and $T_{output2}$ are the total transmission of beam path at the first and second port of the balance detector, respectively.

A reflection coefficient the prism that folds the beam is assumed to be equal to 1. The throughput transmission of beam path through the 1st output is interpreted as

$$T_{output1} = R_{BS} \times R_{M1} \times T_{BS} + T_{BS} \times R_{M2} \times R_{BS}, \tag{4.2}$$

where R_{M1} and R_{M2} represent the reflectivity of the mirrors M1 and M2, respectively. R_{BS} and T_{BS} are the BS's reflection and transmission, respectively.

The throughput transmission of beam path through the 2nd output can be interpreted as

$$T_{output2} = R_{BS} \times R_{M1} \times R_{BS} + T_{BS} \times R_{M2} \times T_{BS}. \tag{4.3}$$

The reflectivity of two mirrors are assumed to be identical as $R_{M1} = R_{M2} = R_M$. By substitute Equation (4.2) and (43) into Equation (4.1),

$$T_{FTS} = T_{L1} \times T_{SF} \times R_M \times (2 \times R_{BS} \times T_{BS} + R_{BS}^2 + T_{BS}^2). \tag{4.4}$$

Therefore, the simplified form is given as

$$T_{FTS} = T_{L1} \times T_{SF} \times R_M \times (R_{BS} + T_{BS})^2. \qquad (4.5)$$

The theoretical throughput transmission in each optical component in the FTS system are separately illustrated in the dash-line with different color in Figure 4.3. The total throughput transmission of the FTS calculated from Equation (4.5) when equipped with an I-band photometric filter of central wavelength equal to 800 nm and FWHM equal to 160 nm is presented in the black solid line. Notice that the theoretical throughput reaches 80% in the wavelength region 760-840 nm.
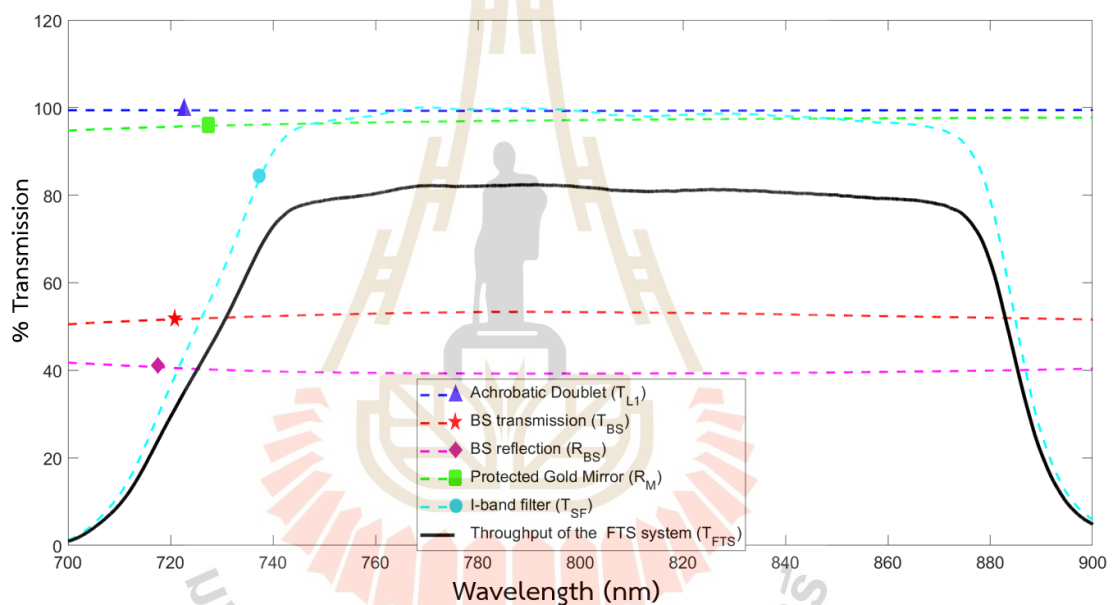
Figure 4.3   An illustration of theoretical throughput variation over the wavelength 700-900 nm. The theoretical transmission of each individual component in the FTS system are separately plotted in dash lines (Blue with rectangular mark: T_{L1}. Red with star mark: T_{BS}. Magenta with diamond mark: R_{BS}. Green with rectangular mark: R_M. Cyan with circular mark: T_{SF}.) and the total transmission throughput of FTS system (T_{FTS}) is plotted in the black-solid line.

4.2.2 Contrast variation

To verify the FTS system, the fringe contrast variation has been considered as a step of system calibration, as described in Section 2.6. Notice that the fringes are

clearly observed when the system is well-aligned. The fringe modulation was measured by injecting the metrology source, which was monochromatic, through the scientific fiber, as illustrated in the schematic of Figure 4.4. The signal was recorded in a single-side interferogram between ZPD and the desired OPD and then implemented to be the full double-side interferogram.
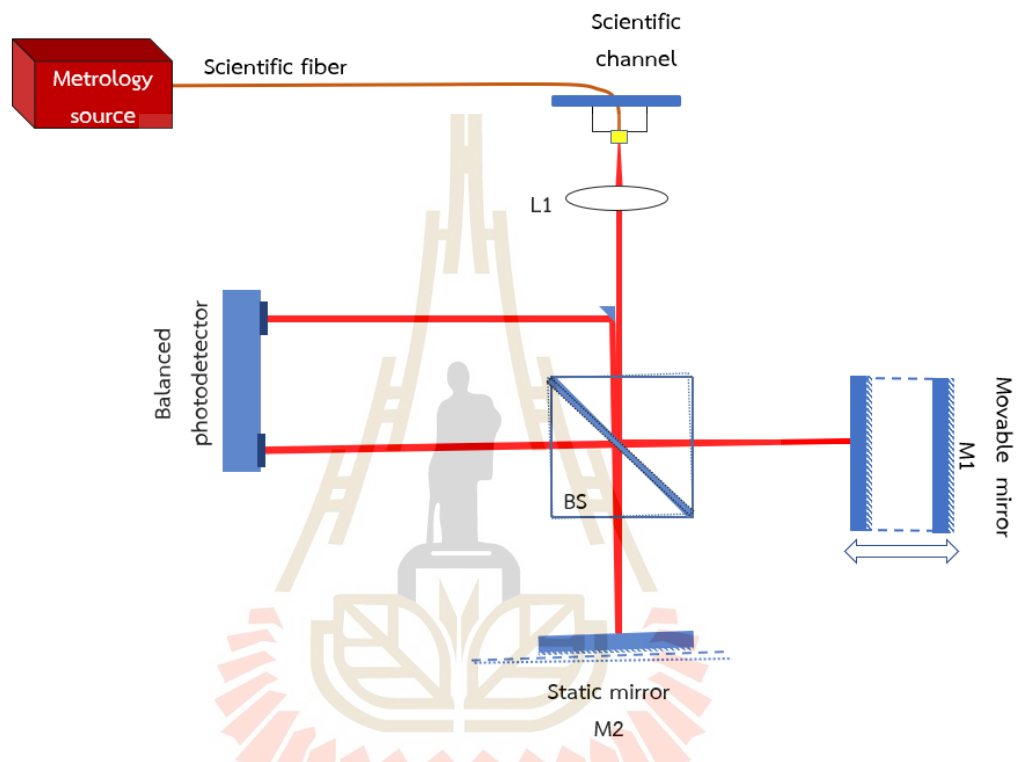
Figure 4.4   Illustrations of the measured intensity of metrology source with removing of spectral filter and mask one output.

The recorded interferogram was retrieved from the scientific channel of the FTS system measured at the $OPD =$ ZPD±65 mm, which provides the contrast variation, as illustrated in Figure 4.5. The variation of fringe modulation shows the maximum intensity at ZPD, which is corresponded to the fringe contrast close to 1.
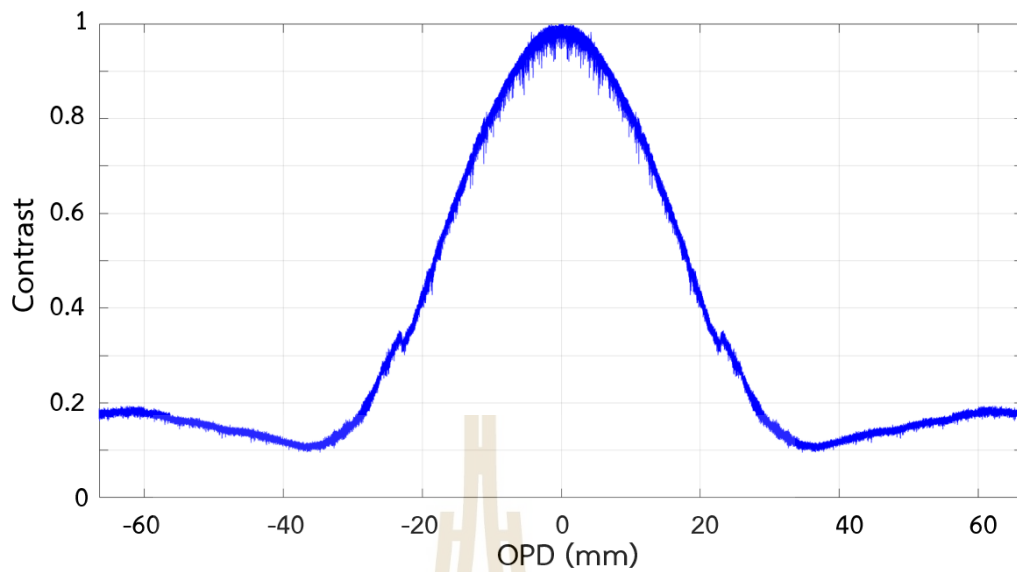
Figure 4.5   The measured contrast of metrology source in the range ZPD±65 mm.

Notice that the fringe modulations are clearly observed at the contrast higher than 0.5 (D. and Milster.), which is correlated to the distance of translation in dynamic mirror at the range ZPD±15 mm, as plotted in Figure 4.6.
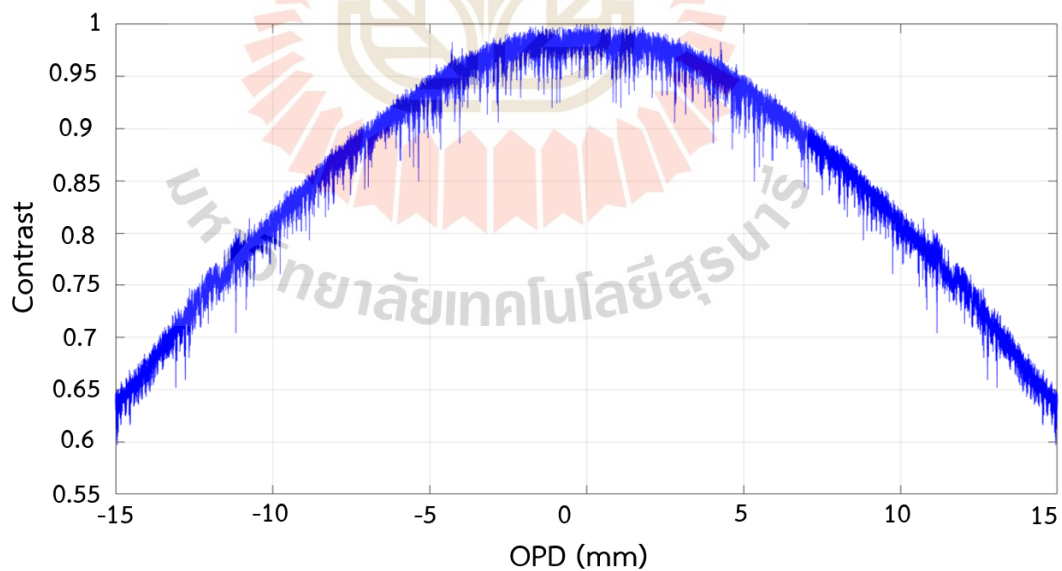
Figure 4.6   The contrast variation of the interferogram result obtained from of metrology source measured in the range 15 mm from ZPD.

In the Sections 3.4.1 and 3.4.2, the two origins that affect the contrast loss, including of the effect of the source's spatial extension and the effect of the mirror misalignment due to the tilt along the translation, have been studied. The results of the two assumptions are as follow.

Effect I: Source's spatial extension

The extended source due to the large fiber core affects the OPD variation and thus leads to the decreasing of contrast that was initial discussed in Section 2.4.1 and 3.4.1. In our FTS, the scientific fiber with core diameter 50 microns has been applied to the system. Therefore, the maximum distances from the fiber core center is equal to the maximum fiber radius $r_{M,max}$ = 25 microns.
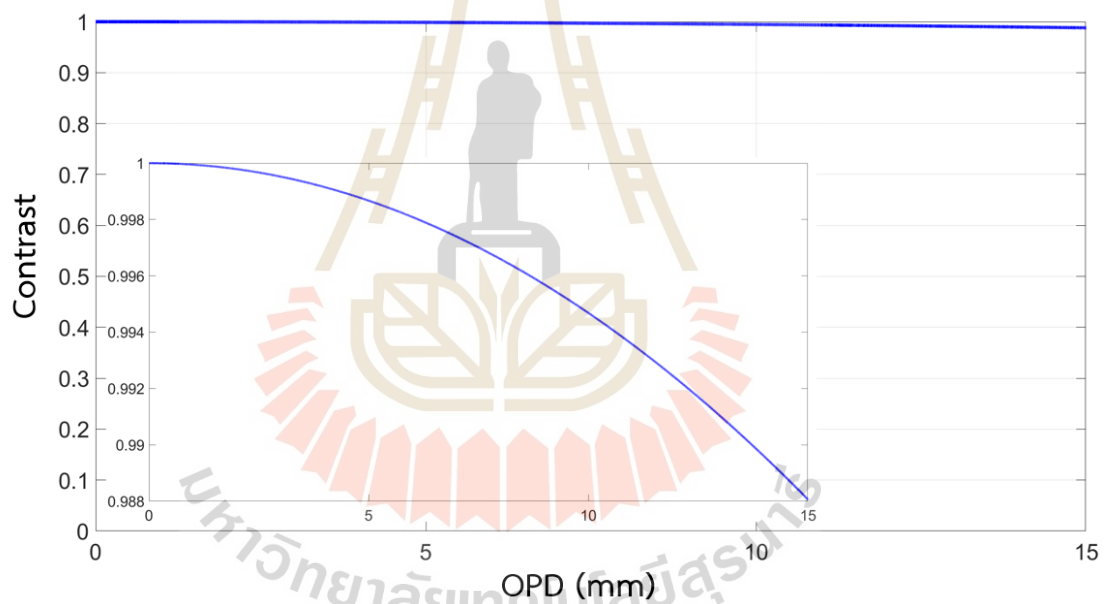
Figure 4.7   The theoretical contrast variation due to the spatial extension of the fiber core. The zoom in is shown in the inset plot.

The theoretical single-side interferogram in the form of intensity variation that has been calculated from the effect of extended source shows the contrast variation. The modulations in fringe pattern provide a very small contrast decrease to be 0.988 at the OPD = 15 mm, as shown in the zoom in plot.

Figure 4.8 shows the disk profiles that represents the image planes measured at the maximum and minimum specified OPD due to the effect of the large fiber core. The four image planes of maximum intensities (I_{max}) that were measured at four position, including of ZPD, OPD = 5 mm, 10 mm, and 15 mm are presented in Figure 4.8(a), while the four image planes of minimum intensities (I_{min}) that measured at ZPD $+ \frac{\lambda}{2}$ mm, $OPD = 5 + \frac{\lambda}{2}$ mm, 10$+\frac{\lambda}{2}$ mm, and 15$+\frac{\lambda}{2}$ mm are presented in Figure 4.8(b).
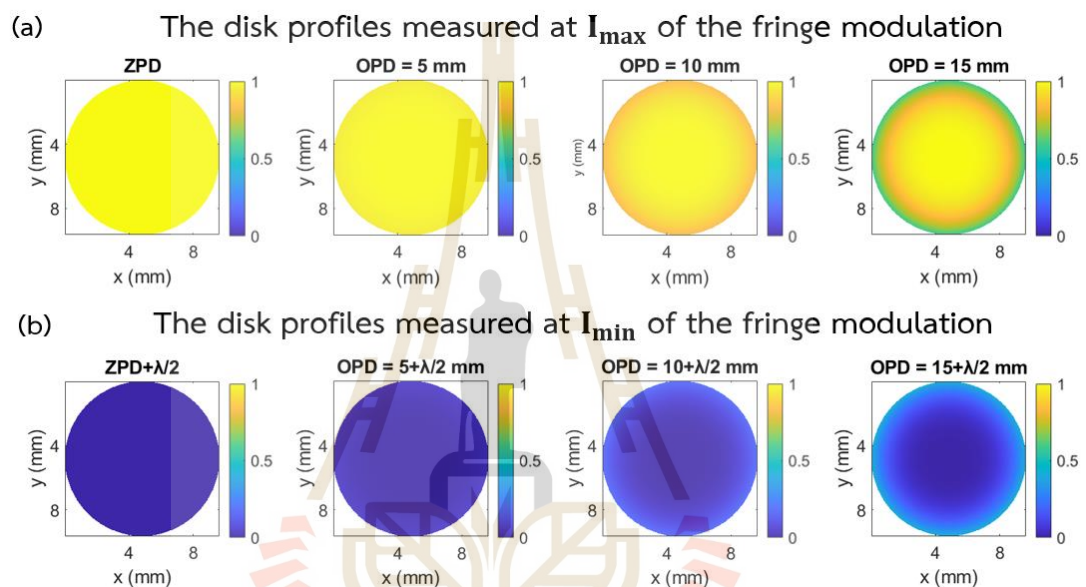
Figure 4.8   The disk profiles distribution of the image planes that was induced by the spatial extension of fiber core and represented as maximum intensity located at ZPD, OPD = 5 mm, 10 mm, and 15 mm and consecutive minimum intensity of (a) that were measured at ZPD + λ/2 mm, OPD = 5+λ/2 mm, 10+λ/2 mm, and 15+λ/2 mm in (b), respectively.

Effect II: Mirror misalign during the translation

The misalignment is induced by the pitch tilt of dynamic mirror M1 along the translation, which has introduced in the Section 2.4.2 and 3.4.2. In this Section, the model of contrast decreasing in realistic FTS measurement due to this effect is presented.

The scientific fiber has NA equal to 0.22. The collimator is placed at the distance of focal length: f_{colli} = 19 mm from the fiber output. The half cone angle is calculated following Equation (3.1) as

$$\emptyset = \sin^{-1}(NA) \approx 12.7°. \tag{4.6}$$

The collomator collimates the diverged beam and provides the diameter size of the collimated beam (d_{colli}), which is defined the maximum size of η_P as

$$d_{colli} = 2 \times f_{colli} \times \tan\emptyset \approx 8.6 \text{ mm} = \eta_{P,max}. \tag{4.7}$$

In Michelson interferometer, the relative alignments between dynamic mirror M1 and the static mirror M2 directly affects the modulation of the interference between two beams. This misalignment could be induced by the unmaintained acuracy path during the translation in dynamic mirror. The dynamic mirror was moved and induced the tilt along the translation.
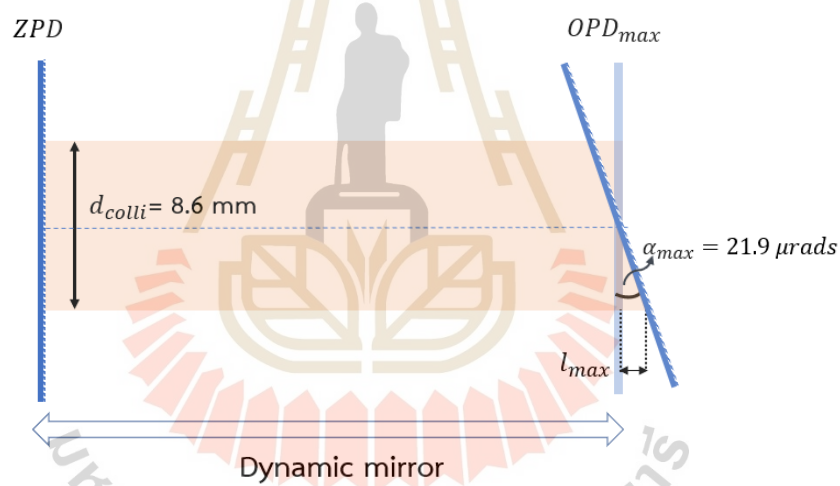
Figure 4.9   The tilt along the translation in dynamic mirror, which is linearly increased from 0 to 21.9 microradians at OPD_{max} = 15 mm.

In this work, the tilt in the dynamic mirror was simulated. The tilt was assumed to be linearly varied from α_0 = 0 microradian at ZPD to α_{max} = 21.9 microradians at the OPD_{max} = 15 mm, as illustrated in Figure 4.9. The theoretical interferogram, which is obtained from the mirror misalignment, was calculated under the following parameters. The result of contrast variation was plotted in Figure 4.10.
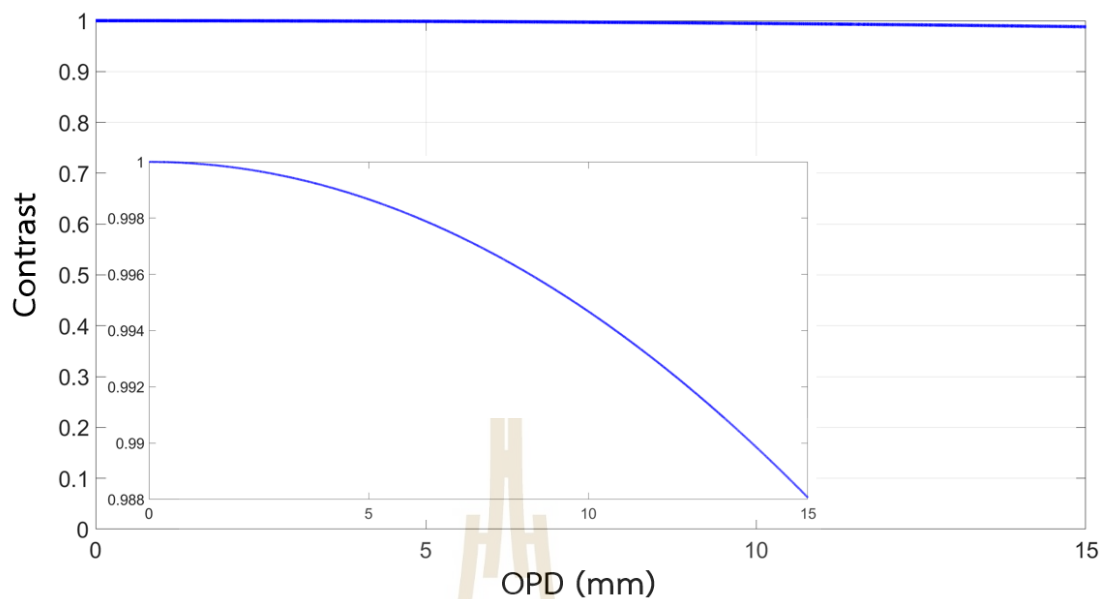
Figure 4.10   The theoretical contrast variation due to the effect of the dynamic mirror tilt along the translation, while the zoom in is shown in the inset plot.

The disk profiles that represents the pupil planes at the specified OPD due to the effect of mirror tilt along the translation are illustrated in Figure 4.11. The four image planes of maximum intensities (I_{max}) that are measured at ZPD, OPD = 5 mm, 10 mm, and 15 mm are presented in Figure 4.11(a). The four image planes of minimum intensities (I_{min}) that are measured at ZPD $+ \frac{\lambda}{2}$ mm, $OPD = 5 + \frac{\lambda}{2}$ mm, $10 + \frac{\lambda}{2}$ mm, and $15 + \frac{\lambda}{2}$ mm are presented in Figure 4.11(b).

(a)   The disk profiles at maximum intensity of the fringe modulation
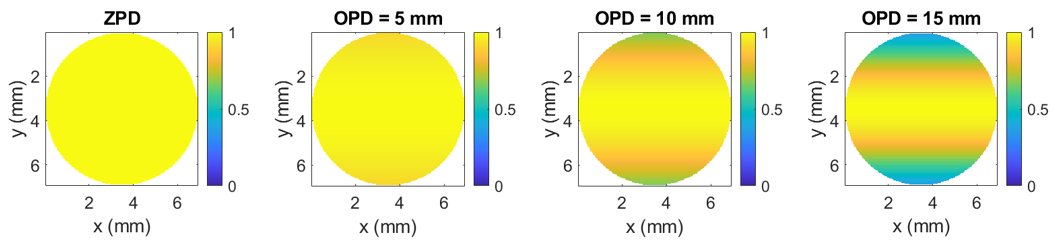
(b)   The disk profiles at minimum intensity of the fringe modulation
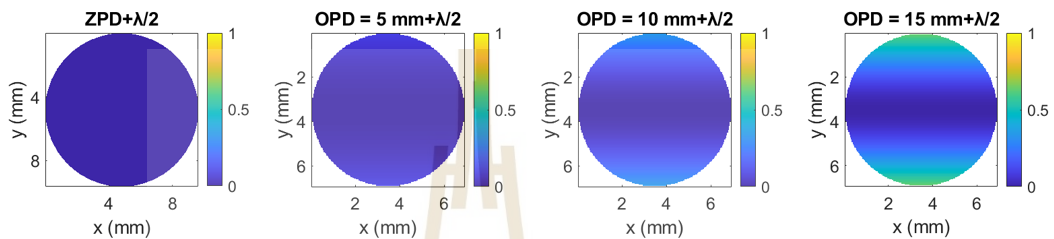
Figure 4.11   (a) The distribution of the pupil planes that was induced by the linear tilt in dynamic mirror along the translation represented as maximum intensity located at ZPD, *OPD* = 5 mm, 10 mm, and 15 mm. Minimum intensity that were measured at ZPD +λ/2 mm, *OPD* =5 +λ/2 mm, 10+λ/2 mm, and 15+λ/2 mm in (b).

Figure 4.12 shows the comparison between the three contrast varying plots. The contrast measured from the FTS setup is illustrated in the blue solid line. The theoretical contrast loss due to the source's spatial extension is plotted in the red dotted line, while the theoretical contrast loss due to the mirror misaligned along the translation is plotted in the yellow-solid line. These plots show that the effect of source's spatial extension is considered negligible for the contrast loss in the FTS system.
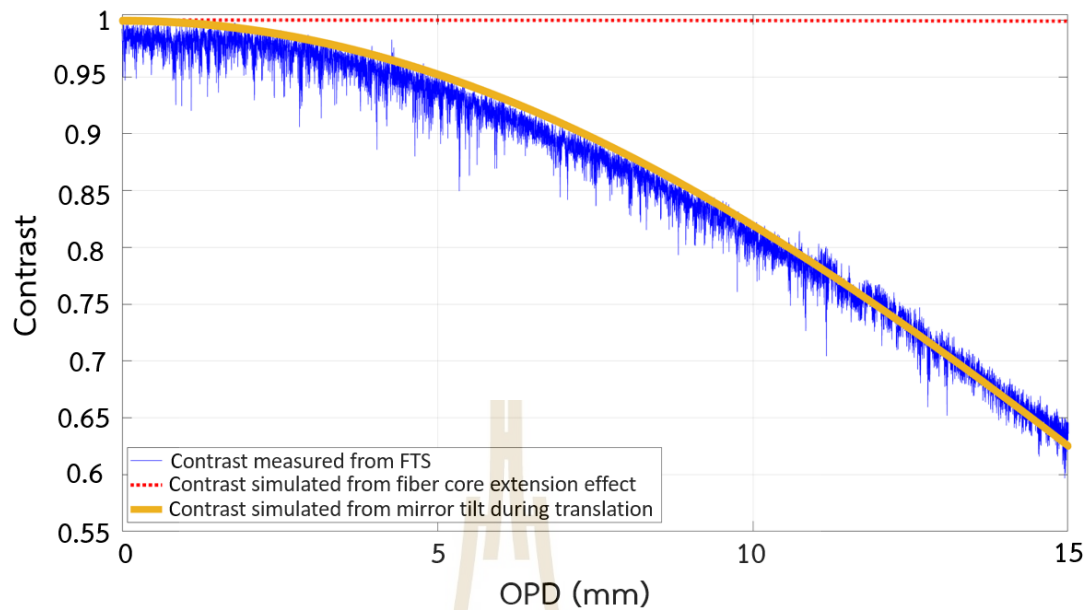
Figure 4.12 An illustration of between contrast and *OPD* variation. Blue solid: measured contrast from FTS experiment. Red dot: Theoretical contrast variation due to the spatial extension of the fiber core. Yellow solid: Theoretical contrast variation due to a tilt in mirror along the translation.

4.2.3 The instrument line shape

The Instrument Line Shape (ILS) defines the line shape in a measured spectrum that differs from the true spectrum of the source due to the physical instrument deviations (Libert, 2016). The measurement of ILS is consisted of measuring spectrum provided by the instrument of a monochromatic source. The monochromatic source used for this measurement was the metrology laser.

The ILS of FTS system was by turning "ON" the metrology source and removing the I-band filter in front of the detector. The observed fringes are induced by the leakage of the metrology signal on the detector. The acquired signals were based on the properties as shown in Table 3.2. The measured ILS from metrology leakage does not include the effect of the scientific fiber on the ILS.

However, as mentioned in the previous Section, the fiber core diameter has a negligible effect on the contrast loss. Notice that the metrology follows an optical path close to the scientific beam and therefore can be used to obtain the ILS of the prototype.

The results of three ILS that were obtained from the measurement using the parameter in the Table 3.2 are illustrated in Figure 4.13, including of

i)   The theoretical model of ILS (ILS$_{theo}$) is plotted in the blue dot line.

ii)   The measured ILS that was retrieved from metrology leakage in FTS system (ILS$_{meas}$) is plotted in the red solid line.

iii)   The theoretical model of ILS with an effect of dynamic mirror tilt (ILS$_{theo,tilt}$), as described in the Section 4.2.2, is plotted in the yellow dot-dash line.
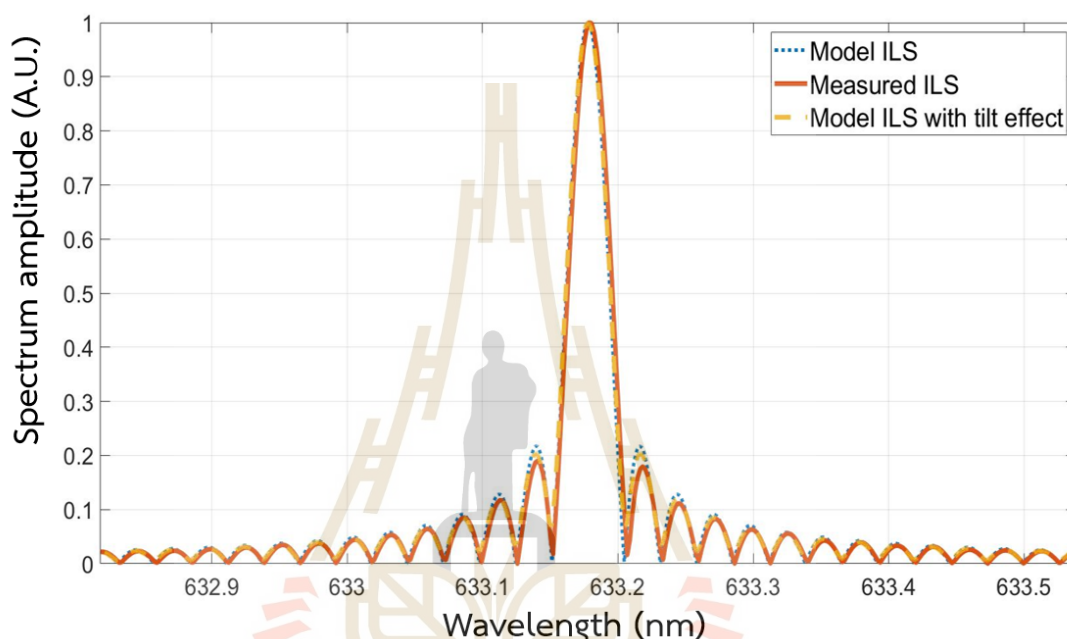
Figure 4.13   The comparison plots of ILS at central wavelength 633.178 nm. The blue dot line is the theotetical ILS (ILS$_{theo}$). The red solid line is the measured ILS (ILS$_{meas}$). The yellow dot-dash line is the theoretical ILS with the tilt effect (ILS$_{theo,tilt}$).

The characterization of the measured ILS was considered by using two critical points. First, the central wavelength (CWT) shifted and the second is the Full Width at Half maximum (FWHM) of the spectrum.

As described in Section 2.4, the ILS is related to the spectrum of finite path difference. The ILS$_{theo}$ of monochromatic source at frequency σ is observed in the sinc function and expressed in the Equation (2.34). In practice, the measure ILS that was obtained from the experiment can be expressed as (Lacan et al., 2010)

$$S_{ILS}(\sigma) = Asinc[OPD_{max}(\sigma' - \sigma - \epsilon(\sigma))] , \tag{4.8}$$

where A defines the amplitude coefficient of the spectrum. σ' is the measured frequency which is obtained from the ILS_{meas}. $\epsilon(\sigma)$ is the tuning error of the source.

Notice that the CTW of the metrology source is equal to 633.178 nm. Figure 4.14(a) presents the zoom in of the ILS in which a small shift in CTW in the ILS_{meas} has been observed. The CTW of ILS_{meas} is observed at 633.1795 nm, which provided a tuning error $\epsilon(\lambda)$ equal to 1.5 pm. The potential contributors to this difference are the laser stability, which is equal to 2 pm (from specifications: SLM_52371_2-258, Edmund Optics Inc., USA) and the tuning error of the laser (Lacan et al., 2010).
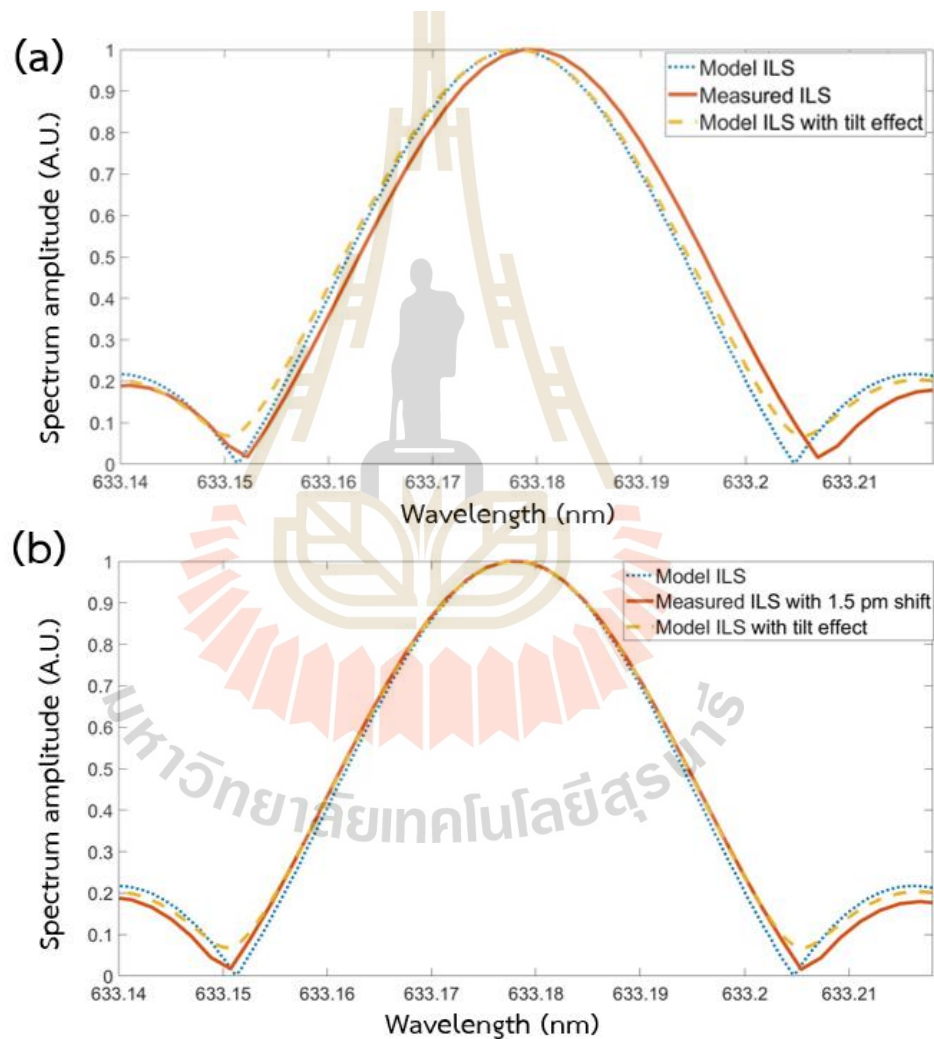
Figure 4.14   An illustration of the three ILS plots near CTW. (a) The zoom in of the ILS results in Figure 4.11. (b) The zoom in of ILS results in Figure 4.11 after applying the shift of 1.5 pm to ILS_{meas}.

As the second consideration, the FWHM was calculated in the optical frequency domain. The theoretical FWHM of ILS$_{theo}$ can be obtained as $\delta\sigma = 1.207/OPD_{max} \cong 0.80\,\text{cm}^{-1}$. In the wavelength domain, the FWHM was thus retrieved from the relation $\delta\lambda \cong \lambda^2\delta\sigma$.

Therefore, at the wavelength $\lambda = 633.178$ nm, the FWHM of ILS$_{theo}$ approximately was equal to 0.032 nm. When the CTW of ILS$_{meas}$ is shifted to the theoretical CTW at 633.178 nm, as illustrated in Figure 4.14(b), it is obviously seen that both ILS$_{meas}$ and ILS$_{theo,tilt}$ provided identical FWHM equal to 0.03229 nm, which are wider approximately 3% than the theoretical FWHM.

4.2.4 The spectral resolution of instrument line shape

This Section presents the calculation of spectral resolution by following the Equation (2.49) that was described in Section 2.7.1. The result of FWHM that were presented in the previous Section provides the theoretical spectral resolution that is retrieved from the ILS$_{theo}$ of equal to R$_{theo}$ = 19,787.

In the FTS measurement, the spectral resolution that is calculated from the FWHM of ILS$_{meas}$ is reduced to R$_{meas}$ =19,609. In parallel, the spectral ILS$_{theo,tilt}$ is obtained as R$_{theo,tilt}$ = R$_{meas}$. Therefore, the decrease in the spectral resolution of the system is related to by the effect of contrast loss. The result is summarized as presented in the table 4.1.

Table 4.1   The spectral qualities that obtained from ILS at OPD_{max} =15 mm.

ILS	CTW shift (pm)	FWHM (nm)	FWHM (cm^{-1})	Spectral resolution (R=$\lambda/\Delta\lambda$)
ILS$_{theo}$	0	0.03201	0.804	R$_{theo}$ = 19,781
ILS$_{meas}$	1.5	0.03229	0.805	R$_{meas}$ = 19,609
ILS$_{theo,tilt}$	0	0.03229	0.805	R$_{theo,tilt}$ = 19,609

4.3 Signal processing

4.3.1 The verification of processing code

In this part, to verify the processing code, a halogen-tungsten source (SLS201L/M Thorlabs Inc., USA) was coupled to an optical fiber with high OH absorption and then measured with the FTS system. The spectrum results were obtained from the developed resampling code method II and process in MATLAB 2020a.

The three spectra, as illustrated in Figure 4.15, were measured.

i) The spectrum of halogen-tungsten source excludes the bandpass filter, which is represented the fiber profile with high OH absorption at wavelength 940 nm as in the specification (OP0024[A], SHELYAK INSTRUMENTS, France), as plotted in the blue line.

ii) The spectrum of halogen-tungsten source with a bandpass filter at central wavelength 650 nm and bandwidth 40 nm (FBH650, Thorlabs Inc., USA), as plotted in the red line.

iii) The spectrum of halogen-tungsten source with a bandpass filter at central wavelength 800 nm and bandwidth 40 nm (FBH800, Thorlabs Inc., USA), as plotted in the black line.

As illustrated in Figure 4.15, the two spectral profiles of the halogen-tungsten source with two bandpass filters, can be matched with the obtained fiber spectral profile without bandpass filter and thus implied that our developed processing code worked properly.
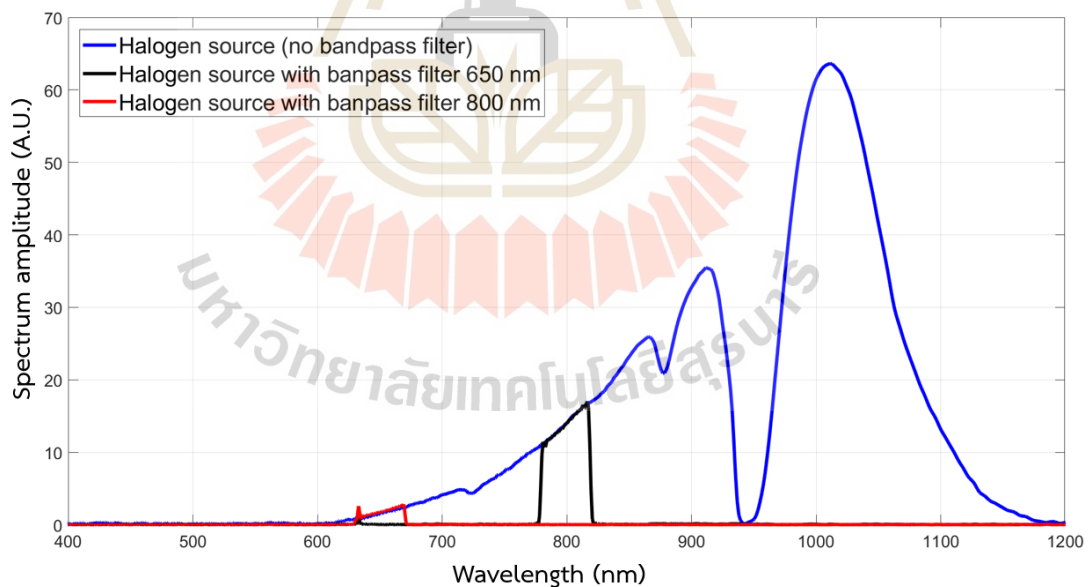
Figure 4.15   The plots of the three spectra that were measured from halogen-tungsten source. The blue line shows the spectrum of the source with no optical filter while the red and black lines present the spectra obtained with bandpass filters at central wavelength 650 nm and 800 nm, respectively.

4.3.2 The spectrum analysis in resampling methods

In this Section, the performance of two resampling methods will be discussed. The interferogram signals was obtained from the Halogen-Tungsten source with the bandpass filter 800 nm to avoid the metrology leakage. The performances will be represented by the SNR calculation of the spectrum results and the processing time in each method.

The resampling timegrid obtained from method I and method II are respectively plotted in the top-panel of Figure 4.16. The residual variances were created from the difference timestamps that retrieved from the two methods.
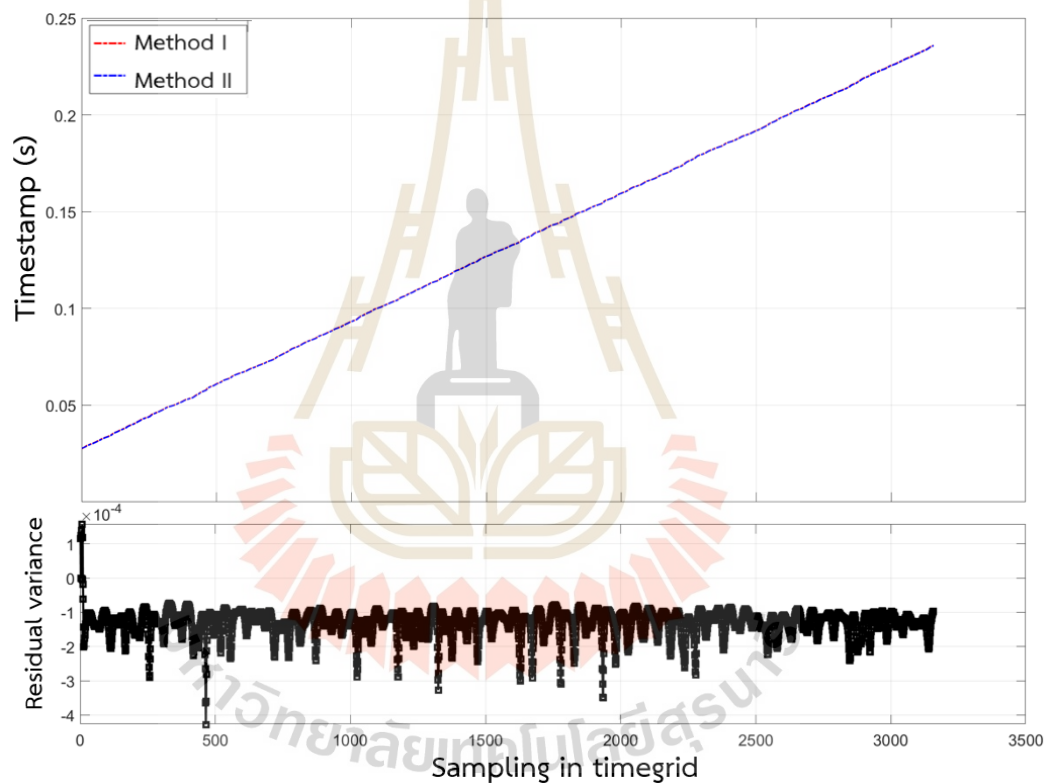
Figure 4.16   Top panel: The two timegrids obtained from method I (red) and from method II (blue). Bottom panel: The residual variances of timestamps between the two methods.

The spectrum results that were obtained from the two resampling methods are plotted in the top-panel of Figure 4.17, while the difference amplitude between two spectra are illustrated as the residual plotted in the bottom-panel.

The SNR is calculated by the ratio between the maximum of the spectrum intensity (S_{max}) and the standard deviation (STD) of the feet of the spectrum noise.

The spectrum result obtained from method II provides a slightly higher S_{max} but significantly lower STD than method I.
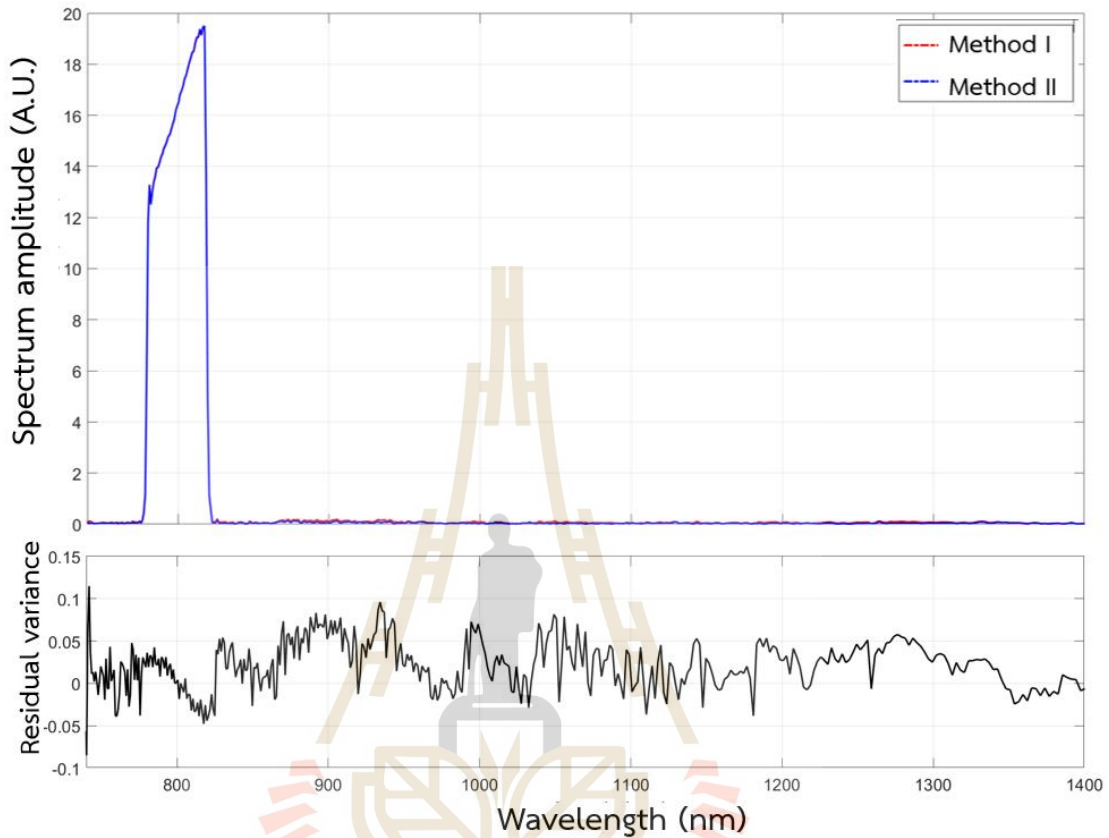
Figure 4.17 Top-panel: The spectrum results obtained from method I in the red plot and from method II in the blue plot. Bottom-panel: The residual of two spectra that retrieved from two methods.

Table 4.2 presents the result of the SNR calculations and the processing time, which represent the performance of the two resampling methods. The result shows that our developed resampling method II provides spectrum results of about twice as high SNR than a spectrum obtained from the resampling method I, but it took a longer processing time.

Table 4.2   The performances of the spectrum analysis obtained from two processing methods.

Qualities	Method I	Method II
S_{max}	19.45	19.50
STD	0.0408	0.0268
SNR	476.7	727.6
Time of processing	0.015 seconds	0.51 seconds

4.4 The Sun observation

The experimental setup was previously described in Section 3.6.1. The scientific fiber was then connected to the FTS system inside the controlled room. The flux of defocused Sun light at the output of the fiber equal to 1.27 μW, which is equivalent to a bright star at magnitude equal to -4. The observations were recorded in January 27, 2021 starting from 3.30 PM to 4.30 PM local time in Thailand (GMT+7). The tracking errors with in the field of view should not compromise the integrated solar disk light in 20 minutes with 30 times of measurement.

4.4.1 The interferogram result

The interferograms were recorded by following the parameters presented in the Table 3.2 with the observation steps described in the Section 3.6. Figure 4.18(a) illustrates the single measured interferogram, which was recorded along the time variations. Each single measurement was processed to obtain the uniform OPD interval.

The developed processing code of method II that was described in Section 3.5.3 was implemented for the correction. The result of the resampling interferogram in one measurement is illustrated in Figure 4.18(b).
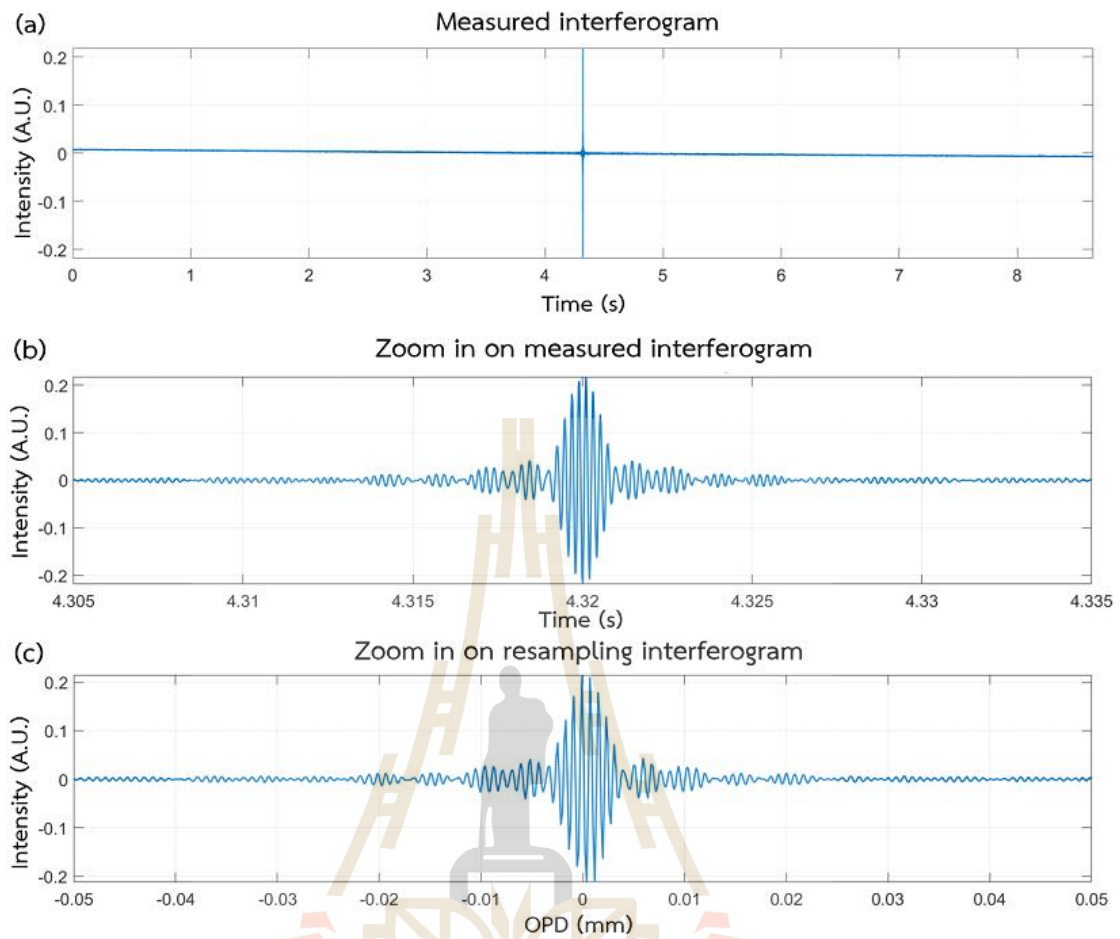
Figure 4.18 (a) The full scan range interferogram of the Sun observation from the FTS system. (b) The zoom in on central part of recorded interferogram. (c) The zoom in on central part of recorded interferogram in OPD range ±0.05 mm.

In order to increase the SNR, the measured interferograms were averaged. In this experiment, the 30 resampling interferograms were used to produce a symmetric interferogram. The final result was obtained as the symmetrical interferogram and illustrated with the zoom in Figure 4.19 within the OPD range ± 0.1 mm.
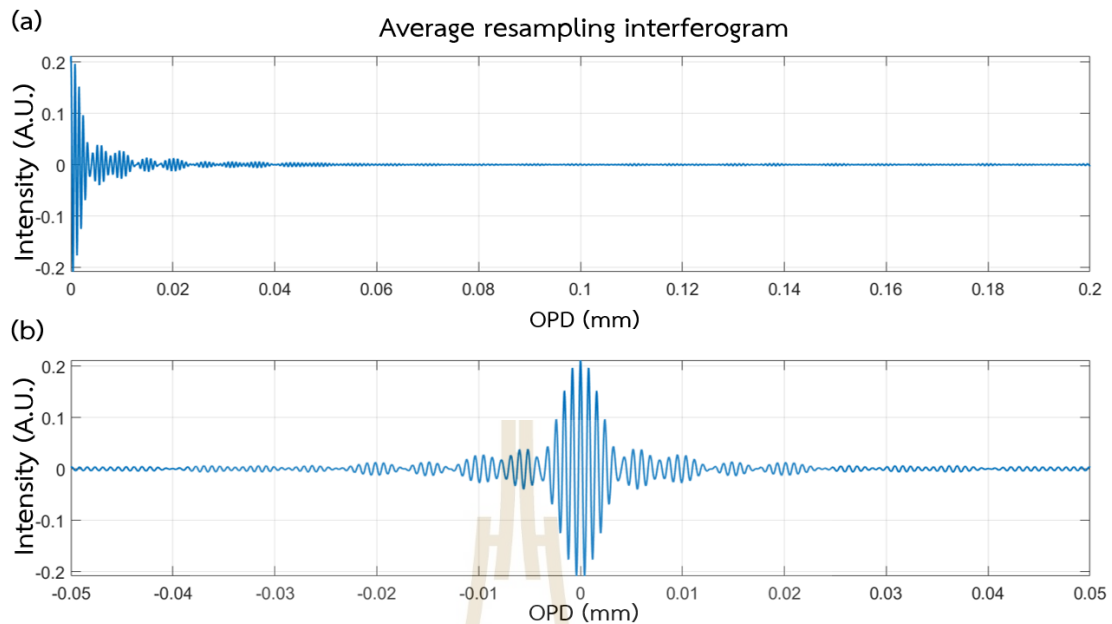
Figure 4.19   The interferogram result after taking an average on 30 resampling interferograms (a) the half interferogram between ZPD to OPD = 0.2 mm. (b) The symmetrical of average interferogram in OPD range ±0.05 mm.

4.4.2 The spectrum result

In ground-based observations, the effect of Earth's atmosphere to the spectrum result needs to be considered. This Section aims to present the spectrum result of the Sun from the observation compared to the spectrum model created from the Solar atmospheric model adopted parameters and abundance (Asplund et al., 2005).

Figure 4.20(a) presents the model of telluric lines that was generated from a web-based service named TAPAS (Transmissions of the AtmosPhere for AStronomical data) (Bertaux et al., 2014). TAPAS generates atmospheric lines using LBLRTM code (Clough and Iacono, 1995), HITRAN molecular lines (Rothman et al., 2013) and atmospheric profiles stored in the ETHER database, a French Atmospheric Chemistry Data Center ETHER (CNES and CNRS). The synthetic of Sun spectra were generated using SYNTHE code (Kurucz, 1993), as plotted in Figure 4.20(b).
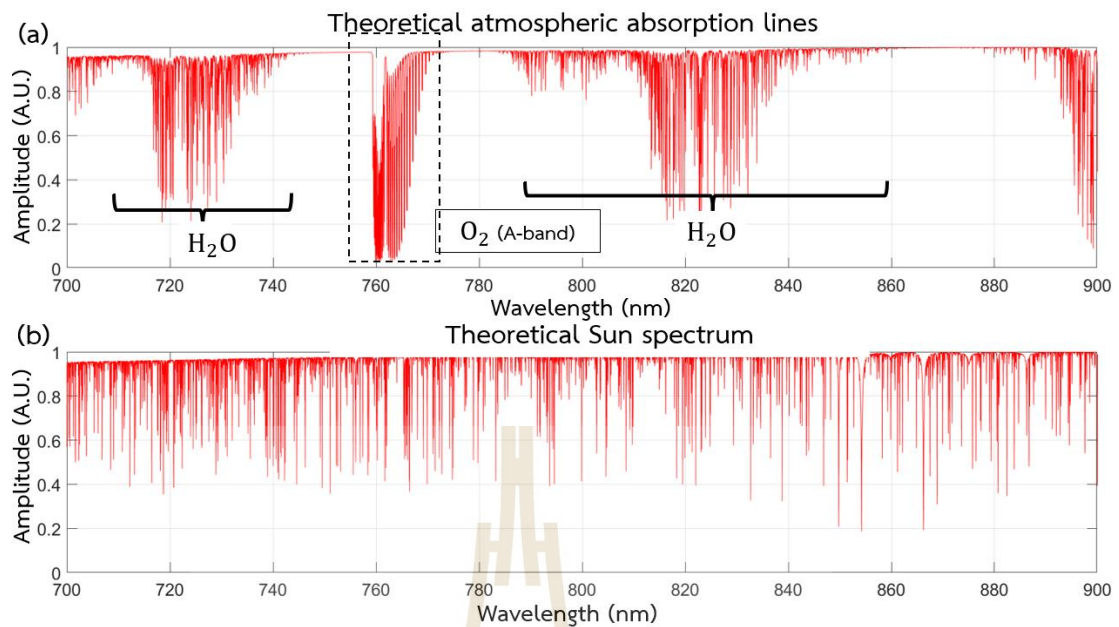
Figure 4.20 The synthetic model of (a) atmospheric absorption lines and (b) theoretical spectrum of the Sun between the range 700 nm and 900 nm.

The observation model spectrum was simulated in order to compare with the experimental result, as illustrated in Figure 4.21(a). The measured spectrum result that was obtained by taking the Fourier transform to an averaged symmetrical interferogram received from the previous Section is illustrated in Figure 4.21(b). The spectral range between 740 nm and 870 nm, which is related to the throughput response of the FTS system, is presented.
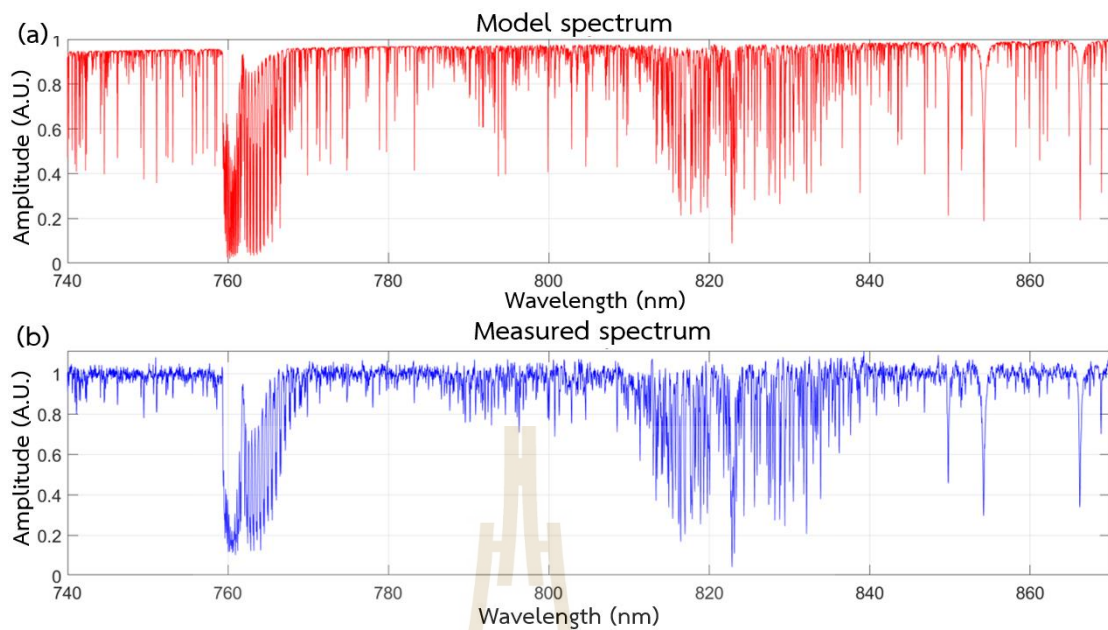
Figure 4.21   The measured spectrum of the Sun from the FTS measurement (a) in the blue line compared to the synthetic model spectrum (b) in red line.

4.4.3 The instrument calibration

The Sun light passed through the atmosphere that contains the natural gases, including of about 78% of N_2, 21% of O_2, and other gases (Smette et al., 2015), along the path. The atmospheric absorption lines as presented in Figure 4.22(a), also called "telluric absorption lines", are formed and then merged to the Sun spectral lines along the measurement. This effect induced the wavelength errors and line strengths in the measured spectrum as shown in the Sun spectrum in Figure 4.22(b). The telluric lines are registered in the same location along the measured spectrum. Therefore, in astronomical observations, the telluric lines are normally used for wavelength calibrations (Catanzaro and Doria, 1997) for the measurement.
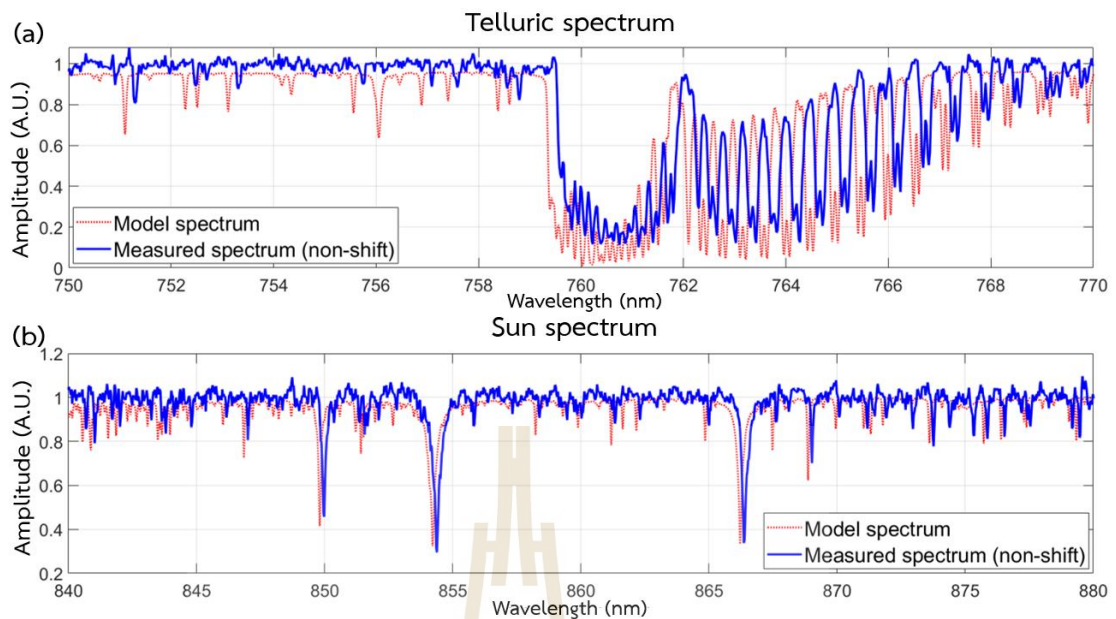
Figure 4.22   The zoom in of Sun spectrum for comparation between theoretical model in blue-solid line and the raw measured spectrum from the FTS measurement in red-dot line of the (a) telluric region and (b) the Sun absorption lines.

The instrumental corrections that were determined from the wavelength-shift of telluric lines between the measured spectrum and the model spectrum, is called "instrument shift". Our measurement has considered the telluric lines in the region of O_2 A-band between 759 nm and 772 nm as a reference.

The shift that applies to the spectrum was obtained from an average of instrument shifts. The instrument shift is related to the shift in the region of atmospheric or telluric lines. Multiple pairs of O_2 band in the theoretical telluric absorption lines, as illustrated in Figure 4.23(a) was selected and then the measured spectrum, which is corresponded to this pair were imported, as shown in the blue solid line of Figure 4.23(b). Figure 4.23(c) shows the overlapped plots between the model spectrum and the measured spectrum after correction of an instrument shift. Before applying the shift, the measured spectrum needs a gaussian fit, as plotted in the dot-dash purple line, in order to finely obtain the absorption peaks. The difference in location of the absorption peaks that were retrieved from the model spectrum and measured spectrum are considered for the instrument shift.
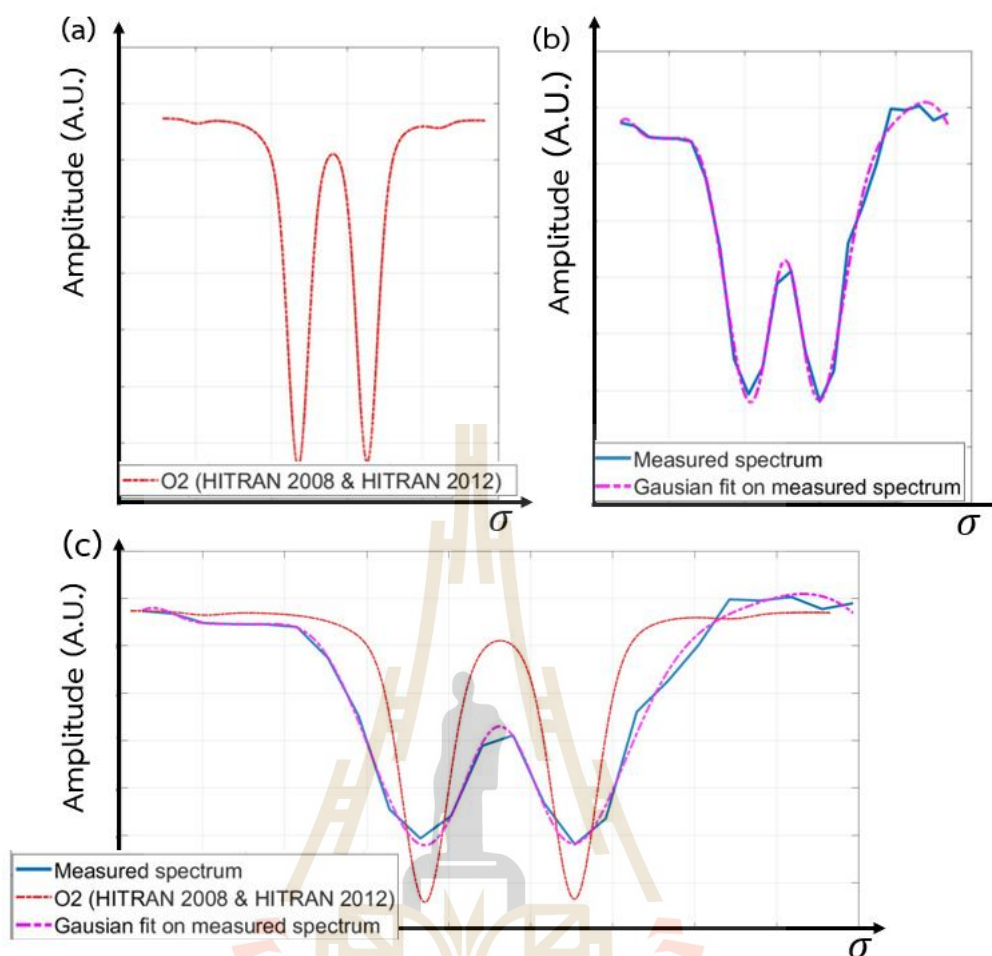
Figure 4.23 An illustration of instrument shift method.

Table 4.3 The determined instrumental shift in each pair of O_2 isotopes.

No	Spectral region		Reference peaks		Shift
	Isotopologue	Spatial frequency (cm^{-1})	(cm^{-1})		(cm^{-1})
1	$^{16}O_2$	13,158-13,165	12,992.30	12,994.34	3.33
2	$^{16}O_2$, $^{16}O^{17}O$	13,120-13,127	13,014.29	13,016.93	3.36
3	$^{16}O^{18}O$	13,060-13,067	13,062.61	13,064.95	3.29
4	$^{17}O^{18}O$	13,041-13,050	13,044.57	13,046.40	3.36
5	$^{16}O^{17}O$	13,029-13,041	13,035.13	13,036.97	3.29
6	$^{16}O^{17}O$	13,023-13,031	13,049.15	13,066.59	3.29
7	$^{16}O^{17}O$	13,007-13,019	13,015.15	13,016.93	3.32
8	$^{16}O_2$	12,990-12,999	12,992.30	12,994.34	3.29

Then, the method was repeated and applied into the 16 isotopes (8 pairs) of O_2 in A-band, providing the results presented in the Table 4.3. The average value of the instrument shift in this observation was determined as 3.32 cm^{-1}.
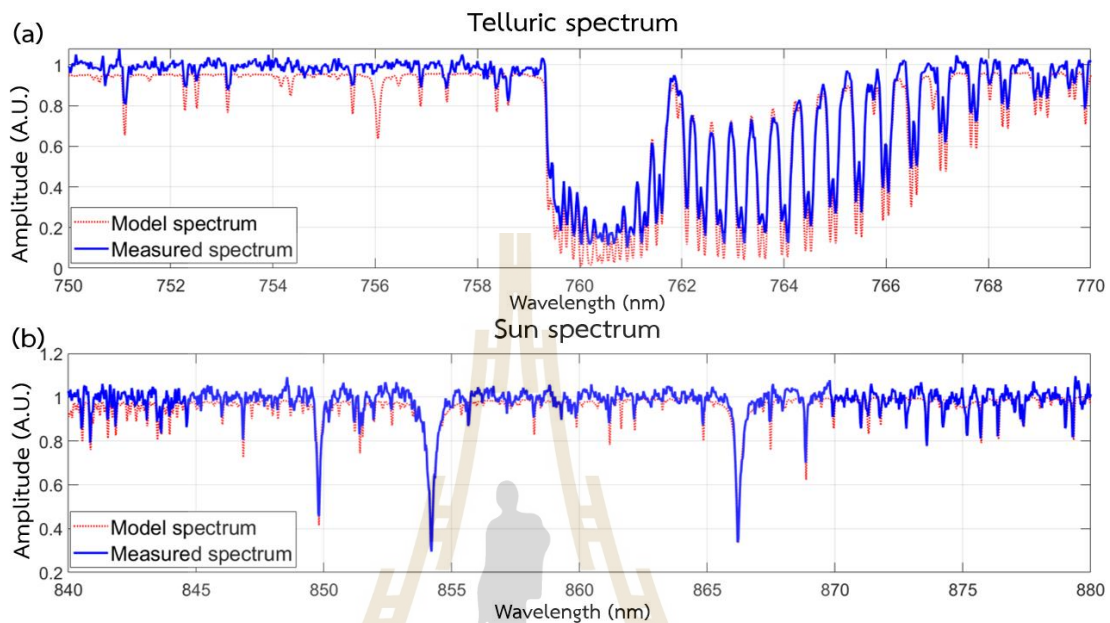
Figure 4.24　The zoom-in on for comparation between theoretical model in blue-solid line and the measured spectrum after applying an instrument shift in red-dot line of the (a) telluric region and (b) the Sun absorption lines.

In the final step, this average value was applied to the spectrum result for the instrument calibration. Figure 4.24 illustrates the shifted spectrum in the telluric region (a) and the Sun absorption (b).

4.4.4 The spectral qualities of the spectrum

The result of the four absorption lines of the Sun spectrum including their envelope regions for the spectral resolution and SNR determination is illustrated in Figure 4.25. First, the region of fine absorption of an iron (Fe I) at wavelength 846.8 nm was chosen, as illustrated in Figure 4.25(a). Second, the three distinctive Ca-II triplet absorption lines at wavelength 849.8 nm in Figure 4.25(b), 854.2 nm in Figure 4.25(c), and 866.2 nm in Figure 4.25(d) are presented.
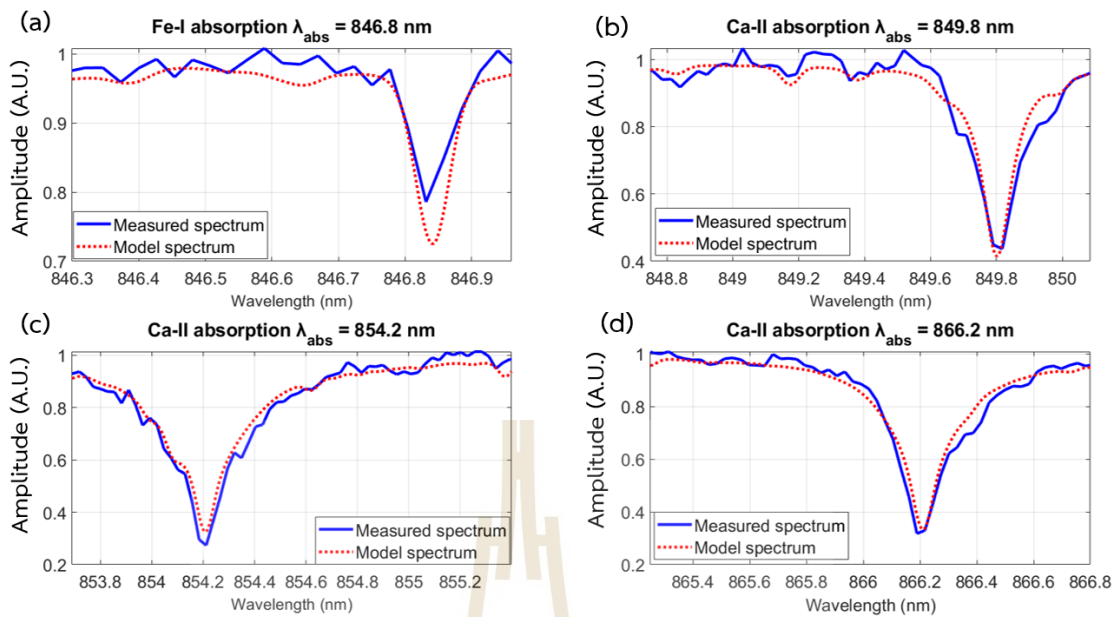
Figure 4.25   An illustration of (a) Fe-I absorption line at 846.8 nm. (b) 1st Ca-II absorption at central wavelength 849.8 nm. (c) 2nd Ca-II absorption at central wavelength 854.2 nm. (d) 3rd Ca-II absorption at central wavelength 866.2 nm.

The spectral resolution of each absorption line was calculated from the ratio between the FWHM of absorption line measured at the depth $\frac{S_{abs}}{2}$ and the standard deviation of its noise envelop that was described in the method II of Section 2.7.2. Table 4.4 summarizes the qualities of, FWHM and SNR at each the central wavelength measured on Fe-I and Ca-II triplet absorption lines.

Table 4.4   The spectral qualities of each absorption line in Figure 4.26.

	(a) Fe-I	(b) 1st Ca-II	(c) 2nd Ca-II	(d) 3rd Ca-II
Central wavelength	846.8 nm	849.8 nm	854.2 nm	866.2 nm
FWHM	0.0562 nm	0.125 nm	0.185 nm	0.181 nm
Spectral resolution	15,068	6,798.4	4,617.3	4,785.64
SNR	17.6	24.9	22.9	34.9

The results presented in Figure 4.25 and in Table 4.4 clearly show that the developed spectrograph is able to detect spectral lines of width varying between 0.0562 nm (Fe-I) and 0.185 nm (2nd Ca-II). The overall profile, depth, and FWHM of the

Ca-II absorption lines have been well measured. Ii can be deduced that the prototype is able to correctly measure some spectral lines with a width typically larger than 0.125 nm. The limit of detection of our instrument reached the Fe-I absorption line of FWHM equal to 0.056 nm, corresponding to the spectral resolution closed to 15,000. The instrument was able to detect the absorption line with an SNR close to 20.
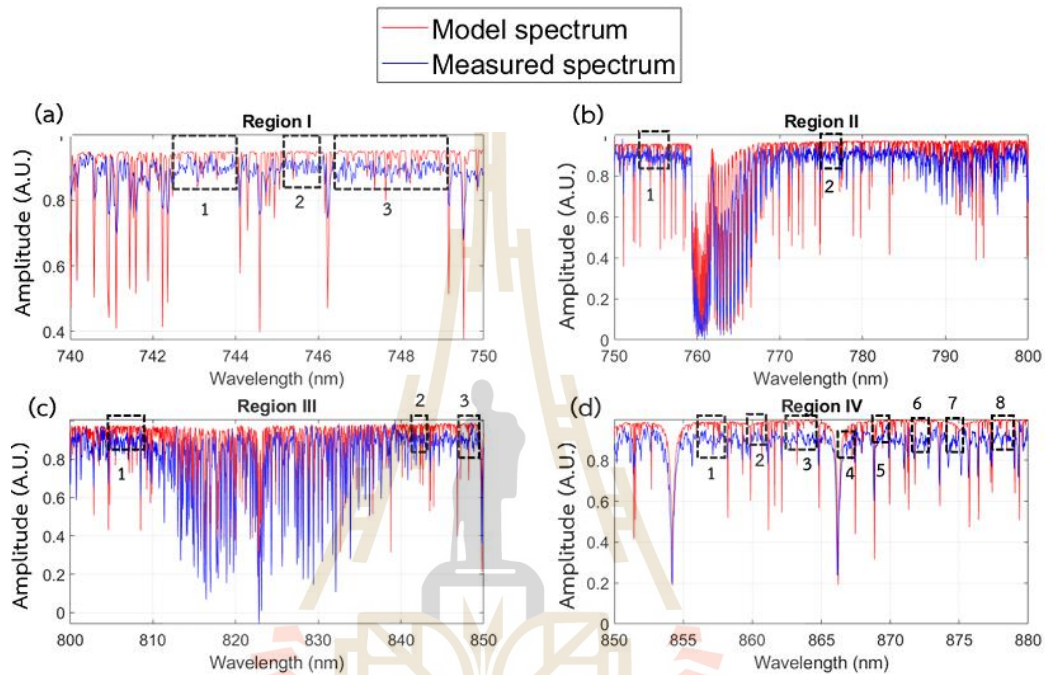
Figure 4.26　　An illustration the Sun spectrum after applying the instrumental shift correction.

The qualities of SNR from the whole measured spectrum were derived, as described in method III of Section 2.7.2. The zoom-in of four regions comparation between the theoretical model spectrum and the spectrum obtained from the observation are respectively presented in the red and blue lines, as illustrated in Figure 4.26.

The ranges of each selected sub-region that were inspected are bounded by the rectangular border in the black-dash line.

The signal variations in each sub-region provide the average $\bar{x}$ and the deviation STD, which are separately represented in each region in the Table 4.5. The SNR results obtained from this method are varied between the minimum value equal to 22.49 in and the maximum value equal to 49.53.

Table 4.5   The qualities for SNR characterization in each region of Figure 4.26.

No	$\bar{x}$	σ	SNR
Region I			
1	0.782907	0.019066	41.06378
2	0.794868	0.018193	43.69101
3	0.791278	0.035177	22.49439
Region II			
1	0.807764	0.017085	47.28009
2	0.855758	0.024107	35.49824
Region III			
1	0.843786	0.027204	31.01698
2	0.900330	0.019347	46.53532
3	0.906221	0.025522	35.50773
Region IV			
1	0.954317	0.029382	32.47942
2	0.985259	0.01989	49.53493
3	0.971976	0.025341	38.35616
4	0.923274	0.023388	39.47685
5	0.968018	0.025744	37.60233
6	0.944396	0.024739	38.17491
7	0.924928	0.028914	31.98848
8	0.850931	0.023931	35.55818

4.4.5 The instrument stability

The instrument stability is used to analyze the repeatability of single measurement of the system. In our measurement, as describe in the Section 4.4.3, the telluric absorption was used as the reference for the instrument calibration. To investigate the instrument stability along the observation, the instrument shift that was measured in each single scan of interferometer was considered.

In the result of Sun observation illustrated in Section 4.4.2, the spectrum was obtained from the low flux detection. The single measurement provides the low SNR spectrum, as illustrated in Figure 4.27(a). The correction of instrument calibration was implemented after taking an average to 30 resampling interferograms.

To determine the instrument calibration from the single measurement, the SNR in the spectrum result was improved by increasing the flux to the fiber. The absorption lines in telluric spectrum are thus clearly observed, as illustrated in Figure 4.27(b).
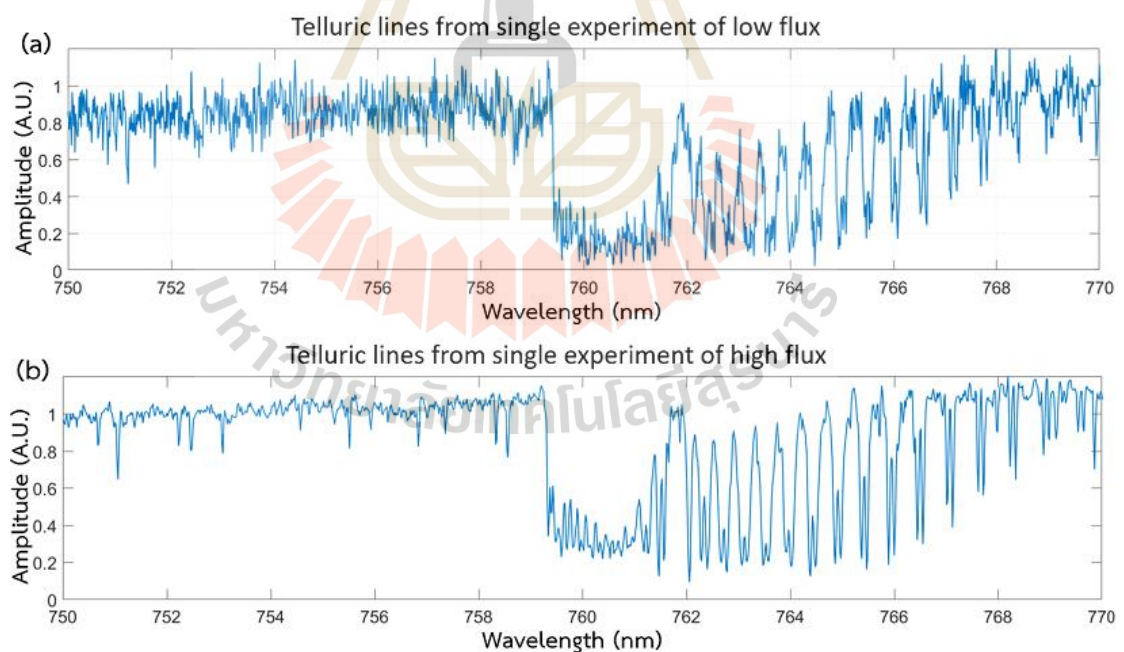
Figure 4.27 The telluric lines of (a) The low signal-to-noise-ratio that obtained from the single measurement of reduced flux Sun observation. (b) The higher SNR that retrieved from the increasing of Sun light flux in an observation.

As described in Section 4.4.3, the instrument calibration was calculated by comparing with telluric lines in the spatial frequency domain. Figure 4.28 illustrated the three spectral lines in the telluric region that were directly obtained from the measurements before applying the instrument calibration.
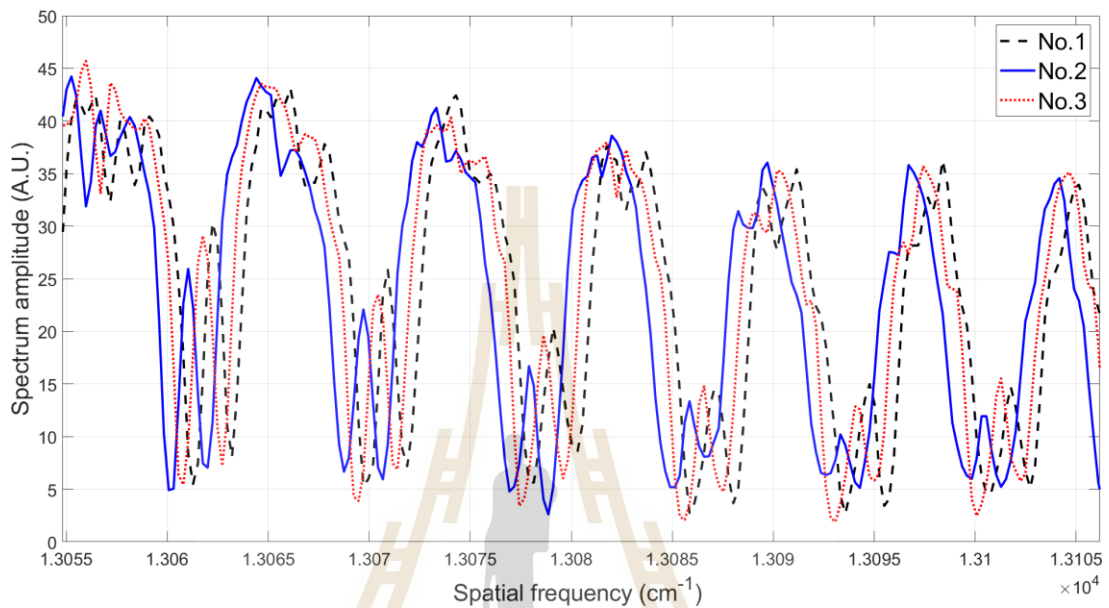
Figure 4.28   Illustrations of three telluric lines before applying instrument calibration.

The repeatability was measured along the 40 experiments. The shift in each single measurement was derived and plotted in the Figure 4.29 with an average shift equal to 3.30 cm^{-1}. The shift variance, as associated to the instrument stability along the measurements, was equal to 0.311 cm^{-1}. The instrument stability was verified by comparing to minimum resolvable of the instrument equal to 0.805 cm^{-1}, as derived in the Table 4.1. The smaller value derived in the shift variance indicates the success performance of our developed FTS system.
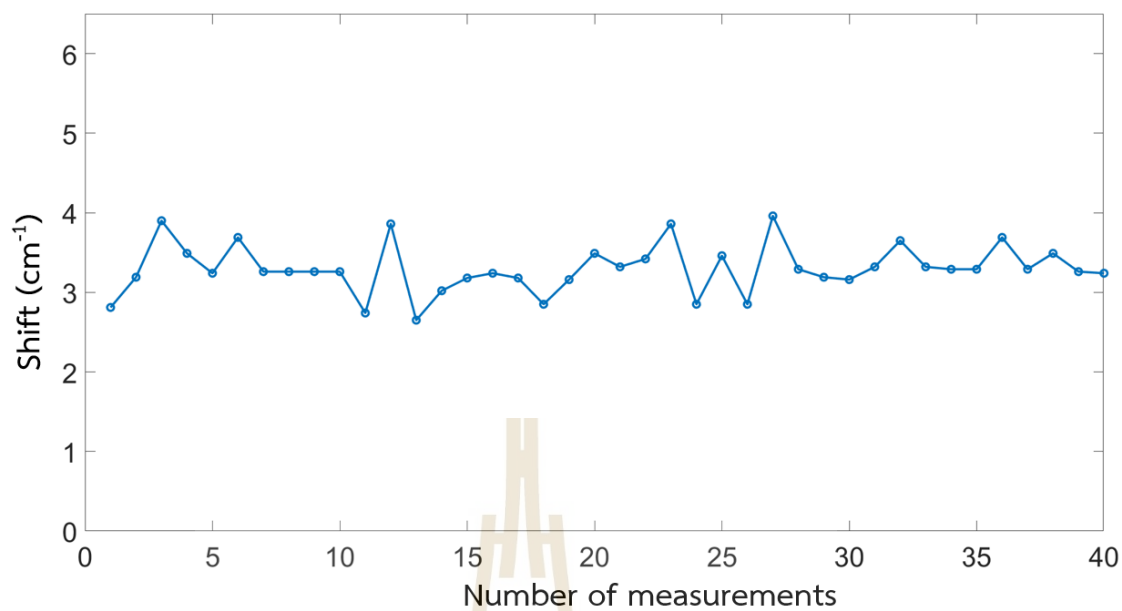
Figure 4.29   A plotted of instrument shift value that were determined from the single measurement of FTS system.

CHAPTER V

CONCLUSION

The prototype of fiber-fed Fourier Transform Spectrograph (FTS) built from off-the-shelf optical component have been successful developed. The instrument concept is based on a custom design to retrieve a compact system with balance detection. The achieved specification of this developed system is summarized in the table 5.1.

Table 5.1   The achieved performance of the current developed FTS.

Parameter	specification
Science spectral band	[700 nm, 900 nm]
Setup Architecture	one metrology channel and one scientific channel with balance detection
Input fiber	FC/PC connectors
	Core diameter 50 micron
	Numerical aperture 0.22
Metrology source	Stabilized laser wavelength 633.178 nm
Dynamic mirror Translating stage	High precision DC motor 200 mm range
Detector	Balanced Si photoreceiver Detectors

The developed FTS system provides a high throughput, insensitive to fiber modal noise and adjustable spectral resolution that was determined by the desired OPD. The maximum OPD is limited by the contrast loss in the system. The two effects

of contrast loss, including of the source's spatial extension and mirror tilt along the translation, have been investigated. The contrast variation in the developed FTS system is dominated by the tip-tilt performance of the mirror. The current maximum OPD of the developed FTS is equal to 1.5 cm.

The instrument line shape was measured by analyzing the metrology leakage. The FWHM of the line shape was measured as 0.03229 nm, which corresponds to the spectral resolution equal to 19,609 at the OPD of 1.5 cm. Notice that this spectral resolution can be adjustable depend upon the length of the scan. The common specifications of the developed FTS have summarized in the Table 5.2

Table 5.2   The common specifications of the developed FTS system

Specification	Value
Maximum optical path difference	1.5 cm
Spectral resolution	19,609
Spectral precision	0.31 cm^{-1}
Throughput	> 80% at $\lambda =$ 760-840 nm
Dimension	320 mm x 432 mm x 662 mm

The signal processing has been developed by using MATLAB R2021a. The scientific and metrology channels are simultaneously recorded. The peak and valley of metrology signal is used as the reference for the resampling method in order to correct of non-linear scan of dynamic mirror and recover the aliasing problem. The algorithm relies on the cubic spline interpolation and resampling of both the scientific and metrology interferograms to produce the spectrum from the raw measurements. The performance of the resampling method was verified.

The system was tested with the Sun observation. The result of measured spectrum was obtained by an average of 30 measurements. The measured spectrum was compared to a synthetic model and identified the observable telluric and solar absorption lines. The telluric lines model was generated from a web-based service

named TAPA, while the model spectrum of the Sun is obtained from the solar atmospheric model. The Ca-II absorption lines have been well detected. The limit of detection of the instrument can detect the Fe-I absorption line that was able to detect with a SNR close to 20.

The next development steps will aim at increasing the SNR to reach SNR ≈ 100 for an incident flux of a few nano-Watt and reach R ≈ 70,000 in the wavelength range between 400 nm and 1000 nm. The upgrades to reach these objectives will be the use of a phase-lock amplifier and a high-performance air-bearing translating stage.

REFERENCES

Aliaga, R. (2017). Real-time estimation of zero crossings of sampled signals for timing using cubic spline interpolation. *IEEE Trans. Nucl. Sci., 64*, 2414-2422. doi:10.1109/TNS.2017.2721103

Artsang, P., Buisset, C., Meemon, P., Rittipruk, P., Sithajan, S., Soonthornthum, B., and Poshyachinda, S. (2022). Design and laboratory performance of a fiber-fed Fourier transform spectrograph based on off-the-shelf components for astronomical medium and high-resolution spectroscopy. *Optical Engineering, 61*. doi:10.1117/1.OE.61.1.014104

Asplund, M., Grevesse, N., and Sauval, A. J. (2005, September 01, 2005). *The Solar Chemical Composition.* Paper presented at the ASPC.

Barducci, A., Guzzi, D., Lastri, C., Marcoionni, P., Nardino, V., and Pippi, I. (2010). Theoretical aspects of Fourier Transform Spectrometry and common path triangular interferometers. *Optics Express, 18*, 11622-11649. doi:10.1364/OE.18.011622

Beaudry, T. D. M. a. N. A. (2007). Coherence and Fringe Localization. Retrieved from https://www.tau.ac.il/~lab3/OPTICFIBERS/Coherence%20and%20Fringe.pdf

Bell, R. J. (1973). Introductory Fourier Transform Spectroscopy. *American Journal of Physics, 41*(1), 149-151. doi:10.1119/1.1987161

Bernier, A.-P., Grandmont, F., Rochon, J.-F., Charlebois, M., and Drissen, L. (2006, June 01, 2006). *First results and current development of SpIOMM: an imaging Fourier transform spectrometer for astronomy.* Paper presented at the Society of Photo-Optical Instrumentation Engineers (SPIE) Conference Series.

Bertaux, J. L., Lallement, R., Ferron, S., Boonne, C., and Bodichon, R. (2014). TAPAS, a web-based service of atmospheric transmission computation for astronomy. *A&A, 564*, A46. doi:10.1051/0004-6361/201322383

Born, M., and Wolf, E. (1999). *Principles of Optics: Electromagnetic Theory of Propagation, Interference and Diffraction of Light* (7 ed.). Cambridge: Cambridge University Press.

Bracewell, R. (2000). The Fourier Transform and Its Application. In (Vol. 34).

Brault, J. W. (1985, January 01, 1985). *Fourier Transform Spectroscopy.* Paper presented at the High Resolution in Astronomy.

Britannica, T. (2020). astronomical observatory. In *Encyclopedia Britannica*.

Buisset, C., Prasit, A., Leckngam, A., Lépine, T., Poshyajinda, S., Soonthornthum, B., Irawati, P., Richichi, A., Sawangwit, U., Dhillon, V., and Hardy, L. (2015). Progress on the prevention of stray light and diffraction effects on the Thai National Telescope. *SPIE Optical Systems Design, 9626*. Retrieved from https://doi.org/10.1117/12.2190411

Catanzaro, G., and Doria, V. (1997). High Resolution Spectral Atlas of Telluric Lines. *Astrophysics and Space Science - ASTROPHYS SPACE SCI, 257,* 161-170. doi:10.1023/A:1001197016750

Chakraborty, A., Mahadevan, S., Roy, A., Dixit, V., Harvey Richardson, E., Dongre, V., Pathan, F. M., Chaturvedi, P., Shah, V., Ubale, G. P., and Anandarao, B. G. (2014). The PRL Stabilized High-Resolution Echelle Fiber-fed Spectrograph: Instrument Description and First Radial Velocity Results. *PASP, 126*(936), 133-147. doi:10.1086/675352

Chalabaev, A. A., and Maillard, J. P. (1985). NEAR-INFRARED SPECTROSCOPY OF γ CASSIOPEIAE: CONSTRAINTS ON THE VELOCITY

FIELD IN THE ENVELOPE. *The Astrophysical Journal, 294*, 640-645.

Clough, S. A., and Iacono, M. J. (1995). Line-by-line calculation of atmospheric fluxes and cooling rates: 2. Application to carbon dioxide, ozone, methane, nitrous oxide and the halocarbons. *J. Geophys. Res, 100*(D8), 16519-16535. doi:10.1029/95JD01386

D., T. K. M., and Milster.(2021) *Coherence and Fringe Localization 41 5.2 Fringe Localization*.

Deng, Y., and Chu, D. (2017). Coherence properties of different light sources and their effect on the image sharpness and speckle of holographic displays. *Scientific Reports, 7*(1), 5893-5893. doi:10.1038/s41598-017-06215-x

Dhillon, V. S., Marsh, T. R., Atkinson, D. C., Bezawada, N., Bours, M. C. P., Copperwheat, C. M., Gamble, T., Hardy, L. K., Hickman, R. D. H., Irawati, P., Ives, D. J., Kerry, P., Leckngam, A., Littlefair, S. P., McLay, S. A., O'Brien, K., Peacocke, P. T., Poshyachinda, S., Richichi, A., Soonthornthum, B., and Vick, A. (2014). ULTRASPEC: a high-speed imaging photometer on the 2.4-m Thai National Telescope. *Monthly Notices of the Royal Astronomical Society, 444*, 4009. doi:10.1093/mnras/stu1660

Dondurur, D. (2018). Chapter 4 - Fundamentals of Data Processing. In D. Dondurur (Ed.), *Acquisition and Processing of Marine Seismic Data* (pp. 211-239): Elsevier.

Drissen, L., Alarie, A., Martin, T., Lagrois, D., Rousseau-Nepton, L., Bilodeau, A., Robert, C., Joncas, G., and Iglesias-Páramo, J. (2012). New scientific results with SpIOMM:

a testbed for CFHT's imaging Fourier transform spectrometer SITELLE. *Proc SPIE, 8446*. doi:10.1117/12.925202

Drissen, L., Bernier, A.-P., Charlebois, M., Alarie, A., Grandmont, F. d. r., and Mandar, J. (2011). Imaging Fourier Transform Spectroscopy for Astronomy, Fourier Transforms In G. Nikolic (Ed.), *Fourier Transforms - New Analytical Approaches and FTIR Strategies*

 Rijeka, Croatia: InTech.

Erickson, E. F., and Brown, R. M. (1967). Calculation of Fringe Visibility in a Laser-Illuminated Interferometer. *Journal of the Optical Society of America, 57*(3), 367-371. doi:10.1364/JOSA.57.000367

Fellgett, P. B. (1949). On the ultimate sensitivity and practical performance of radiation detectors. *J Opt Soc Am, 39*(11), 970-976. doi:10.1364/josa.39.000970

Grandmont, F., Drissen, L., and Baril, M. (2016, 2016/11/14). *The SITELLE Optical Imaging Fourier Transform Spectrometer at the Canada-France-Hawaii Telescope.* Paper presented at the Light, Energy and the Environment, Leipzig.

Griffiths, P. R., De Haseth, J. A., and Winefordner, J. D. (2007). *Fourier Transform Infrared Spectrometry* (2nd ed.). New Jersey: Wiley.

Hecht, E. (2002). *Optics 4th edition* (Vol. 4). adelphi university, New York: Addison Wesley.

Hecht, J. (2019). *Understanding Lasers: An Entry-Level Guide*: Wiley.

Heverly, M., Dougherty, S., Toon, G., Soto, A., and Blavier, J.-F. (2004). A Low Mass Translation Mechanism for Planetary FTIR Spectrometry using an Ultrasonic Piezo Linear Motor.

Hinse, T., Han, W., Yoon, J.-N., Lee, C.-U., Kim, Y.-G., and Kim, C.-H. (2015). Photometric Defocus Observations of Transiting Extrasolar Planets. *Journal of Astronomy and Space Sciences, 32*. doi:10.5140/JASS.2015.32.1.21

Hofmann, A. (2010). Spectroscopic Techniques: I Spectrophotometric Techniques. In K. Wilson and J. Walker (Eds.), *Principles and Techniques of Biochemistry and Molecular Biology*. United Kingdom: Cambridge University Press.

Holmes, D. S. (2007). *SIGNAL TO NOISE RATIO-WHAT IS THE RIGHT SIZE ?*

Hu, H., Yang, X., Zhai, F., Hu, D., Liu, R., Liu, K., Sun, Z., and Dai, Q. (2016). Far-field nanoscale infrared spectroscopy of vibrational fingerprints of molecules with graphene plasmons. *Nature Communications, 7*(1), 12334. doi:10.1038/ncomms12334

Hughes, C., Isaacson, J., Perry, A., Sun, R. F., and Turner, J. (2021). Creating Superposition: The Beam Splitter. In *Quantum Computing for the Quantum Curious* (pp. 17-28). Cham: Springer International Publishing.

Jacquinot, P. (1960). New developments in interference spectroscopy. *Reports on Progress in Physics, 23*, 267. doi:10.1088/0034-4885/23/1/305

Kirchner, J. (2005). Aliasing in 1/f(alpha) noise spectra: Origins, consequences, and remedies. *Physical Review E - PHYS REV E, 71*. doi:10.1103/PhysRevE.71.066110

Kurucz, R. (1993). SYNTHE Spectrum Synthesis Programs and Line Data Retrieved from https://ui.adsabs.harvard.edu/abs/1993KurCD13K.

L. Drissen, T. Martin, L. R. Nepton, A. Alarie, J. Mandar, A. Bilodeau, M. Baril, S. Lavoie, M. T. Duchesne, and Grandmont, F. (2016). SITELLE: A Primer. In (2nd ed.). CFHT.

Lacan, A., Bréon, F.-M., Rosak, A., Brachet, F., Roucayrol, L., Etcheto, P., Casteras, C., and Salaün, Y. (2010). A static Fourier transform spectrometer for atmospheric sounding: concept and experimental implementation. *Optics Express, 18*(8), 8311-8331. doi:10.1364/OE.18.008311

Laychak, M. B. (2020). Maunakea Spectroscopic Explorer and Astro2020.

Lhospice, E., Buisset, C., Jones, H. R., Martin, W., Errmann, R., Sithajan, S., Boonsri, C., Choochalerm, P., Anglada-Escudé, G., Campbell, D., Alagao, M. A., Paenoi, J., Prasit, A., Panyaphirawat, T., Rattanasoon, S., Leckngam, A., Mkrtichian, D., and Aukkaravittayapun, S. (2019). *EXOhSPEC folded design optimization and performance estimation* (Vol. 11117): SPIE.

Libert, A. (2016). *Design of a Fourier transform spectrometer for high resolution spectroscopy.* (master). Université catholique de Louvain,

Massey, P., and Hanson, M. M. (2013). Astronomical Spectroscopy. In (pp. 35).

McCurnin, T. W. (1981). CONTROL AND DATA ACQUISITION FOR A HIGH RESOLUTION DYNAMIC FOURIER TRANSFORM SPECTROMETER. In: The University of Arizona.

Migeotte, M. V. (1948). Spectroscopic Evidence of Methane in the Earth's Atmosphere. *Physical Review, 73*(5), 519-520. doi:10.1103/PhysRev.73.519.2

Migeotte, M. V. (1949). The Fundamental Band of Carbon Monoxide at $4.7\ensuremath{\mu}$ in the Solar Spectrum. *Physical Review, 75*(7), 1108-1109. doi:10.1103/PhysRev.75.1108

Naylor, D., Fulton, T., Davis, P., Chapman, I., Gom, B., Spencer, L., Lindner, J., Nelson-Fitzpatrick, N., Tahic, M., and Davis, G. (2004). Data processing pipeline for a time-sampled imaging Fourier transform spectrometer. *Proceedings of SPIE - The International Society for Optical Engineering, 5546*. doi:10.1117/12.560096

Newport. Large-Area BalancedPhotoreceiversModels 2307 & 2317. Retrieved from https://www.newport.com/medias/sys_master/images/images/h8d/h7d/87970 02727454/2307-2317-User-Manual-RevA.pdf

Paton-Walsh, C. (2011). Remote Sensing of Atmospheric Trace Gases by Ground-Based Solar Fourier Transform Infrared Spectroscopy

In G. Nikolic (Ed.), *Fourier Transforms - New Analytical Approaches and FTIR Strategies*. Rijeka, Croatia: Intech.

Pepe, F., Mayor, M., Delabre, B., Kohler, D., Lacroix, D., Queloz, D., Udry, S., Benz, W., Bertaux, J.-L., and Sivan, J.-P. (2000). *HARPS: a new high-resolution spectrograph for the search of extrasolar planets.* Paper presented at the Astron. Telesc. Instrum.

Pilachowski, C., Dekker, H., Hinkle, K., Tull, R., Vogt, S., Walker, D. D., Diego, F., and Angel, R. (1995). High-Resolution Spectrographs for Large Telescopes. *PASP, 107*(716), 983-989. Retrieved from http://www.jstor.org/stable/40680638

Queloz, D., Casse, M., and Mayor, M. (1999). The Fiber-Fed Spectrograph, a Tool to Detect Planets. *International Astronomical Union Colloquium, 185*, 13. doi:10.1017/S0252921100048284

Réhault, J., Borrego-Varillas, R., Oriana, A., Manzoni, C., Hauri, C. P., Helbing, J., and Cerullo, G. (2017). Fourier transform spectroscopy in the vibrational fingerprint region with a birefringent interferometer. *Optics Express, 25*(4), 4403-4413. doi:10.1364/OE.25.004403

Rinsland, C. P., Zander, R., Brown, L. R., Farmer, C. B., Park, J. H., Norton, R. H., Russell III, J. M., and Raper, O. F. (1986). Detection of carbonyl fluoride in the stratosphere. *Geophysical Research Letters, 13*(8), 769-772. doi:https://doi.org/10.1029/GL013i008p00769

Rodler, F., and Curto, G. L. (2019). HARPS User Manual. In (Vol. 2.4). Chile: European Southern Observatory.

Rothman, L. S., Gordon, I. E., Babikov, Y., Barbe, A., Chris Benner, D., Bernath, P. F., Birk, M., Bizzocchi, L., Boudon, V., Brown, L. R., Campargue, A., Chance, K., Cohen, E. A., Coudert, L. H., Devi, V. M., Drouin, B. J., Fayt, A., Flaud, J. M., Gamache, R. R., Harrison, J. J., Hartmann, J. M., Hill, C., Hodges, J. T., Jacquemart, D., Jolly, A., Lamouroux, J., Le Roy, R. J., Li, G., Long, D. A., Lyulin, O. M., Mackie, C. J., Massie, S. T., Mikhailenko, S., Müller, H. S. P., Naumenko, O. V., Nikitin, A. V., Orphal, J., Perevalov, V., Perrin, A., Polovtseva, E. R., Richard, C., Smith, M. A. H., Starikova, E., Sung, K., Tashkun, S., Tennyson, J., Toon, G. C., Tyuterev, V. G., and Wagner,

G. (2013). The HITRAN2012 molecular spectroscopic database. *J Quant Spectrosc Radiat Transf, 130*, 4-50. doi:10.1016/j.jqsrt.2013.07.002

Roy, S. A., Genest, J., and Giaccari, P. (2007). Hybrid sampling approach for imaging Fourier-transform spectrometry. *Applied Optics, 46*(35), 8482-8487. doi:10.1364/AO.46.008482

Simcoe, R. A., Burgasser, A. J., Schechter, P. L., Fishner, J., Bernstein, R. A., Bigelow, B. C., Pipher, J. L., Forrest, W., McMurtry, C., Smith, M. J., and Bochanski, J. J. (2013). FIRE: A Facility Class Near-Infrared Echelle Spectrometer for the Magellan Telescopes. *Publications of the Astronomical Society of the Pacific, 125*(925), 270-286. doi:10.1086/670241

Simon A. Roy, J. G., and Philippe Giaccari. (2007). Hybrid sampling approach for imaging Fourier-transform spectrometry. *Appl. Opt., 46*, 8482-8487.

Smette, A., Sana, H., Noll, S., Horst, H., Kausch, W., Kimeswenger, S., Barden, M., Szyszka, C., Jones, A., Gallenne, A., Vinther, J., Ballester, P., and Taylor, J. (2015). Molecfit: A general tool for telluric absorption correction. I. Method and application to ESO instruments. *Astronomy & Astrophysics, 576*. doi:10.1051/0004-6361/201423932

Soldevila, F., Clemente, P., Tajahuerce, E., Uribe-Patarroyo, N., Andrés, P., and Lancis, J. (2016). Computational imaging with a balanced detector. *Scientific Reports, 6*(1), 29181. doi:10.1038/srep29181

Thorne, A., Litzén, U., and Johansson, S. (1999). Spectrophysics: Principles and Applications. In. Berlin, Germany: Springer.

Toenger, S., Mäkitalo, R., Ahvenjärvi, J., Ryczkowski, P., Närhi, M., Dudley, J. M., and Genty, G. (2019). Interferometric autocorrelation measurements of supercontinuum based on two-photon absorption. *Journal of the Optical Society of America B, 36*(5), 1320-1326. doi:10.1364/JOSAB.36.001320

Undavalli, V. K., Ling, C., and Khandelwal, B. (2021). Chapter 6 - Impact of alternative fuels and properties on elastomer compatibility. In B. Khandelwal (Ed.), *Aviation Fuels* (pp. 113-132): Academic Press.

Zhang, P., Tan, Z., Ding, Z., and Guo, L. (2021). Simulation Analysis of Balance Detection Technique in Coherent Optical Receiver. *Optics and Photonics Journal, 11*, 301-313. doi:10.4236/opj.2021.118020

Zhang, Y., Li, Y., Wei, T., Lan, X., Huang, Y., Chen, G., and Xiao, H. (2010). Fringe Visibility Enhanced Extrinsic Fabry–Perot Interferometer Using a Graded Index Fiber Collimator. *IEEE Photonics Journal, 2*(3), 469-481. doi:10.1109/JPHOT.2010.2049833

APPENDIX A

RESAMPLING METHOD I

```matlab
%% Algorithm development for resampling and FFT implementation
%Method I: Cubic spline interpolation on the PV interval
%--------------------------------------------------------------
% create by Pornapa  Artsang
%--------------------------------------------------------------
clear all; close all; clc

%% call the file from data acquisition recorded
% drag excel file and put the name
name = ; %named of the dragged file
rm = 1; %remove the initial recorded error
[Ma,zp] = min(name(rm:end,2));
bg = zp-5e3+rm-1;
ed = zp+5e3+rm-1;

%call each column from the whole data
o_tstamp1 =  name(bg:ed,1); %time of data acquisition
o_Halogen =  name(bg:ed,2); %Halogen interference
o_sm_meth =  name(bg:ed,3); %Metrology interference

%% downsample (choice)
n =2; %defualt
sm_meth = downsample(o_sm_meth,n);
tstamp1= downsample(o_tstamp1,n);
Halogen = downsample(o_Halogen,n);
%see the range of signal
dx = [0:1:length(sm_meth )-1]; %length signal equals to length
time recording
dp = 0:0.01:length(sm_meth )-1;
tstamp = interp1(dx,tstamp1,dp,'spline');
sm_met = interp1(dx,sm_meth,dp,'spline');

% find peak and valley(-)
[~,PP] = findpeaks(sm_met); %find array of peaks in the
dataset
[~,VV] = findpeaks(-sm_met); %find array of valleys in the
dataset
pv = sort([PP,VV]); %line the position array
xTime = tstamp(pv);

%%
clear Time_d cm_time time_cell
N = 3;
for i = 1:length(pv)-1
    % implement cubic spline interpolation
```

```matlab
  Time_d{i} = linspace(pv(i),pv(i+1),N);
  cm_time(i,:) = cell2mat(Time_d(1,i));
  time_cell(i,:) = cm_time(i,1:end-1);
end
t_line = (cell2mat(Time_d));
last = t_line(end);
new_time = reshape(time_cell',1,[]); %arrange data in one row
timescale = [new_time last];
time_spline = csapi(pv,xTime,timescale); %find interval
time_spline = fnval(csape(pv,xTime),timescale);
%% timegrid varying for the resampling
figure(), plot(time_spline,'*-')
ax = gca; ax.FontSize = 15; %ax.FontWeight = 'bold';
xlabel('Sample','Fontsize',24);
ylabel('Time (s)','Fontsize',24);
title('Time grid for resampling','Fontsize',24);
%% Halogen and interpolation to the same interval as metrology
s2_H = Halogen-mean(Halogen); %remove DC
halogen = interp1(dx,s2_H,dp,'spline'); %interpolation

%% resampling implementation
resamp_cubic = interp1(tstamp,halogen,time_spline,'spline');

%% FFT implementation
m1 = length(resamp_cubic);
NFFT1 = pow2(nextpow2(m1)); %fft automatically pads the data
with zeros to increase the sample size.
inv_fft_resampTime=fftshift(ifft(ifftshift(resamp_cubic)));
delta_inv2 = inval/(wavelength*NFFT1); %m-1 unit, by 10
interval dividing in each half lambda %N=9delta is 16?
xScaled_inv2 = [-
(NFFT1*delta_inv2)/2:delta_inv2:(NFFT1*delta_inv2)/2-
delta_inv2];
xScale_nm_inv2=1./xScaled_inv2*1e9;
figure(),
plot(xScale_nm_inv2,abs(inv_fft_resampTime)./max(abs(inv_fft_r
esampTime)),'b', 'LineWidth', 1.5); xlim([400 1200]);%ylim([0
0.2])
title('Graph shows the FFT spectrum ');
xlabel('wavelength (nm)'); ylabel('Spectrum amplitude
(A.U.)');
ax = gca; ax.FontSize = 15;
```

APPENDIX B

RESAMPLING METHOD II

```matlab
%% Algorithm development for resampling and FFT implementation
%Method I: CSAPI interference line
%------------------------------------------------------------
% create by Pornapa  Artsang, Ph.D. student
%%%%%%%%%% November 2020 %%%%%%%%%%%%
%------------------------------------------------------------
clear all; close all; clc

%% call the file from data acquisition recorded
name = ; %named of the dragged file
rm = 1; %remove the initial recorded error
[Ma,zp] = min(name(rm:end,2));
bg = zp-5e3+rm-1;
ed = zp+5e3+rm-1;

%call each column from the whole data
o_tstamp1 =  name(bg:ed,1); %time of data acquisition
o_Halogen =  name(bg:ed,2); %Halogen interference
o_sm_meth =  name(bg:ed,3); %Metrology interference

%% downsample (choice)
n =2; %defualt
sm_meth = downsample(o_sm_meth,n);
tstamp1 = downsample(o_tstamp1,n);
Halogen = downsample(o_Halogen,n);

%% interpolation of metrology interference

dx = [0:1:length(sm_meth )-1]; %length signal equals to length
time recording
dp = 0:0.01:length(sm_meth )-1;
tstamp = interp1(dx,tstamp1,dp,'spline');
sm_met = interp1(dx,sm_meth,dp,'spline');

%% find peak and valley(-)
[~,PP] = findpeaks(sm_met); %find array of peaks in the
dataset
[~,VV] = findpeaks(-sm_met); %find array of valleys in the
dataset

%% find contrast of metrology(He-Ne) interference by using
each peak divides each valley
m = sm_met-min(sm_met); %remove DC
m =m'; %transpose from interpolation dimension
```

```matlab
Imax = mean(m(PP)); %average value of peak amplitude
Imin= mean(m(VV)); %average value of valley
contast = (Imax-Imin)/(Imax+Imin)
scan  = 2*(633.178e-9)*(PP);
tot_OPD = max(scan) %total OPD (roughtly)
l_opd = length(PP)+length(VV)-1;
d_opd = 2*tot_OPD/l_opd;

%% --------------------Defind range of Data -----------------
-----------------%%%
% create new signal (begin-finish WRT peak-vallay data)
% how to select the beginning of data--> start by peak-finish
by valley
% when do that phase inversion it will cause increasing

figure(), plot(sm_met(pv(1):pv(2))) %%%% important step

%% set the condition before starting

%if figure shows line with increasing slope:
L = pv(2):pv(end);
%if figure shows line with decreasing slope:
L = pv(1):pv(end);
L = pv(2):pv(end); %define range of processing

%% phase inversion implementation
ts = tstamp(L);
sm_met1 = sm_met(L);
%% Call the scientific signal
s2_H = Halogen-mean(Halogen); %remove DC
%interpolation to the same parameter as metrology
halogen = interp1(dx,s2_H,dp,'spline'); %interpolation
halo = halogen(L); %specify the range

%% Plot signal in the scale of OPD (optical path difference)
d_pv =(632.8/2)*1e-6;
tot_opd = length(pv)*d_pv; %mm unit = 7.6844 mm
d_opd = d_pv*length(pv)/length(ts);
opd_scale = 2.*[-tot_opd/2+d_opd/2:d_opd:tot_opd/2-d_opd/2];
figure(), plot(opd_scale,halo,'r','Linewidth',2)
hold on
plot(opd_scale,sm_met1,'b','Linewidth',2)
title('Graph shows two recorded signals in OPD variation:
scientific (red) and metrology (blue) ','Fontsize',22);
xlabel('OPD (mm)','Fontsize',22); ylabel('Amplitude
(A.U.)','Fontsize',22);
legend({'Scientific signal', 'Metrology
signal'},'FontSize',18)

% Interference line with CSAPI implementation
[~,P] = findpeaks(sm_met1); %find array of peaks in the
dataset
```

```matlab
[~,V] = findpeaks(-sm_met1); %find array of valleys in the
dataset
s_pv = sort([P,V]);
le_pv = length(s_pv);
y1 = ts; %time
x1 = sm_met1; %interference
lin2 = sort([1,P,V,le_pv]);

%% define interval -opposite condition with previous method
line = lin2(2:end);
%% interval point
N = 3; %default value N=3
%% Start processing
clear spi1 time_int1 cm_time1 time_cell1 new_time1 Alin1 Lin1
%if want to run with other intervals

for i = 1:length(line)-1
    % implement cubic spline interpolation

    spi1(i) = csapi(x1(line(i)+1:line(i+1)),
y1(line(i)+1:line(i+1)));

    if mod(i, 2) == 0

        Lin1 = linspace(spi1(i).breaks(1),
spi1(i).breaks(end), N);
        time_int1{i} = fnval(spi1(i), Lin1);%the time wrt to
N point (N-1 interval)

  % line the data
        cm_time1(i,:) = cell2mat(time_int1(1,i));
        time_cell1(i,:) = cm_time1(i,1:end-1);

    else

        ALin1 = linspace(spi1(i).breaks(end),
spi1(i).breaks(1), N);
        time_int1{i} = fnval(spi1(i), ALin1); %the time wrt
to N point (N-1 interval)

  % line the data
        cm_time1(i,:) = cell2mat(time_int1(1,i));
        time_cell1(i,:) = cm_time1(i,1:end-1);

    end %if
end

%% line the data of CSAPI
t_line1 = (cell2mat(time_int1));
last1 = t_line1(end);
%New x-axis scale
new_time1 = reshape(time_cell1',1,[]); %arrange the data in
one row
timescale1 = [new_time1 last1];
```

```matlab
%% resampling implementation
resamp_CSAPI = interp1(ts,halo,timescale1,'spline');

figure(), plot(timescale1,resamp_CSAPI,'-ro')

%% define the length of nuber of FFT
m1 = length(resamp_CSAPI);
NP1 = nextpow2(m1);
%specify range of data before FFT
ct1 = round(m1/2); %find the postion due to the center of data
x_resamp1 = (ct1-(2^(NP1-1)/2)):(ct1+(2^(NP1-1)/2))-1;
x_resamp_CSAPI = resamp_CSAPI(x_resamp1);
figure(), plot(x_resamp_CSAPI)

%% FFT implementation
% in the case using only fft implementation
NFFT2 = pow2(nextpow2(m1)); %fft automatically pads the data
with zeros to increase the sample size.
inv_fft_resampTime2=fftshift(ifft(ifftshift(x_resamp_CSAPI)));
% scale x-axis into wavelength unit
delta_inv2 = inval/(wavelength*NFFT2); %m-1 unit, by 10
interval deviding in each half lambda %N=9delta is 16?
xScaled_inv2 = [-
(NFFT2*delta_inv2)/2:delta_inv2:(NFFT2*delta_inv2)/2-
delta_inv2];
xScale_nm_inv2=1./xScaled_inv2*1e9;
figure(),
plot(xScale_nm_inv2,abs(inv_fft_resampTime2)./max(abs(inv_fft_
resampTime2)),'b', 'LineWidth', 1.5); xlim([400
1200]);%ylim([0 0.2])
title('Graph shows the FFT spectrum of Halogen in CSAPI
method');
xlabel('wavelength (nm)'); ylabel('intensity (A.U.)');
```

CURRICULUM VITAE

Name   Ms. Pornapa Artsang

Date of Birth   29 September 1994

Place of Birth   Surin, Thailand

Education

- (2009-2011) High school, Science Classrooms in University-Affiliated School Project (SCiUS) program from Ratchasima Witthayalai School, Nakhon Ratchasima, Thailand
- (2012-2015) Physics (Honors) B.Sc. with GPA 3.90 from Suranaree University of Technology, Nakhon Ratchasima, Thailand under Development and Promotion of Science and Technology Talents Project (Royal Government of Thailand scholarship) or DPST scholarship
- (2016-present) Ph.D. student in Applied Physics program at Suranaree University of Technology (DPST scholarship) GPA 4.00

Publications

- Artsang, P., Buisset, C., Meemon, P., Rittipruk, P., Sithajan, S., Soonthornthum, B., and Poshyachinda, S. (2022). Design and laboratory performance of a fiber-fed Fourier transform spectrograph based on off-the-shelf components for astronomical medium and high-resolution spectroscopy. Optical Engineering, 61(1), 014104. Retrieved from https://doi.org/10.1117/1.OE.61.1.014104
- Artsang, P., Pongchalee, P., Palawong, K., Buisset, C., and Meemon, P. (2018, March 01, 2018). A technique for phase correction in Fourier transform spectroscopy. Paper presented at the Society of Photo-Optical Instrumentation Engineers (SPIE) Conference Series.